UNIVERSIDAD DE CHILE
FACULTAD DE CIENCIAS FÍSICAS Y MATEMÁTICAS
DEPARTAMENTO DE ASTRONOMÍA

MOLECULAR CLOUDS IN EXTREME ENVIROMENTS OF THE LOW-METALLICITY MAGELLANIC SYSTEM

TESIS PARA OPTAR AL GRADO DE
MAGÍSTER EN CIENCIAS, MENCIÓN ASTRONOMÍA

MARÍA TERESA VALDIVIA MENA

PROFESOR GUÍA:
MÓNICA SOLANGE RUBIO LÓPEZ

MIEMBROS DE LA COMISIÓN:
ALBERTO BOLATTO
VIVIANA GUZMÁN VELOSO
LAURA PÉREZ MUÑOZ

Este trabajo ha sido parcialmente financiado por beca CONICYT-PFCHA/MagísterNacional/2018 - 22180279, proyecto FONDECYT no. 1190684, proyecto FONDECYT no. 1140839 y VID grant ENL22/18

SANTIAGO DE CHILE
2020

RESUMEN DE LA MEMORIA PARA OPTAR
AL GRADO DE MAGÍSTER EN CIENCIAS, MENCIÓN ASTRONOMÍA
POR: MARÍA TERESA VALDIVIA MENA
FECHA: 2020
PROF. GUÍA: MÓNICA SOLANGE RUBIO LÓPEZ

MOLECULAR CLOUDS IN EXTREME ENVIROMENTS OF THE LOW-METALLICITY MAGELLANIC SYSTEM

The goal of this thesis is to study the physical properties of the molecular clouds in Magellanic Bridge A, the source with the highest 870 μm excess of emission found in single dish surveys, and in the vicinity of the young massive cluster R136 in 30 Doradus (30Dor), using high-resolution ALMA and APEX (single dish) observations.

Magellanic Bridge A breaks up into two molecular clouds, North and South, in 870 μm continuum emission and in ^{12}CO(2-1) line emission. Dust in the North source, according to our best parameters from fitting the far-infrared fluxes, is ≈ 3 K colder than in the South source in correspondence to its less developed star formation. Both dust sources present large submillimeter excesses E, $E(870\mu m) \sim 7$ and $E(870\mu m) \sim 3$ for the North and South sources respectively, based on APEX single-dish LABOCA observations. Nonetheless, we do not detect the corresponding 1.3 mm continuum with ALMA. The ^{12}CO(2-1) emission is concentrated in two parsec-sized clouds with virial masses around 400 and 700 $M_\odot$ each. Their bulk volume densities are $n(H_2) \sim 0.7 - 2.6 \times 10^3$ cm^{-3}, larger than typical bulk densities of Galactic molecular clouds. The ^{12}CO luminosity to H_2 mass conversion factor α_{CO} is 6.5 and 15.3 $M_\odot\,(\mathrm{K\,km\,s^{-1}\,pc^2})^{-1}$ for the North and South clouds, calculated using their respective virial masses and ^{12}CO(2-1) luminosities. Gas mass estimates from our modified blackbody model fits to dust emission yields masses $M \sim 1.3 \times 10^3$ $M_\odot$ and 2.9×10^3 $M_\odot$ for North and South respectively, a factor of ~ 4 larger than the virial masses we infer from ^{12}CO.

In the vicinity of R136, we have resolved for the first time parsec-sized molecular clouds in ^{12}CO(3-2) and 880 μm continuum dust emission. We find that their virial masses are between $\sim 1000 - 2400$ $M_\odot$, and these masses are $2 - 3$ times larger than the gas masses obtained from dust emission in the same area. α_{CO} in this region is 4-6 times larger than the canonical galactic conversion factor (4.3 $M_\odot\,(\mathrm{K\,km\,s^{-1}\,pc^2})^{-1}$). The region was also mapped in ^{13}CO(3-2), CS(7-6), HCO$^+$(4-3) and HCN(4-3). Clouds which show emission in all these molecular species are the ones with the strongest ^{12}CO(3-2) emission. Kinetic temperatures derived from ^{12}CO emission range from 5.4 K to 33.4 K, and H_2 column densities derived from ^{13}CO emission range from $(4.2 - 23.7) \times 10^{21}$ cm^{-2}. Line ratios of the different molecular species show values similar to line ratios found in N11, N159 and N113 in the LMC. We find no dependence of the properties of the clouds with distance to R136.

The molecular clouds in these two extreme environments show some differences in their physical properties. 30Dor molecular clouds have larger velocity dispersions and Magellanic Bridge A clouds show lower CO luminosities, even though they have comparable radii. The lower CO luminosities could be explained due to the lower metallicity in the Magellanic Bridge. The larger velocity dispersions in 30Dor clouds could be a consequence of a higher energy input from R136 stars, in comparison to the more quiescent environment of Magellanic Bridge A.

NUBES MOLECULARES EN AMBIENTES EXTREMOS Y DE BAJA METALICIDAD DEL SISTEMA DE MAGALLANES

El objetivo de esta tesis es estudiar las propiedades físicas de las nubes moleculares en el Puente de Magallanes A (MagBridgeA), fuente que presenta el mayor exceso de emisión a 870 μm en estudios con telescopios single-dish, y en las cercanías del súper cúmulo estelar R136 en 30 Dorado (30Dor), usando observaciones a alta resolución angular de los telescopios ALMA y APEX (single-dish).

MagBridgeA se descompone en dos nubes moleculares en emisión de continuo en 870 μm y en la línea de emisión molecular ^{12}CO(2-1), las cuales llamamos Norte y Sur. El polvo de la fuente Norte es ≈ 3 K más frío que en la fuente Sur, de acuerdo a los parámetros del modelo de polvo que mejor ajustan los flujos en el infrarrojo lejano, lo cual coincide con su aparente menor formación estelar. Ambas fuentes tienen un alto exceso submilimétrico E en su emisión de polvo, $E(870\mu m) \sim 7$ y $E(870\mu m) \sim 3$ para las fuentes Norte y Sur respectivamente, en base a observaciones con el instrumento LABOCA en APEX. No obstante, no detectamos la emisión de continuo correspondiente a 1.3 mm con ALMA. La emisión de línea de ^{12}CO(2-1) está concentrada en dos nubes moleculares de ~ 1 pc de radio y masas viriales de ~ 400 y 700 $M_\odot$ cada una. Sus densidades son $n(H_2) \sim 0.7 - 2.6 \times 10^3$ cm^{-3}, mayores que las densidades típicas en nubes moleculares de la Vía Láctea. El factor de conversión de luminosidad de ^{12}CO a masa de H_2, α_{CO}, es 6.5 y 15.3 $M_\odot\,(\mathrm{K\,km\,s^{-1}\,pc^2})^{-1}$ para las fuentes Norte y Sur respectivamente, calculados a partir de sus masas viriales y luminosidades de ^{12}CO(2-1). Las masas de gas estimadas a partir del modelo de cuerpo negro modificado que mejor se ajusta a la emisión de polvo son $M \sim 1.3 \times 10^3$ $M_\odot$ y 2.9×10^3 $M_\odot$ para las fuentes Norte y Sur respectivamente, ~ 4 veces más grandes que las masas viriales obtenidas a partir del ^{12}CO.

Por primera vez resolvemos nubes moleculares en emisión de línea de ^{12}CO(3-2) y de continuo a 880 μm con una resolucion de 1 pc cerca de R136. Las masas viriales de las nubes resueltas varían entre $\sim 1000 - 2400$ $M_\odot$, las cuales son de 2 a 3 veces mayores que las masas de gas obtenidas a partir de su emisión de polvo en la misma área. α_{CO} en esta región es entre $4 - 6$ veces mayor que el factor de conversión en la Vía Láctea (4.3 $M_\odot\,(\mathrm{K\,km\,s^{-1}\,pc^2})^{-1}$). Esta región también fue observada en emisión de línea de ^{13}CO(3-2), CS(7-6), HCO$^+$(4-3) and HCN(4-3). Las nubes que muestran emisión de estas 4 transiciones moleculares son las que tienen la emisión más brillante en ^{12}CO(3-2). Las temperaturas cinéticas a partir de la emisión de ^{12}CO están entre 5.4 K y 33.4 K y las densidades de columna de H_2 a partir de la emisión de ^{13}CO están en el rango $(4.2 - 23.7) \times 10^{21}$ cm^{-2}. Las razones entre las diferentes emisiones moleculares muestran valores similares a razones de línea encontradas en N11, N159 y N113 en la Nube Grande de Magallanes. No encontramos una correlación entre las propiedades de las nubes moleculares y su distancia a R136.

Existen algunas diferencias entre las propiedades físicas de las nubes moleculares en ambos lugares. Aunque sean de tamaños similares, las nubes en 30Dor tienen dispersiones en velocidad más grandes que las nubes en MagBridgeA y estas últimas tienen menor luminosidad de CO. La diferencia en luminosidad puede deberse a la menor metalicidad en MagBridgeA. La mayor dispersión en velocidad de las nubes en 30Dor puede deberse a que reciben una mayor cantidad de radiación desde las estrellas de R136, en comparación al entorno menos activo de MagBridgeA.

Agradecimientos

Primero que todo, quiero agradecer a mi profesora guía, Mónica Rubio, por todo el apoyo, las enseñanzas y las oportunidades que me entregó durante la licenciatura y el magíster. Gracias de corazón por su paciencia y por nunca rendirse conmigo, en especial en los momentos más difíciles. También le agradezco al profesor Alberto Bolatto, quien me recibió en su oficina siendo una alumna recién licenciada, y me trató como una alumna suya desde entonces a la distancia, apoyándome en toda esta investigación.

Le doy mis más profundos agradecimientos a mi familia. A mis padres, quienes siempre privilegiaron mi educación por sobre todas las cosas. Le agradezco a mi mamá por enseñarme a ser una mujer fuerte y no rendirme por nada, y a mi papá, quien estando cerca o lejos siempre me ha apoyado en todas mis decisiones (no te preocupes seré doctora, solo que no en medicina). Quiero agradecer a mi esposo Jaime, quien me levantó en cada caída y me empuja siempre a hacer lo mejor. Sin su cariño este proceso habría sido mucho más difícil. Le agradezco a mis primos, quienes siempre han sido mis hermanos mayores, por cuidarme y acompañarme siempre, aunque estén lejos.

Quiero agradecer a todos mis amigos, a aquellos que han estado conmigo desde el colegio y a aquellos que llegaron después. Gracias a mis amigos del colegio por todas las risas y copuchas, a los "Feos", con los que nos conocimos en Plan Común y compartimos largas horas de estudio, al Club de Rol de InJeniería y la Sala 11, donde encontré mi lugar en la universidad y un nuevo hobby, a la Tere, el Jose y la Anto, quienes hicieron la licenciatura mucho más llevadera y entramos juntos al postgrado, a las Astroniñas, quienes me enseñaron el significado de la sororidad y me permitieron participar de un hermoso proyecto de difusión, y a los amigos que hice en las oficinas el Cerro Calán, tanto estudiantes como funcionarios, por todas las risas, llantos y asados que compartimos.

Le agradezco a todas las personas con las que trabajé en este magíster. A Hugo y Venu, gracias por todo el apoyo y lo que me han enseñado durante esta investigación. Gracias al equipo de APEX (Diah, Paulina, Panchito, Felipe, Claudio, Mauricio, Manuel, Karl y a muchos más) por las noches de observación donde aprendí muchísimo sobre la toma de datos.

Agradezco a ANID (ex-CONICYT) por el apoyo financiero otorgado a través de la Beca de Magíster Nacional folio no.2218279 y a traves de los FONDECYT no.1190684 y no.1140839. Agradezco al VID por el apoyo financiero a través del proyecto Enlace ENL22/18. Agradezco a SOCHIAS quienes financiaron viajes a congresos en los cuales pude presentar mi trabajo.

Contents

1 Introduction **1**
1.1 Molecular clouds . . . 1
1.2 Physical properties of CO molecular clouds . . . 2
1.2.1 Size . . . 2
1.2.2 CO intensity and luminosity . . . 3
1.2.3 Cloud mass . . . 3
1.2.4 Surface and volume density . . . 6
1.2.5 Correlations between physical properties . . . 7
1.3 Dust continuum emission . . . 7
1.3.1 Thermal dust emission . . . 7
1.3.2 Thermal free-free emission . . . 8
1.3.3 Synchrotron emission . . . 10
1.4 Molecular clouds in low-metallicity environments . . . 10
1.5 The Magellanic Bridge . . . 12
1.6 R136 in 30 Doradus . . . 13
1.7 Thesis goal and structure . . . 14

2 Observations and Data Processing **16**
2.1 Observations and data reduction for Magellanic Bridge A . . . 16
2.1.1 ALMA observations . . . 16
2.1.2 APEX observations . . . 19
2.1.3 Combined ALMA & APEX CO(2-1) observations . . . 22
2.1.4 Complementary data . . . 23
2.2 Observations and data reduction for 30 Doradus . . . 24
2.2.1 ALMA observarions . . . 24
2.2.2 Complementary Data . . . 26

3 Molecular clouds in Magellanic Bridge A **28**
3.1 Millimeter and submillimeter emission from Magellanic Bridge A . . . 28
3.1.1 Spectral energy distribution of Magellanic Bridge A . . . 29
3.1.2 SED modeling . . . 33
3.1.3 Submillimeter excess . . . 34
3.1.4 Gas masses obtained from dust emission . . . 36
3.2 Resolved CO(2-1) molecular clouds . . . 37
3.2.1 CO(2-1) molecular clouds spectra . . . 38
3.2.2 Physical properties . . . 39

3.3 Discussion . . . 40
3.3.1 CO(2-1) in comparison with previous studies . . . 41
3.3.2 Gas and dust comparison . . . 43
3.3.3 Gas and dust in the context of star formation . . . 44

4 Molecular clouds near R136 in 30 Doradus 45
4.1 Molecular Clouds near R136 . . . 45
4.1.1 Cloud identification . . . 45
4.1.2 Physical properties of molecular clouds near R136 . . . 50
4.2 Molecular Species in the Region . . . 53
4.2.1 Identification of molecular emission . . . 54
4.2.2 Integrated line intensities . . . 57
4.2.3 Molecular cloud luminosities in different molecular species . . . 58
4.2.4 Physical properties derived from ^{13}CO(3-2) molecular emission . . . 60
4.3 Submillimeter Emission towards R136 . . . 61
4.3.1 Cloud identification . . . 62
4.3.2 Flux measurements . . . 64
4.3.3 Free-Free Emission near R136 . . . 64
4.3.4 Gas mass from dust emission . . . 66
4.4 Comparison between molecular and continuum emission near R136 . . . 68
4.4.1 Extensions of CO and continuum emission . . . 68
4.4.2 Gas masses obtained through CO and dust emission . . . 70
4.5 Discussion . . . 71
4.5.1 Spatial variation in properties of CO clouds . . . 71
4.5.2 Comparison with CO emission in previous works . . . 73
4.5.3 Comparison between molecular line emission in R136 and the LMC . . . 75
4.5.4 Comparison between gas and dust emission . . . 79
4.5.5 Gas and dust in the context of star formation . . . 80

5 Conclusion 83

Bibliography 88

A CPROPS detections in ^{13}CO(3-2), CS(7-6), HCO$^+$(4-3) and HCN(4-3) 94

B Molecular line spectra for each CO cloud 97

List of Tables

2.1 Properties of the resulting continuum at 1.3 mm (230 GHz). UVT: uv-tapered images, using the tapering size in parenthesis. *Convolved to reach a beam size of 22". 19

2.2 Characteristics of the resulting line emission cubes. PA is the angle between the x axis and the major axis of the beam, counterclockwise. Δv_{chan} is the change in velocity from one spectral channel to another. ν_{rf} is the rest frequency of the line cube. 24

3.1 Dust emission flux densities in Magellanic Bridge A, North and South. We express the errors on our measurements with the flux calibration error first (Herschel errors obtained from Meixner et al. 2013) and the photometric error last.†Flux density at 870 μm has the free-free emission and CO(3−2) line contributions subtracted. ‡Flux density at 1.3 mm has the free-free emission contribution subtracted. *In Magellanic Bridge A, all images are convolved to a common resolution of 43". **In sources North and South, all images are convolved to a common resolution of 22". 32

3.2 Free-free emission for each source at 870 μm and 1.3 mm, obtained through aperture photometry. *Aperture photometry done in a circle with a radius of 50". **Aperture photometry done in a circle with a radius of 11". 32

3.3 Gas masses and best fit MBB parameters to the cloud SEDs. *Flux densities measured using aperture photometry radius of 50". **Flux densities measured using aperture photometry radius of 11". † β values obtained for Magellanic Bridge A MBB fit. ‡Gas masses derived from the MBB models that best fit the FIR SEDs of each source. 35

3.4 Submillimeter and millimeter excesses for Magellanic Bridge A and sources North and South. Excess is defined as the ratio between the observed flux density and the flux density predicted by the best fit MBB model to the FIR dust flux densities in the SED. 35

3.5 Characteristics of the clouds identified in the CO(2−1) line cube. [a]Peak values obtained from the CO(2−1) integrated line image between 172 and 176 km s^{-1}. [b]Values obtained from the Gaussian fit to the integrated spectra over the cloud area. 38

3.6 Physical properties of the emission found in the $^{12}CO(2-1)$ line cube. *Corrected for spatial broadening. **Assumes a CO(2−1) to CO(1−0) ratio $r_{21} \sim 1$. . . 40

4.1 30Dor detections in the ^{12}CO(3-2) line cube obtained using CPROPS. The CO(3-2) luminosity is calculated by CPROPS according to Equation 4.1. *The velocity FWHM is corrected for sensibility and resolution bias. †Characterized using a manual method, described in section 4.1.1.[c] Clouds with low luminosity ($L_{^{12}CO(3-2)} < 2$ K km s^{-1} pc^{-2}) will not be used to calculate physical properties. 47

4.2 Physical properties of the 30Dor clouds. The table does not include cloud no. 24, because it includes emission from sidelobes of other stronger clouds. These values are corrected for sensitivity and resolution bias. M_{CO}^{LMC} is calculated using $\alpha_{CO} = 8.4 \pm 3.0$ M$_\odot$ pc^{-2} (K km s^{-1})$^{-1}$ (Indebetouw et al. 2013), assuming $R_{\frac{3-2}{1-0}} \sim 2$ Johansson et al. (1998). M_{CO}^{Gal} is calculated using the canonical conversion factor for ^{12}CO(2-1) $X_{CO} = 2 \times 10^{20}$ cm^{-2} (K km s^{-1})$^{-1}$. $\Sigma_{\rm H_2}$ is calculated using M_{CO}^{LMC} and R values in this table. In the cases where clouds are not spatially resolved (both axes unresolved), virial masses are calculated as upper limits. *Minor axis is unresolved. **Both axes are unresolved. 51

4.3 Summary of the ^{12}CO(3-2) molecular clouds detected in the ^{13}CO(3-2), CS(7-6), HCO$^+$(4-3) and HCN(4-3) line emission cubes. Clouds which are not listed here are only detected in ^{12}CO(3-2) emission. 54

4.4 Integrated line intensities $I = \int T_v {\rm d}v$ for each of the molecular species found in the molecular clouds at the T_{peak} position for each molecule, after fitting a Gaussian profile to each respective spectra. 57

4.5 Intensity line ratios calculated from the intensity at the peak temperature position of each cloud in 30Dor, using the results shown in Table 4.4. 58

4.6 Luminosities of the ^{12}CO(3-2), ^{13}CO(3-2), CS(7-6), HCO$^+$(4-3) and HCN(4-3) molecular emission in each molecular cloud. The $L_{^{12}CO(3-2)}$ luminosities are the same as the ones presented in Table 4.1. 59

4.7 Molecular line ratios obtained from the luminosities in ^{13}CO(3-2), ^{12}CO(3-2), CS(7-6), HCO$^+$(4-3) and HCN(4-3) of each cloud in Table 4.6 for each ^{12}CO(3-2) molecular cloud. 60

4.8 Excitation temperatures, ^{13}CO(3-2) optical depths, ^{13}CO column densities and H_2 column densities for the peak temperature position of each molecular cloud from Section 4.1 which has a ^{13}CO(3-2) detection. We assume the excitation temperature for the ^{12}CO(3-2) and ^{13}CO(3-2) lines are the same so as to calculate the optical depth. We assume an abundance ratio $[H_2/^{13}CO] = 1.8 \times 10^6$ to go from $N(^{13}CO)$ to $N(H_2)$. 62

4.9 Areas and equivalent radii of the clouds found in the ALMA 880 μm image. 64

4.10 Results of the aperture photometry in the ALMA 880 μm continuum image, the free-free images obtained in Section 4.3.3 and in the dust images generated by subtracting the free-free images. RA and DEC are the right ascension and declination of the aperture center, and r_{ap} is the aperture radii. S_{880} is the flux obtained from the ALMA continuum image. $S_{ff,Br\gamma}$ and $S_{ff,{\rm radio}}$ are the fluxes obtained from the free-free images done with Brγ emission and radio continuum emission, respectively. $S_{{\rm d}ust}$ dust fluxes obtained by subtracting $S_{880} - S_{ff,Br\gamma}$. 67

4.11 Gas masses obtained from dust emission using Equation 1.16. M_{gas} and correspond to the gas masses obtained from dust fluxes $S_{{\rm d}ust}$ from Table 4.10. . 67

4.12 Velocity ranges used to integrate the CO line cube to find the areas and radii of the CO clouds, together with the corresponding ALMA 880 μm dust source for each cloud, the rms noise of each velocity integrated image and the areas found for each cloud. 70

4.13 Luminosities and gas masses traced by ^{12}CO(3-2) emission, obtained within the areas covered by the 880 μm continuum sources, together with the gas mass traced by dust emission in the same areas (from Table 4.11) and the ratios $M_{CO}^{A_{880\mu m}}/M_{gas}$ and $M_{vir}^{A_{880\mu m}}/M_{gas}$. †We use $R_{\rm eq,dc} = 1.26 \pm 0.22$ pc to calculate M_{vir} for clouds no. 16, 17 and 18 together, and we use the FWHM of cloud no. 17 as the FWHM because it is the largest FWHM of the three clumps. *Mass of B and D clouds together, obtained from the dust flux in the region shared by both clouds in 880 μm continuum emission. **Cloud not resolved, so the values are not considered for analysis. 71

A.1 Molecular clouds detected in the ^{13}CO(3-2) line cube. α and δ are the right ascension and declination, respectively. T_{peak} is the peak temperature detected in the ^{13}CO(3-2) line cube in K. v and Δv are the central velocity and FWHM of the clouds, respectively, in km s^{-1}. $R_{\rm dc}$ and R are the deconvolved and not deconvolved radii of the ^{13}CO(3-2) cloud, as characterized in CPROPS. For those clouds which are not resolved, we use the equations shown in Section 4.1.2 and take the deconvolved radii as an upper limit. $L_{^{13}CO(3-2)}$ is the ^{13}CO(3-2) luminosity in K km s^{-1} pc^{-2}. *Manually added detection, as CPROPS does not detect a cloud in ^{13}CO(3-2) in that location but a visual inspection reveals it. 95

A.2 Molecular clouds detected in the CS(7-6) line cube. α and δ are the right ascension and declination, respectively. T_{peak} is the peak temperature detected in the CS(7-6) line cube in K. v and Δv are the central velocity and FWHM of the clouds, respectively, in km s^{-1}. $R_{\rm dc}$ and R are the deconvolved and not deconvolved radii of the CS(7-6) cloud, as characterized in CPROPS. For those clouds which are not resolved, we use the equations shown in Section 4.1.2 and take the deconvolved radii as an upper limit. $L_{CS(7-6)}$ is the CS(7-6) luminosity in K km s^{-1} pc^{-2}. 95

A.3 Molecular clouds detected in the HCO^{+}(4-3) line cube. α and δ are the right ascension and declination, respectively. T_{peak} is the peak temperature detected in the HCO^{+}(4-3) line cube in K. v and Δv are the central velocity and FWHM of the clouds, respectively, in km s^{-1}. $R_{\rm dc}$ and R are the deconvolved and not deconvolved radii of the HCO^{+}(4-3) cloud, as characterized in CPROPS. For those clouds which are not resolved, we use the equations shown in Section 4.1.2 and take the deconvolved radii as an upper limit. $L_{HCO^{+}(4-3)}$ is the HCO^{+} luminosity in K km s^{-1} pc^{-2}. 96

A.4 Molecular clouds detected in the HCN(4-3) line cube. α and δ are the right ascension and declination, respectively. T_{peak} is the peak temperature detected in the HCN(4-3) line cube in K. v and Δv are the central velocity and FWHM of the clouds, respectively, in km s^{-1}. $R_{\rm dc}$ and R are the deconvolved and not deconvolved radii of the HCN(4-3) cloud, as characterized in CPROPS. For those clouds which are not resolved, we use the equations shown in Section 4.1.2 and take the deconvolved radii as an upper limit. $L_{HCN(4-3)}$ is the HCN(4-3) luminosity in K km s^{-1} pc^{-2}. 96

List of Figures

1.1 Scheme of the effect of metallicity on CO and H_2 areas in a spherical clump in a uniform radiation field, from Bolatto et al. (2013). Blue shading represents where hydrogen gas is molecular. Panel a illustrates the effect of increasing metallicity and dust-to-gas ratio. Panel b shows the effect of increasing the size of the molecular cloud at fixed metallicity. 11

1.2 Herschel 160 μm map of the SMC from Meixner et al. (2013). White contours represent the HI column density map constructed using the Parkes Galactic All-Sky Survey (GASS) first data release (McClure-Griffiths et al. 2009). The contour levels are (1, 1.5, 2, 2.5 and 3) $\times 10^{21}$ cm^{-2}. The yellow circular region marks the position of Magellanic Bridge A (labeled MagBridge A). 12

1.3 B/V/Hα (=b/g/r) three color HST image of 30 Doradus from Kalari et al. (2018) (by Jesús Maíz Apellániz), spanning $2.5' \times 2.5'$ approximately. R136 is visible as the bright star cluster at α = 5h42m00s and $\delta = -69^{\circ}06'00''$. The red box marks the area covered by the ALMA images used in this work, described in Section 2. 14

2.1 ALMA continuum images at 1.3 mm of Magellanic Bridge A, generated using 12m data only (left) and 7m data only (right). All images are done with natural weight. White ellipse in each image represents the beam size. 18

2.2 ALMA continuum images at 1.3 mm of Magellanic Bridge A, generated using 12m and 7m data, where imaging is performed using natural weight. The left image corresponds to the continuum obtained combining the 12m and 7m array data (from Figure 2.1), without uv tapering. The middle image is the 12m and 7m array continuum with its visibility data tapered using a Gaussian with an on-sky FWHM of 5". The right image is the tapered continuum image convolved to reach a resolution of 22". The white ellipse in the bottom left corner represents the beam size. Dashed contours correspond to continuum emission in the APEX 870 μm map at 25, 30, and 35 mJy/beam. 18

2.3 ALMA CO(2-1) channel maps of Magellanic Bridge A. The velocity range is 171 to 177 km s^{-1}, with 1 km s^{-1} interval between images. (a) Line cube made with 12m data only. (b) Line cube made with 7m data only.(c) Line cube made with the combined 12m array and 7m array datasets. 20

2.4 APEX-LABOCA continuum image at 870 μm, obtained from Verdugo (2012). The white scalebar represents a 10 pc length. The white circle represents the beam size. 21

2.5 APEX CO(2-1) line observations of Magellanic Bridge A. Channel maps are shown in the velocity range 171 to 177 km s^{-1}, with an interval of 1 km s^{-1} per image. 22

2.6 Final CO(2-1) line cube of Magellanic Bridge A, which is the combination between the ALMA 12m and 7m array data with the APEX observations of the CO(2-1) line emission. The velocity range is 171 to 177 km s^{-1} with 1 km s^{-1} spacing. 23

2.7 Velocity integrated images of the ALMA ^{12}CO(3-2) line cube of 30Dor, every 5 km s^{-1}. Each row has its own intensity range: the first and third row go from 0 to 5 Jy $beam^{-1}$ km s^{-1} and the second row goes from 0 to 40 Jy $beam^{-1}$ km s^{-1}. 25

2.8 ALMA 880 μm continuum image of 30 Doradus in the vicinity of R136. The red scalebar represents a 2 pc length. The white ellipse represents the beam size. 26

3.1 Herschel continuum images of Magellanic Bridge A at 100, 160, 250, 350, and 500 μm, together with the LABOCA continuum image at 870 μm. The cyan contours correspond to the LABOCA 870 μm continuum image at 25 (5σ), 30 (6σ), and 35 mJy/beam (7σ). The dashed circles indicate the beam sizes for each image, which correspond to a FWHM of 9" (100 μm), 14" (160 μm), 22" (250 μm), 30" (350 μm), 43" (500 μm) and 22.4" (870 μm). The scale bar in the bottom right panel indicates a 10 pc length. 29

3.2 APEX-LABOCA continuum image at 870 μm. The white circle shows the position and size of the circular aperture used for the aperture photometry of the Magellanic Bridge A source. The black circles show the position and size of the circular aperture used for the aperture photometry of sources North and South. The scalebar represents a 10 pc length. 31

3.3 SEDs for Magellanic Bridge A and the North and South sources. The points correspond to the energy νS_ν derived from the measured flux density S_λ, obtained using aperture photometry. Red points correspond to νS_ν obtained using Herschel data. Dark blue points correspond to the energy νS_ν obtained using the LABOCA image. The purple arrow corresponds to the νS_ν upper limit at 1.3 mm using the ALMA continuum image. The left panel shows the Magellanic Bride A SED, for which we used the 100, 160, 250, 350 and 500 μm Herschel continuum images, the 160 μm Spitzer continuum image, the 870 μm (LABOCA) and 1.3 mm (ALMA) continuum images with a common resolution of 43". We measure the flux density from Magellanic Bridge A inside a circular aperture of radius $r = 50$". The North and South sources SEDs are shown in the last two panels, constructed with the Hershel 100, 160 and 250 μm continuum images, the 870 μm (LABOCA) and 1.3 mm (ALMA) continuum images at a common resolution of 22". We measure the fluxes from sources North and South in a circular aperture of radius $r = 11$". The MBB model that best fits the Herschel points for each source is shown as a black curve. The parameters of each curve are in Table 3.3. 34

3.4 Velocity integrated intensity image of the combined ALMA and APEX CO(2−1) cube of Magellanic Bridge A, integrated between 172 and 176.0 km s^{-1}. The cyan contours correspond to 5 times the σ of the integrated image (σ = 48 mJy/beam km s^{-1}). The white contours correspond to the LABOCA 870 μm continuum image at 25, 30 and 35 mJy/beam, as in Figure 3.1. The white ellipse in the lower left corner represents the beam FWHM (1.22" × 1.15"). The scale bar on the lower right corner indicates a 2 pc length. 37

3.5 CO(2-1) integrated spectra for Magellanic Bridge A clouds North and South. The black lines correspond to the flux density measured in each channel. The red dashed lines represent the Gaussian fits of the spectra. (a) Spectra for CO cloud North. (b) Spectra for CO cloud South. 39

3.6 LABOCA continuum image at 870 μm, with black contours placed at 25, 30 and 35 mJy/beam, as in Figure 3.1. The white circle represents the beam size (beam FWHM= 22"). Red contours correspond to the ALMA and APEX CO(2−1) combined line emission convolved to the APEX resolution of 22", integrated between 172 and 176 km s^{-1}, at 5σ, 6σ and 7σ, where σ is the rms of the integrated image (σ = 1.8 Jy $beam^{-1}$ km s^{-1}). The scalebar in the lower right corner represents a 5 pc length. 43

4.1 ALMA ^{12}CO(3-2) line cube of the vicinity of R136 in 30Dor, integrated between 217 and 285 km s^{-1}. Cyan points with white edges represent the position of the detected clumps in Table 4.1. Each point is labeled according to the corresponding detection no. from Table 4.1. The red solid ellipse in the lower right corner represents the ^{12}CO(3-2) line cube beam FWHM in its major and minor axes. The yellow cross represents the central position of R136. The red scalebar represents a length of 2 pc. 46

4.2 Velocity integrated ^{12}CO(3-2) images of the vicinity of R136 in 30Dor, in the locations of the 5 clouds we characterize manually, together with their integrated spectra. Black points correspond to the integrated spectra in each region. (a) ^{12}CO(3-2) emission integrated between 236.7 and 250.9 km/s of clouds 16, 17 and 18. The top spectra corresponds to the integrated spectra inside the cyan contour, and the bottom spectra corresponds to the red contour. The bottom spectra shows a complex profile, fitted with 4 Gaussian components, each of which is associated with a cloud. (b) ^{12}CO(3-2) emission integrated between 223.6 and 230.9 km/s for clouds 7 and 8, together with the integrated spectra in the red region. The spectra shows two gaussian components, 0 and 1, associated with clouds 8 and 7, respectively. 49

4.3 Relationships between the physical properties observed in the resolved clouds found near R136 in 30Dor. Filled red circles correspond to completely resolved molecular clouds, whereas empty red circles correspond to molecular clouds where the minor axis is unresolved. Left: relationship between the radius R and the velocity FWHM Δv. The dashed line represents the relationship found for molecular clouds in the first Galactic quadrant by Solomon et al. (1987), $\Delta v = 1.69R^{0.5}$. Right: relationship between the virial mass M_{vir} and the ^{12}CO(3-2) luminosity $L_{^{12}CO(3-2)}$. Green dots plot the relation between M_{vir} and $L_{^{12}CO(1-0)}$ for resolved (filled circles) and not resolved (empty circles) clouds, where the luminosities $L_{^{12}CO(3-2)}$ are transformed to $L_{^{12}CO(1-0)}$ using $R_{\frac{3-2}{1-0}} \sim 2$ (Johansson et al. 1998). Dashed line represents the relationship found for molecular clouds in the first Galactic quadrant by Solomon et al. (1987), $M_{vir} = 39(L_{^{12}CO(1-0)})^{0.81}$. 53

4.4 Velocity integrated images of the different molecular species studied in the vicinity of R136 in 30Dor. Orange labeled dots correspond to the central position of the ^{13}CO(3-2) CPROPS detections. Green labeled dots mark the central position of the CS(7-6) CPROPS detections. Red labeled dots show the central position of the HCO$^+$(4-3) CPROPS detections. Purple labeled dots correspond to the central position of the HCN(4-3) CPROPS detections. The red ellipse in the lower left corner represents the beam size. 55

4.5 Central position of the clouds found in ^{12}CO(3-2), ^{13}CO(3-2), CS(7-6), HCO$^+$(4-3) and HCN(4-3) line observations of the vicinity of R136 in 30Dor. Contours correspond to 3, 5, 10, 20 and 30 times the rms of the image generated by integrating the ^{12}CO(3-2) line cube between 217 and 285 km s^{-1} (rms = 4.92 Jy beam^{-1} km s^{-1}). Blue crosses mark the central position of the clouds found in the ^{12}CO(3-2) in Section 4.1.1. Yellow arrowheads point towards the central position of ^{13}CO(3-2) clouds. Green arrowheads point towards the central position of CS(7-6) clouds. Red arrowheads point towards the central position of HCO$^+$(4-3) clouds. Purple arrowheads point towards the central position of HCN(4-3) clouds. The dashed ellipse in the lower left corner represents the beam size of the ^{12}CO(3-2) line cube. 56

4.6 ALMA 880 μm continuum image of the vicinity of R136. White contours represent 1.5, 3, 4 and 5 σ levels (σ = 4 mJy/beam), with labels indicating the contours that correspond to clouds A, B, C, D, E and F. The white ellipse in the lower left corner represents the beam size. The scalebar in the lower right corner represents a 2 pc length. 63

4.7 Free-free emission images generated from Brγ emission (left) and Radio continuum emission (right). The white dashed contours are the same contours as in Figure 4.6. 65

4.8 Velocity integrated images of ^{12}CO(3-2) emission for clouds no. 2, 15, 16, 17, 18, 22 and 23. The red contours correspond to 3, 5 and 10σ, where σ is the rms of each velocity integrated image (given in the respective captions). White contours correspond to the 1.5 and 3σ contours of the ALMA 880 μm continuum image, as in Figure 4.6. Dashed cyan ellipses represent the size of the major and minor axes found in Section 4.1.1. 69

4.9 Velocity integrated images of the ALMA ^{12}CO(3-2) line shown previously in Figure 2.7. White dashed labeled ellipses represent the position and sizes of the major and minor axes of the clouds described in Section 4.1.1. 72
4.10 Central velocity and virial mass plotted as a function of projected distance from R136a 73
4.11 Relationships between physical properties of our sample, together with results in this same region found in Kalari et al. (2018), in 30Dor from Nayak et al. (2016) with $\sim$ 2" resolution ($\sim$ 0.5 pc) and Pineda et al. (2009) with 45" resolution ($\sim$ 15 pc), in the LMC from Wong et al. (2011). (a) Size-linewidth R vs σ_v relationship for molecular clouds in different galaxies, including our results and other regions in 30Dor, the LMC and the Mikly Way. The black line represents the canonical relation $\sigma_v = 0.72R^{0.5}$, followed by the Milky Way clouds. (b) σ_v^2/R vs Σ_{H_2} relationship for molecular clouds in different galaxies, including our results and other regions in 30Dor, the LMC and the Milky Way. The solid black line represents the approximate σ_v^2/R value for increasing Σ_{H_2} of an isolated virialized cloud confined by self-gravity. Dashed lines mark the external pressure required to confine a cloud for a given σ_v^2/R value, assuming a centrally concentrated cloud in hydrostatic equilibrium. Dashed lines cover the range $P/k_B = 1 \sim 10^3 - 10^9$ cm^{-3} K. 74
4.12 M_{gas}/M_{vir} ratio for molecular clouds found in the LMC, SMC and the Milky Way. M_{gas} is the total gas mass determined through dust emission and M_{vir} is the virial mass. We include the ratios found by Bot et al. (2007) in the SMC in cyan, Herrera et al. (2013) in N11 in blue, Milky Way values calculated in Bot et al. (2007) in green and our values in magenta stars. Our clouds are labeled according to their 880 μm continuum labels. The horizontal black line marks the $M_{gas}/M_{vir} = 1$ equality. 80
4.13 Velocity integrated image of ^{12}CO(3-2) emission between 235 and 250 km s^{-1}. White dashed ellipses represent the position and sizes of the major and minor axes of the molecular clouds no. 10, 11, 12, 14, 15, 17 and 18 found in Section 4.1.1. The white numbers over the ellipses are the cloud labels. Red points indicate the IR sources from the Rubio et al. (1998) catalog, with their corresponding lables in bold red letters. White stars represent the YSO candidates from the Gruendl & Chu (2009) Spitzer catalog, with the corresponding labels in white. The white ellipse in the bottom left corner represents the beam size. 81

B.1 Peak position spectra for cloud no. 1, with best fit Gaussian profile. 97
B.2 Peak position spectra for cloud no. 2, with best fit Gaussian profiles. 97
B.3 Peak position spectra for cloud no. 3, with best fit Gaussian profile. 98
B.4 Peak position spectra for cloud no. 5, with best fit Gaussian profiles. 98
B.5 Peak position spectra for cloud no. 8, with best fit Gaussian profiles. 98
B.6 Peak position spectra for cloud no. 9, with best fit Gaussian profile. 98
B.7 Peak position spectra for cloud no. 10, with best fit Gaussian profiles. The individual spectra for each molecule is in Figure B.21. 99
B.8 Peak position spectra for cloud no. 11, with best fit Gaussian profiles. The strong emission at $\sim$ 246 km s^{-1} corresponds to cloud no. 10. 99
B.9 Peak position spectra for cloud no. 12, with best fit Gaussian profiles. 99
B.10 Peak position spectra for cloud no. 13, with best fit Gaussian profile. 99

B.11 Peak position spectra for cloud no. 14, with best fit Gaussian profiles. 100
B.12 Peak position spectra for cloud no. 15, with best fit Gaussian profiles. 100
B.13 Peak position spectra for cloud no. 16, with best fit Gaussian profiles. 100
B.14 Peak position spectra for cloud no. 17, with best fit Gaussian profiles. 100
B.15 Peak position spectra for cloud no. 18, with best fit Gaussian profiles. The peak at 245 km s^{-1} corresponds to cloud no. 17, whereas the peak at 241 km s^{-1} is from cloud no. 18. 101
B.16 Peak position spectra for cloud no. 19, with best fit Gaussian profile. 101
B.17 Peak position spectra for cloud no. 20, with best fit Gaussian profile. 101
B.18 Peak position spectra for cloud no. 21, with best fit Gaussian profiles. 101
B.19 Peak position spectra for cloud no. 22, with best fit Gaussian profiles. 102
B.20 Peak position spectra for cloud no. 23, with best fit Gaussian profiles. 102
B.21 Peak position spectras for cloud no. 10, separated by molecular species, with best fit Gaussian profiles. 102

Chapter 1

Introduction

The space between stars in galaxies is not empty. The Interstellar Medium (ISM) is the matter that fills the space between stars and is composed mainly of gas, but also contains dust, cosmic rays and magnetic fields. The gas in the ISM can be in the form of molecular clouds, neutral gas or ionized medium (Lequeux 2005). We are interested in molecular clouds, as these are the regions in the ISM where stars form. The currently accepted models indicate that stars form when a molecular cloud undergoes gravitational collapse (McKee & Ostriker 2007; Shu et al. 1987). Therefore, to understand the process of star formation, it is necessary to study the conditions of the ISM.

The life of a star is a cyclic process: stars are born from collapsing gas present in between existing stars in the ISM and, at the end of their lifetime, they return this gas back, enriched with elements heavier than Hydrogen and Helium. When stars die, they return part of the mass they have through supernovae or planetary nebula ejection. This enriched material is then used to form stars, so each generation of stars contributes to the chemical enrichment of the ISM they are embedded in and also contributes to increase the metallicity of the stars formed within the ISM. For a fixed galaxy mass, galaxies at higher redshifts (which means closer in time to the Big Bang) tend to have lower metallicities than at lower redshifts (closer to the present time, eg. Savaglio et al. 2005; Zahid et al. 2013). This means that the first generation of stars in the Milky Way (Population III stars) and stars in high-redshift galaxies are formed out of less metal-enriched gas than stars that are forming today. As a result, to understand star formation and molecular clouds at high-redshift and young galaxies, where the gas was less metal-enriched, it is fundamental to study star formation and molecular clouds at low-metallicity galaxies (meaning metallicities lower than half the solar value $Z_{\odot} = 0.02$) in the Local Group, where individual molecular clouds can be detected.

1.1 Molecular clouds

Molecular clouds are regions where molecular gas is self-gravitating and shielded from far-ultraviolet (FUV) radiation. These regions tend to be cold ($\sim 10-20$ K) and dense ($n > 200$ cm^{-3}, Tielens 2005). This way, molecules can form without being photo-dissociated and stars can form from collapsing, cold gas.

The main component of molecular clouds is molecular Hydrogen (H_2). Unfortunately, H_2 is not directly observable in emission. H_2 is a diatomic, non-polar molecule, and therefore does not possess any dipolar rotational transitions. The lowest energy transition of H_2 is the first rotational quadrupole transition ($J = 2 \rightarrow 0$), which is only excited in gas where $T \geq 100$ K and thus does not trace the cold molecular gas component of the ISM. Fortunately, under the conditions present in molecular clouds, other molecules form, the most abundant of them being carbon monoxide (CO). This molecule is the most used tracer of molecular gas, as it is observable under the conditions prevalent in molecular clouds. CO has a small permanent dipole moment ($\mu \approx 0.11$ D), so it possesses dipolar rotational transitions, and the lowest rotational state is only 5.5 K above the ground state, making the $J = 1 \rightarrow 0$ transition observable at low temperatures.

Interstellar dust is another commonly used molecular gas tracer. Dust is heated by stellar radiation in the far-UV and re-emits thermal radiation at the far infrarred (FIR) and millimeter wavelengths. It is expected that dust is spatially correlated with H_2 because dust grains act as catalysts for H_2 formation: H atoms stick to the grain surface, react with other H atom and form the H_2 molecule, which can then leave the grain through evaporation or collisions. Also, dust protects the molecules inside the molecular cloud by absorbing far-UV radiation, avoiding their photodissociation.

1.2 Physical properties of CO molecular clouds

CO is the most commonly used tracer of molecular gas. Its lowest energy rotational transition, CO($J = 1 \rightarrow 0$), emits at 2.6 mm (115 GHz) and is optically thick. From CO emission, we can obtain the size, CO luminosity, total gas mass and density of the cloud. In the following, we explain how to obtain these physical properties.

1.2.1 Size

We explain two commonly used methods to calculate the size of a molecular cloud.

One way to obtain the size of the clouds is assuming a spherical cloud shape. The area of the cloud is defined as the number of spectra in the line cube which belong to one cloud, multiplied by the area occupied by a pixel in the image. The spectras that belong to a cube are usually defined as the spectra which present emission over a certain threshold signal T_{edge}. Then, we calculate the equivalent radius R_{eq}, which is the radius of a sphere that has the observed area, as:

$$R_{\mathrm{eq}} = \sqrt{\frac{A}{\pi}}. \tag{1.1}$$

This size definition works best when clouds are circular, because it tends to overestimate the size of the cloud when it is has an ellipsoidal spatial brightness distribution.

When the cloud has an ellipsoidal shape, a way to calculate the size of the cloud is to measure the second moments of the CO line emission along the major and minor spatial axes of the cloud, σ_{maj} and σ_{min}. In this method, the area of the cloud is the ellipse described by

σ_{maj} and σ_{min}. Once determined, the radius is calculated using:

$$R = 1.91\sigma_r, \tag{1.2}$$

(Rosolowsky & Leroy 2006) where $\sigma_r = \sqrt{\sigma_{maj}\sigma_{min}}$ is the geometric mean of the second moments of emission and D is the distance to the cloud in pc. The factor that relates the geometric mean of σ_{maj} and σ_{min} to the spherical radius of the cloud, for a density profile $\rho \propto r^{-1}$, is 1.91 (Solomon et al. 1987).

1.2.2 CO intensity and luminosity

The brightness temperature at α, δ and v is related to the flux density of the source S_ν at frequency ν through the Rayleigh-Jeans law:

$$T_{MB} = \frac{c^2}{2k_B\nu^2\Omega}S_\nu, \tag{1.3}$$

where Ω is the solid angle of the source, c is the speed of light in vacuum and k_B is the Boltzmann constant.

The velocity integrated intensity of CO, I_{CO}, is defined as:

$$I_{CO} = \int T_{MB}(\alpha, \delta, v)\,\mathrm{d}v, \tag{1.4}$$

where T_{MB} is the measured main-beam brightness temperature of the CO line at velocity v and sky position (α, δ).

The CO luminosity of a molecular cloud, L_{CO}, is the sum of the CO intensity inside the area of the cloud:

$$L_{CO} = \int\int T_{MB}(\alpha, \delta, v)\,\mathrm{d}v\,\mathrm{d}A = \int I_{CO}(\alpha, \delta)\,\mathrm{d}A. \tag{1.5}$$

When the area of the cloud is defined through the solid angle subtended by the cloud Ω, we rewrite $\mathrm{d}A = D^2\mathrm{d}\Omega$. Therefore, replacing T_{MB} from Equation 1.3 in Equation 1.5, the CO luminosity can be calculated using the flux density:

$$L_{CO} = D^2 \int I_{CO}\,\mathrm{d}\Omega = \frac{c^2}{2k_B\nu^2}\int S_\nu\,\mathrm{d}v. \tag{1.6}$$

1.2.3 Cloud mass

There are several ways to obtain the total gas mass of a molecular cloud. These are (1) using the CO luminosity, (2) using the virial theorem, (3) using dust emission, and (4) assuming Local Thermodynamic Equilibrium (LTE) inside the cloud. We explain how to obtain the gas mass of a cloud through these methods in the following.

1. Gas mass from CO luminosity

The most common way to obtain the gas mass of a molecular cloud is using the CO $J = 1 \rightarrow 0$ rotational transition luminosity (from now on, CO(1-0)). CO(1-0) is optically thick, so we count the number of clouds inside the beam through the CO intensity. As a result, the CO(1-0) intensity is related to the H_2 column density $N(H_2)$:

$$N(H_2) = X_{CO} \int T_{MB} \, \mathrm{d}v = X_{CO} I_{CO}. \tag{1.7}$$

X_{CO} is known as the CO-to-H_2 conversion factor and has units of cm^{-2} $(\mathrm{K\ km\ s}^{-1})^{-1}$. To obtain the mass of the cloud, we integrate $N(H_2)$ over the area of the cloud and multiply by the mass of the H_2 molecule, m_{H_2}:

$$M_{CO} = X_{CO} m_{H_2} \int I_{CO} \, \mathrm{d}A = \alpha_{CO} L_{CO}, \tag{1.8}$$

where we replace L_{CO} from Equation 1.5 and define the CO-to-H_2 conversion factor in terms of the CO luminosity as α_{CO}, which has units of $M_\odot$ $(\mathrm{K\ km\ s}^{-1}\ \mathrm{pc}^2)^{-1}$. Both α_{CO} and X_{CO} are known as the CO-to-H_2 conversion factor.

The CO-to-H_2 conversion factor in the galaxy is $X_{CO} \approx 2 \times 10^{20}$ cm^{-2} $(\mathrm{K\ km\ s}^{-1})^{-1}$, or $\alpha_{CO} \approx 4.3$ $M_\odot$ $(\mathrm{K\ km\ s}^{-1}\ \mathrm{pc}^2)^{-1}$, and has been determined through different methods. This value is referred to as the canonical conversion factor. This conversion factor, however, is not universal. For low-metallicity galaxies, this factor appears to be higher, although the relation between X_{CO} and metallicity shows a large scatter (Bolatto et al. 2013).

2. Virial mass

One of the ways to obtain the total gas mass of a molecular cloud is through the virial theorem. We assume the cloud is in virial equilibrium, neglecting the effect of external forces, like magnetic fields. The simplest form of the virial theorem is:

$$2K + U = 0, \tag{1.9}$$

where K is the total kinetic energy of the cloud and U is its potential energy, in this case, dominated by self-gravity. For a spherical cloud in virial equilibrium, the kinetic energy is:

$$K = \frac{3}{2} M_{vir} \sigma_v^2, \tag{1.10}$$

where M_{vir} is the total gas mass of the cloud under virial equilibrium, which we call the virial mass from now on, and σ_v is the velocity dispersion of the CO line profile. The velocity dispersion of the CO emission line reflects the velocity dispersion of the gas inside of the cloud (see Bolatto et al. 2013, and references within). The gravitational energy of this cloud is

$$U = \frac{aGM_{vir}^2}{R}, \tag{1.11}$$

where G is the gravitational constant, R is the spherical radius of the cloud, and a is a constant that depends on the mass density profile of the cloud. Replacing Equations 1.10 and 1.11 in Equation 1.9 and solving for M_{vir}, we obtain:

$$M_{vir} = \frac{3\sigma_v^2 R}{aG} = \frac{k_1 \sigma_v^2 R}{G}, \tag{1.12}$$

where we replace the constant $3/a$ with k_1, which is the parameter we will adjust depending on the density profile of the cloud (MacLaren et al. 1988). This method can overestimate the total gas mass of the cloud if the external forces over the cloud are not negligible.

For a density profile $\rho \propto r^{-1}$, $k_1 = 3/2$. Replacing all constant values and calculating the mass based on the velocity FWHM Δv we obtain:

$$M_{vir} = 190R(\Delta v)^2, \tag{1.13}$$

(MacLaren et al. 1988) where Δv is in km s^{-1}, R is in pc and M_{vir} is in solar masses $M_\odot$.

3. Gas mass from dust emission

Gas mass can be obtained from the total dust mass of a molecular cloud. For this, it is necessary to know the dust emissivity per H nucleon ε_ν, which is related to the absorption coefficient $\kappa_{\rm d}(\nu)$ as:

$$\kappa_{\rm d}(\nu) = \frac{\varepsilon_\nu}{x_{\rm d}\mu m_H}, \tag{1.14}$$

where μm_H is the mass of the Hydrogen atom, multiplied by a factor to consider the contribution of Helium atoms to the gas mass[1], and

$$x_{\rm d} = \frac{M_{\rm d}}{M_{gas}} \tag{1.15}$$

is the dust-to-gas mass ratio. Replacing the resulting dust mass from Equation 1.31 and replacing $\kappa_{\rm d}(\nu)$, the total gas mass from dust emission is:

$$M_{gas} = \frac{M_{\rm d}}{x_{\rm d}} = \frac{S_\nu D^2 \mu m_H}{\varepsilon_\nu B(T_{\rm d})} \tag{1.16}$$

M_{gas} depends on the dust-to-gas ratio, which varies with metallicity, and the absorption coefficient $\kappa_{\rm d}(\nu)$, which varies according to the emission frequency and the properties of the dust grains.

4. LTE gas mass

Another method to calculate the total gas mass of a molecular cloud is to obtain the H_2 column density $N(H_2)$. Unfortunately, this cannot be done with ^{12}CO line emission alone, because CO emission lines are usually optically thick (which means that their optical depth $\tau_\nu \gg 1$) and therefore trace only the surface of the molecular cloud. To trace the column density of a cloud, we need an optically thin ($\tau_\nu < 1$) molecular emission together with the ^{12}CO observations. The most common ^{12}CO isotopologue used for this is the ^{13}CO molecule. The idea is to obtain the column density of ^{13}CO, $N(^{13}CO)$, and transform it into $N(H_2)$.

To convert the observed intensity into column density, we require the density and temperature of the cloud along the line of sight, which might vary. A simple approximation is

[1]The value of μ is usually considered = 1.36

to assume LTE, the assumption that a single excitation temperature T_{ex} describes how the different rotational transitions of ^{13}CO are populated along the line of sight. We also assume that ^{13}CO and ^{12}CO share the same T_{ex} for the same $J \to J-1$ rotational transition, which is reasonable when collisions dominate the excitation of the gas, so $T_{ex} \approx T_K$, the kinetic temperature of the gas. In molecular clouds, this assumption is usually safe due to their high density.

For a ^{12}CO $J \to J-1$ transition with frequency ν, the excitation temperature relates to the main-beam brightness temperature T_{MB} obtained by the telescope through:

$$T_{MB} = T_0\Big(\frac{1}{\mathrm{e}^{T_0/T_{ex}}-1} - \frac{1}{\mathrm{e}^{T_0/T_{BG}}-1}\Big)(1-\mathrm{e}^{-\tau_\nu}), \tag{1.17}$$

(Wilson et al. 2009) where T_{BG} is the cosmic microwave background temperature, which is ≈ 2.7 K, and

$$T_0 = T_0(\nu) = \frac{h\nu}{k_B}. \tag{1.18}$$

k_B is the Boltzmann constant and h is the Planck constant. The term $1/(\mathrm{e}^{T_0/T_{BG}}-1)$ is a constant, so we can replace it with a constant value c. To obtain the excitation temperature, we require the ^{12}CO brightness temperature, as it is optically thick. This way, assuming $\mathrm{e}^{-\tau} \to 0$, we isolate T_{ex} from Equation 1.17 and find:

$$T_{ex}(\nu) = \frac{T_0}{\ln(1+\frac{T_0}{T_{MB,CO}+cT_0})}. \tag{1.19}$$

Having the excitation temperature, we can calculate the column density in the ^{13}CO line intensity. For the ^{13}CO(3-2) line emission, the ^{13}CO column density $N(^{13}CO)$ in cm^{-2} is calculated using:

$$N(^{13}CO) = 8.28\times10^{13}\mathrm{e}^{\frac{15.85}{T_{ex}}}\frac{T_{ex}+0.88}{1-\mathrm{e}^{\frac{-15.85}{T_{ex}}}} \times \frac{1}{J(T_{ex})-J(T_{BG})} I_{^{13}CO(3-2)}, \tag{1.20}$$

(Celis Peña et al. 2019) where $I_{^{13}CO(3-2)} = \int T_{MB}(^{13}CO(3-2))\,\mathrm{d}v$ is the integrated line intensity and

$$J(T) = \frac{h\nu/k}{\mathrm{e}^{h\nu/kT}-1}, \tag{1.21}$$

where, for $\nu = 330.588$ GHz (the rest frequency of the ^{13}CO(3-2) line), $h\nu/k = 15.85$ K. This equation assumes that the optical depth of the ^{13}CO(3-2) line $\tau_{^{13}CO(3-2)} \ll 1$. The $N(H_2)$ is obtained from the $N(^{13}CO)$ column density assuming a $H_2/^{13}$CO abundance ratio.

1.2.4 Surface and volume density

With the size and the gas mass obtained through any of the methods above, we can obtain the surface density Σ_{H_2} and the bulk volume density $n(H_2)$.

The surface density is defined as the number of molecules in the area of the cloud. We calculate it based on the mass of the cloud M using:

$$\Sigma_{H_2} = \frac{M}{A m_{H_2}} \tag{1.22}$$

where m_{H_2} is the mass of the H_2 molecule.

The bulk volume density $n(H_2)$ is the number of molecules inside the cloud volume. To obtain $n(H_2)$, we assume the molecular cloud is a sphere which has the radius R found using any of the methods shown in Section 1.2.1. Therefore, the bulk density of the cloud is:

$$n(H_2) = \frac{3M}{4\pi R^3 m_{H_2}}. \tag{1.23}$$

1.2.5 Correlations between physical properties

Empirically, velocity dispersions, clump sizes, virial masses and CO(1-0) luminosities of molecular clouds in the Milky Way are correlated. The velocity linewidths and clump sizes for galactic molecular clouds (GMC) in the Milky Way are found to follow a power-law $\Delta v \propto R^{\alpha}$, where the exponent α is around 0.5 (Solomon et al. 1987). This correlation is often known as "Larson's law", as it was first described by Larson (1981). The virial masses and CO luminosities are found to follow a power-law $M_{vir} \propto L_{CO}^{\alpha}$, where α is close to 0.81 (Solomon et al. 1987). These scaling relations appear to hold true in other galaxies (Bolatto et al. 2008).

1.3 Dust continuum emission

There are three different physical processes that can contribute to the flux density measured from molecular clouds in continuum images at submillimeter wavelengths: (1) thermal dust emission, (2) thermal free-free emission (3) non-thermal synchrotron emission. In this work, we are interested in dust emission, so the other contributions need to be subtracted from the fluxes we measure in molecular clouds. In the following, we describe the properties of these emission mechanisms and how to subtract those which not correspond to thermal dust.

1.3.1 Thermal dust emission

Dust grains absorb energy from the far-UV emission from nearby stars and re-emit this energy at longer wavelengths.

At millimeter and submillimeter wavelengths, we can assume that dust emission is optically thin, which means that the optical depth τ_ν at frequency ν is < 1. Under this condition, we can write the power per unit area, frequency and solid angle as

$$I_\nu = \tau_\nu B_\nu(T_{\rm d}), \tag{1.24}$$

where B_ν is the Planck's law value at the dust temperature $T_{\rm d}$. The optical depth is given by the dust absorption coefficient $\kappa_{\rm d}(\nu)$ and the mass density of the dust cloud ρ integrated

along the line of sight:

$$\tau_\nu = \int \kappa_{\rm d}(\nu)\rho \, {\rm d}s. \tag{1.25}$$

If we assume that both the density and the absorption coefficient are constant along the line of sight in the cloud, then the optical depth is written as:

$$\tau_\nu = \kappa_{\rm d}(\nu)\Sigma_{\rm d}, \tag{1.26}$$

where $\Sigma_{\rm d}$ is the mass surface density of the source. Replacing τ_ν in Equation 1.24 and integrating I_ν by the solid angle of the source Ω, we obtain the flux density of dust at frequency ν:

$$S_\nu = \Omega\kappa_{\rm d}(\nu)\Sigma_{\rm d}B_\nu(T_{\rm d}). \tag{1.27}$$

The simplest model to describe the dust emission in galaxies is the Modified Blackbody model (MBB), in which the absorption coefficient is a function of frequency:

$$\kappa_{\rm d}(\nu) = \kappa_{\rm d}(\nu_0)\Big(\frac{\nu}{\nu_0}\Big)^\beta \tag{1.28}$$

where $\kappa_{\rm d}(\nu_0)$ is the absorption coefficient at the reference frequency ν_0 and β is called the dust emissivity index. Thermal emission from dust has been empirically found to be well represented by this model, where β is expected to range from 1 to ~ 2.5 (Hildebrand 1983).

Replacing $\kappa_{\rm d}(\nu)$ and reorganizing the constant values Ω, $\Sigma_{\rm d}$, $\kappa_{\rm d}(\nu_0)$, and ν_0 as C, the flux density is a function of frequency ν, the dust emissivity index β and dust temperature $T_{\rm d}$ (Hildebrand 1983):

$$S_\nu = C\nu^\beta B_\nu(T_{\rm d}). \tag{1.29}$$

From Equation 1.27, we can obtain the total dust mass of a cloud. Writing the solid angle in terms of the cloud area $\Omega = A/D^2$, and replacing the dust mass $M_{\rm d} = A\Sigma_{\rm d}$:

$$S_\nu = \frac{A}{D^2}\kappa_{\rm d}(\nu)\Sigma_{\rm d}B(T_{\rm d}) = \frac{M_{\rm d}\kappa_{\rm d}(\nu)B(T_{\rm d})}{D^2}, \tag{1.30}$$

where D is the distance to the cloud and $M_{\rm d}$ is the dust mass of the cloud. We rearrange Equation 1.30 to obtain the dust mass:

$$M_{\rm d} = \frac{S_\nu D^2}{\kappa_{\rm d}(\nu)B(T_{\rm d})}. \tag{1.31}$$

1.3.2 Thermal free-free emission

Free-free emission, also known as Bremsstrahlung emission, is produced by free charged particles accelerated in the Coulomb field of another charged particle. The interaction with the field accelerates the free particles and these remain free after the interaction, hence the name free-free. For example, HII regions, which are ionized gas regions produced by the radiation of young stars, possess free electrons which can produce free-free radiation.

The power emitted by a single charge q is given by Larmor's formula:

$$P = \frac{2q\dot{u}}{3c^2}, \tag{1.32}$$

where $\dot{u}$ is the acceleration of the free charge and c is the speed of light in vacuum. The spectrum of free-free radiation is obtained from adding the power coming from particles with a thermal (Maxwellian) distribution of velocities. In cgs units, the resulting power per unit volume and frequency is:

$$\varepsilon_{ff}(\nu) = 6.8 \times 10^{-38} q^2 n_{\rm e} n_{\rm i} T_{\rm e}^{-1/2} {\rm e}^{-k\nu/k_b T_{\rm e}} \bar{g}_{ff} \tag{1.33}$$

(Rybicki & Lightman 1986) where $n_{\rm e}$ and $n_{\rm i}$ are the number densities of electrons and ions, respectively, $T_{\rm e}$ is the electron temperature in K and $\bar{g}_{ff}$ is the velocity-averaged Gaunt factor, which gives a quantum correction to the classical formulation. The Gaunt factor depends on $T_{\rm e}$ and ν in the optically thin regime as:

$$g_{ff} = 11.96 T_{\rm e}^{0.15} \nu^{-0.1} \tag{1.34}$$

There are three ways we can obtain free-free emission. The first one is through radio continuum images. For typical electrron temperatures of $\sim 10^4$ K, the optically thin free-free emission spectra is in centimeter-millimeter wavelengths. Due to the Gaunt factor (Equation 1.34), free-free emission flux density scales with frequency as $S_{ff} \propto \nu^{-0.1}$. Therefore, the free-free emission can be obtained from the flux density in a radio continuum image as:

$$S_{ff}(\nu_{ff}) = \left(\frac{\nu_{ff}}{\nu}\right)^{-0.1} S_\nu, \tag{1.35}$$

where ν_{ff} is the objective frequency where we want to obtain S_{ff} and S_ν is the flux density measured in a radio continuum image at frequency ν.

Another way to obtain the free-free emission flux is through Hα line emission. The intensity of the Hα line traces the warm ionized gas component of the ISM, so it is proportional to the free-free emission (see the Appendix in Hunt et al. 2004). To convert Hα flux density in erg cm^{-2} s^{-1} into free-free emission S_ν^{ff} in mJy, we use the following formula:

$$S_\nu^{ff} = 1.16 \left(1 + \frac{n({\rm He}^+)}{n({\rm H}^+)}\right) \left(\frac{T_{\rm e}}{10^4}\right)^{0.62} \nu^{-0.1} \left(\frac{S_\alpha}{10^{-12}}\right) \tag{1.36}$$

(Hunt et al. 2004) where S_α is the intensity of Hα in erg cm^{-2} s^{-1}, $T_{\rm e}$ is the gas electron temperature in K, $n({\rm He}^+)$ and $n({\rm H}^+)$ are the number density of Helium and Hydrogen ions, respectively, and ν is the objective frequency of free-free emission in GHz.

A third way to obtain the free-free emission flux density is through Brγ. For a typical HII region with an electronic temperature $T_{\rm e} = 10^4$ K and electron density $n_{\rm e} = 100$ cm^{-3}, the ratio between the Hα and Brγ line intensities is 101.78 (Osterbrock & Ferland 2006). Using this ratio, we can transform Brγ to Hα emission and use Equation 1.36 to obtain the free-free emission flux density.

1.3.3 Synchrotron emission

Synchrotron radiation consists of the radiation by relativistic charged particles accelerated in a magnetic field. In a magnetic field, a particle with charge q has a helical motion described by the frequency of rotation:

$$\omega_B = \frac{qB}{\gamma mc} \tag{1.37}$$

where B is the magnitude of the magnetic field, m is the mass of the particle and $\gamma = (1 - \frac{v^2}{c^2})^{-1/2}$ is the Lorentz factor.

The power emmited by a charge q, moving at relativistic speeds in a magnetic field, is:

$$P = \frac{2q^2}{3c^2}\gamma^4 \frac{q^2B^2}{\gamma^2 m^2 c^2} v_\perp^2 = \frac{2q^2}{3c^2}\gamma^2 a_\perp^2 \tag{1.38}$$

(Rybicki & Lightman 1986) where the particle acceleration is $a_\perp = \omega_B v_\perp$.

The total power emitted by an ensemble of electrons is given by the energy distribution $N(E)$, which is the number density of particles with energies between E and $E + \mathrm{d}E$, which for relativistic electrons can be expressed as a power-law:

$$N(E)\mathrm{d}E = CE^{-p}\mathrm{d}E \tag{1.39}$$

For this distribution, the total power emitted by the ensemble is proportional to the frequency of emission ν as $P \propto \nu^{-s}$, where the spectral index $s = (p-1)/2$.

Synchrotron radiation is detected in sources with strong magnetic fields, like in the vicinity of supernova remnants or active galactic nuclei. For the sources we observe in this thesis, synchrotron radiation is negligible.

1.4 Molecular clouds in low-metallicity environments

The study of molecular clouds at low-metallicity environments represents a challenge. CO is usually very faint and, therefore, difficult to detect in low-metallicity environments (see Rubio et al. 2015; Mizuno et al. 2006). As CO is optically thick, its brightness depends on its emitting area. When metallicity decreases, the abundances of carbon an oxygen atoms decrease, as well as the ratio between the amount of dust with respect to molecular gas. As there is less dust to shield the molecules, the CO molecule is more easily photo-dissociated, whereas the H_2 molecule has a stronger self-shielding capability. As a result, at low metallicities, the region where CO is emitting is smaller relative to the region of H_2 gas for a fixed cloud size (see Figure 1.1, Bolatto et al. 2013 and references within).

Dust emission in low-metallicity galaxies behaves differently than in the Milky Way. The current picture is that dust emission observed at far-infrared (FIR) and millimeter wavelengths is produced by grains in thermal equilibrium that emit as a MBB, where the dust emissivity depends on frequency ($S_\nu \propto \nu^\beta B_\nu(T)$), as explained in Section 1.3.1. This model, however, does not explain the observations of low-metallicity dwarf galaxies, in which dust emission at submillimeter and millimeter wavelengths often show an excess with respect to a

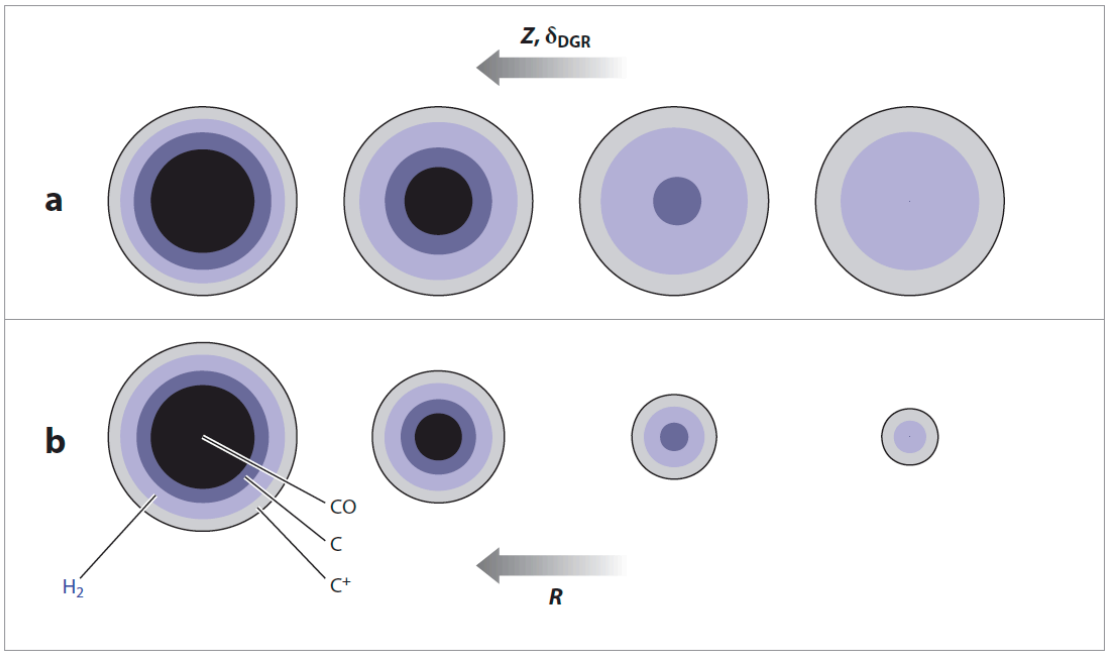

Figure 1.1: Scheme of the effect of metallicity on CO and H_2 areas in a spherical clump in a uniform radiation field, from Bolatto et al. (2013). Blue shading represents where hydrogen gas is molecular. Panel a illustrates the effect of increasing metallicity and dust-to-gas ratio. Panel b shows the effect of increasing the size of the molecular cloud at fixed metallicity.

modified blackbody expected emission (see Planck Collaboration et al. 2011; Bot et al. 2010b; Galametz et al. 2009; Lisenfeld et al. 2002), implying the presence of larger amounts of dust. For example, in the Magellanic Clouds, gas masses have been derived from dust emission in submillimeter and millimeter wavelengths, obtaining higher masses than those calculated from CO luminosities or virial masses (Bot et al. 2007; Rubio et al. 2004; Israel 1997). This emission has been attempted to be explained through several models, for example, through a second, colder dust component (Galliano et al. 2003, 2005), temperature-dependent emissivity in amorphous dust grains (Meny et al. 2007) and emission from magnetic nanoparticles (Draine & Hensley 2012). To achieve a good understanding of the molecular gas properties, both dust and CO emission must be studied.

The Magellanic System is the closest low-metallicity pair of galaxies we can study. It consists of the Large Magellanic Cloud (LMC) at ~ 50 kpc from the Milky Way (Pietrzyński et al. 2013), the Small Magellanic Cloud (SMC) at ~ 60 kpc (Cioni et al. 2000; Harries et al. 2003), and the Magellanic Bridge and Magellanic Stream, two components which might have been the result of the gravitational interaction between the Magellanic Clouds. The LMC has a metallicity $Z \approx Z_{\odot}/2$ (Rolleston et al. 2002), the SMC has $Z \approx Z_{\odot}/5$ (Dufour et al. 1982) and the Magellanic Bridge has a metallicity between $Z \approx Z_{\odot}/5$ and $Z \approx Z_{\odot}/10$ (Lee et al. 2005; Rolleston et al. 2003; Lehner et al. 2008). Due to their proximity to the Milky Way, they enable the study of molecular clouds in a range of low metallicities in great detail.

This work focuses on two regions of the Magellanic System, the Magellanic Bridge molecular cloud A and the vicinity of the young massive cluster (YMC) R136 in 30 Doradus. These two regions present different properties: the Magellanic Bridge has a lower metallicity

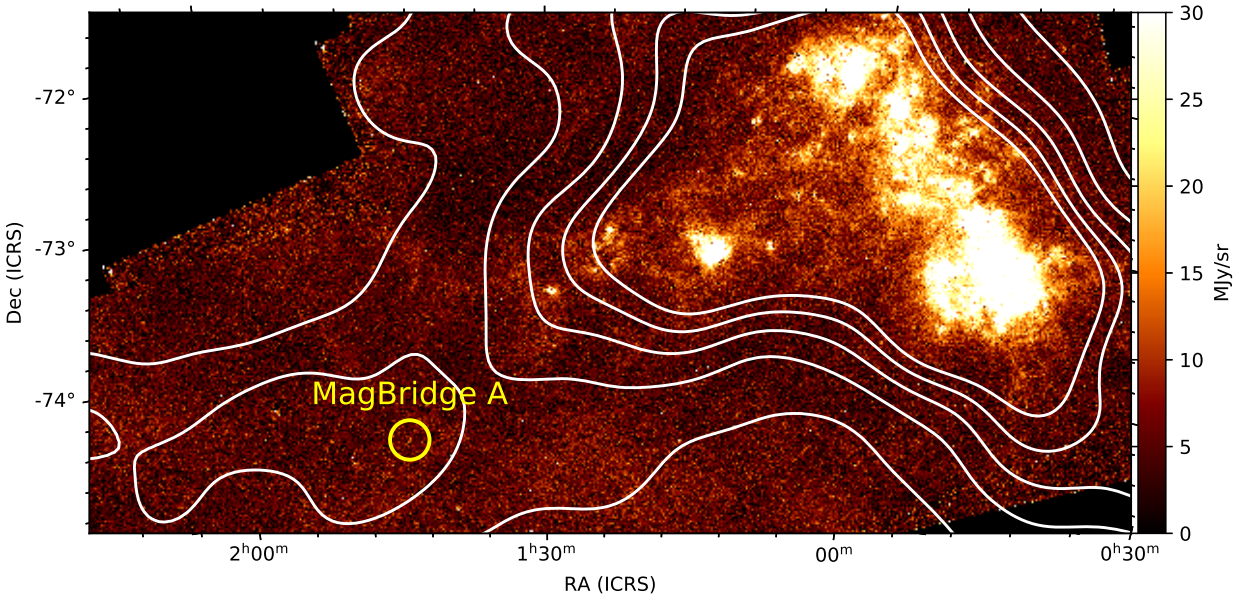

Figure 1.2: Herschel 160 μm map of the SMC from Meixner et al. (2013). White contours represent the HI column density map constructed using the Parkes Galactic All-Sky Survey (GASS) first data release (McClure-Griffiths et al. 2009). The contour levels are (1, 1.5, 2, 2.5 and 3) $\times 10^{21}$ cm^{-2}. The yellow circular region marks the position of Magellanic Bridge A (labeled MagBridge A).

and has a few, sparse OB type stars and compact HII regions, whereas the vicinity of R136 has a higher metallicity and strong UV radiation coming from the YMC. We describe the properties of the Magellanic Bridge in Section 1.5 and of 30 Doradus in Section 1.6.

1.5 The Magellanic Bridge

The Magellanic Bridge was first described through neutral hydrogen (HI) observations as a gaseous bridge joining the LMC and SMC (Hindman et al. 1963). It is a filamentary structure with lumps, holes, and shells, with an extent of 15 to 21 kpc, a total gas mass of $\sim 1.5 \times 10^8$ M$_\odot$, and an HI column density between 10^{20} and 10^{21} cm^{-2} (Staveley-Smith et al. 1998; Muller et al. 2003a). Simulations suggest that the Magellanic Bridge is the result of a close gravitational interaction between the LMC and SMC that happened around 200-300 Myrs ago (Murai & Fujimoto 1980; Gardiner et al. 1994; Besla et al. 2012). Star formation has and is taking place in the Magellanic Bridge: there are young stars and clusters of less than 100 Myr in age (Bica & Schmitt 1995; Harris 2007; Bica et al. 2015; Kalari et al. 2018) and evidence of current star formation in the form of Hα filamentary shells (Muller & Parker 2007) and young stellar objects (YSOs; Chen et al. 2014). At a distance of almost 60 kpc, using the SMC as reference (Harries et al. 2003; Cioni et al. 2000), the Magellanic Bridge is the closest low-metallicity tidally influenced region outside of a dwarf galaxy; it allows detailed studies of star formation under unique physical conditions.

The molecular component of the Magellanic Bridge has been studied through CO and dust emission, both tracers of H_2 gas, but these emissions are weaker than in the SMC main body

(Meixner et al. 2013; Muller et al. 2014) and, therefore, harder to detect. The first study that detected a molecular cloud in the Magellanic Bridge was done by Muller et al. (2003b), using ^{12}CO(1-0) observations. The detection was found in a region with an HI intensity peak and where the 60-to-100 μm intensity ratio was $S_{60\mu m}/S_{100\mu m} < 0.2$. Using a different criteria, matching HI and 100 μm intensity peaks, Mizuno et al. (2006) detected seven more ^{12}CO clouds which, together with the Muller et al. (2003b) detected cloud, have ^{12}CO(1-0) intensities between 30 and 140 mK km s^{-1} in a 2.6' beam. These molecular clouds have narrow velocity widths ($\Delta v \lesssim 2$ km s^{-1}), similar to the clouds in the metal-poor far edges of our galaxy, and molecular masses derived from their CO luminosities between $(1-7) \times 10^3$ M$_\odot$ (Mizuno et al. 2006), similar to the masses of nearby molecular clouds in the Milky Way (Mizuno et al. 1995, 2001). The eight clouds have been labeled from A to H, which is the naming convention that we use in this work. Mizuno et al. (2006) concluded that these clouds were recently formed in the Magellanic Bridge. All of the clouds except for one are within a few tens of parsecs to the closest OB stellar association (Bica & Schmitt 1995). YSO candidates have been found towards all of these sources, except for cloud D (Chen et al. 2014), showing the correlation of these molecular clouds with local star formation.

Magellanic Bridge A is the closest molecular cloud to the SMC (~ 3.5 kpc from the main body of the SMC; see Fig. 1.2) and one of the faintest of the molecular clouds detected by Mizuno et al. (2006), with a ^{12}CO(1$-$0) intensity of 30 mK km s^{-1} and a molecular mass of 10^3 M$_\odot$, estimated from its ^{12}CO(1$-$0) emission. It is located between two faint compact HII regions (Muller & Parker 2007) and is within a stellar association (Bica & Schmitt 1995). There is recent star formation in this region, revealed by two YSO candidates within the molecular cloud (Chen et al. 2014) and its proximity to HII regions and 24 μm bright sources (Muller et al. 2014). Verdugo (2012) found that Magellanic Bridge A has very high excess emission at 870 μm in comparison with other dust sources in the LMC and SMC.

1.6 R136 in 30 Doradus

30 Doradus (30Dor) is a giant HII region within the LMC, known to have the strongest star formation activity in the Local Group. An HII region, also known as a gaseous nebulae, is a well-defined region of ionized gas surrounding a hot star or a star cluster (Lequeux 2005). 30Dor has a diameter of ~ 200 pc and contains several filaments of ionized shells between 1 and 100 pc long (Chu & Kennicutt 1994). Because of this filamentary appearance, it is also called the Tarantula Nebula.

30 Doradus hosts the young massive cluster (YMC) R136, a 1.5 to 3 Myr cluster containing more than 100 massive stars (> 15 M$_\odot$, Walborn 1991). These stars ionize the surrounding gas, forming the gigantic HII region shown in Hα emission in Figure 1.3. The photoionizing luminosity produced by these massive stars (10^{51} ph s^{-1}), according to theoretical models (Dale et al. 2012), is sufficient to evacuate any dense molecular gas within a radius of 10-15 pc within 2 Myrs. Two massive molecular clouds are found to the northeast and southwest of R136, clouds 6 and 10 from Johansson et al. (1998), leaving a ~ 10 pc cavity around the YMC.

Surprisingly, higher sensitivity observations towards the R136 region revealed molecular clouds towards this cavity, between clouds 6 and 10. Rubio et al. (2009) found dense molecular

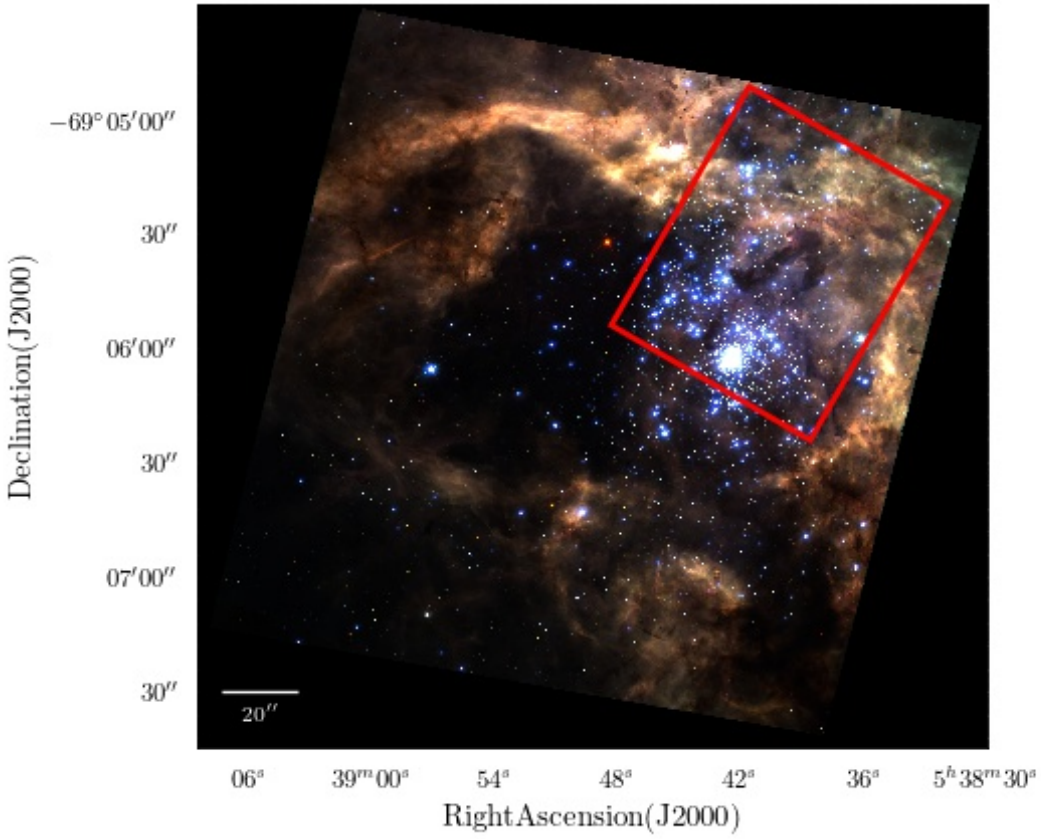

Figure 1.3: B/V/Hα (=b/g/r) three color HST image of 30 Doradus from Kalari et al. (2018) (by Jesús Maíz Apellániz), spanning $2.5' \times 2.5'$ approximately. R136 is visible as the bright star cluster at α = 5h42m00s and $\delta = -69^{\circ}06'00''$. The red box marks the area covered by the ALMA images used in this work, described in Section 2.

gas emission in this region, the closest to R136, associated to a young massive star, IRSW-127. They suggest that there is a high degree of clumpiness in this region. Kalari et al. (2018) investigated further this region through ^{12}CO(2-1) emission and found three knots, molecular clouds which spatially coincide with a dark area seen in optical emission.

1.7 Thesis goal and structure

The goal of this thesis is to study the physical properties of the molecular clouds in Magellanic Bridge A and in the vicinity of R136 in 30Dor through molecular gas and dust emission. This work is divided in two parts. The first one focuses on the molecular gas and dust emission, using data with different resolutions, in Magellanic Bridge A. The study of molecular cloud properties in Magellanic Bridge A is part of the paper Valdivia-Mena et al. (2020s, in press). The second part consists of the study of gas and dust at the same resolution in the vicinity of R136 in 30Dor.

The structure of this thesis is the following. In Chapter 2, we desribe the observations used for both regions, their reduction and imaging process, and complementary data. In Chapter 3, we present the characterization of the molecular clouds in Magellanic Bridge A

through CO(2-1) line and continuum emission, together with a discussion of the results for this region. In Chapter 4, we present the characterization of molecular clouds in the vicinity of R136 using CO(3-2) and continuum emission, together with results from other molecular species, and discuss their properties. In Chapter 5, we summarice our results from both regions and compare the molecular clouds found in both environments.

Chapter 2

Observations and Data Processing

In order to perform this study, we use a set of observations at different wavelengths. These observations trace the cold gas and dust content of the studied environments. We describe the observations used to study Magellanic Bridge A in Section 2.1 and the data used for 30Dor in Section 2.2.

2.1 Observations and data reduction for Magellanic Bridge A

In the following section, we describe the observations used to study the millimeter and submillimeter emission from Magellanic Bridge A. We summarize the main properties of the observations and describe the reduction process for the new data presented in this work.

2.1.1 ALMA observations

Magellanic Bridge A was observed with the Atacama Large Millimeter/Submillimeter Array (ALMA), located at Llano de Chajnantor in Atacama, Chile. We use Band 6 observations taken with the 12m array and the 7m array (also known as the Morita Array), which include continuum emission observations and the ^{12}CO(2-1) line emission data. In this thesis, we refer to the ^{12}CO(2-1) line as CO(2−1). Observations were performed in separate cycles: we used 7m array data taken during Cycle 1 and 12m array observations taken in Cycle 2. The datasets belong to project 2012.1.00683.S (PI M. Rubio). As the observations were obtained and reduced in different cycles, we decided to start from the raw data and completely reprocess both datasets, instead of using the delivered data products by ALMA.

The 12m observations were constructed with 33 antennas and consist of a mosaic of 93 pointings, with 13.7" spacing, and a total excecution time of 107 minutes. Uranus was used as flux calibrator, J0057−7040 as phase calibrator and J2357−5311 as bandpass calibrator.

The 7m observations were conducted with 10 antennas and consist of a mosaic of 34 pointings, with a distance of 23.4" between the center of each pointing, and a total integration time of 93.7 minutes. Uranus was also used as a flux calibrator for these observations. The

phase calibrator was J0102−7546 and the bandpass calibrator was J2357−5311.

We reduce, combine and image the data using the Common Astronomy Software Applications (CASA, McMullin et al. 2007) package version 4.7 , with the consideration that the software was released later than the observations. We use the standard scripts provided by the ALMA Science Archive[1] with the delivered raw data to recover the calibrated datasets. The 12m and 7m data are reduced separately.

We combine the calibrated 12m and 7m observations into one dataset. The observations are done using both the 12m and 7m array to have high-resolution data without losing extended emission: the 12m array configuration gives us observations with high resolution, yet it filters out diffuse emission that is larger than its maximum recoverable scale (MRS), which for our 12m observations is 18.3". The MRS increases to 30.9" after the 7m array data are combined with the 12m array observations. To combine data taken with two different arrays of antennas, it is crucial that the relative weights of each visibility are correct, as specified in the CASA guide[2]. We calculate the visibility weights of the 12m and 7m observations with the `statwt` task. After calculating the correct visibility weights, the 12m array and 7m array data were combined using the `concat` task with a frequency tolerance of 10 MHz (using the `freqtol` parameter). Figure 2.1 shows the 1.3 mm continuum images resulting from the 12m data and 7m data individually, together with the continuum image which results from the combination of both datasets. Figures 2.3a and 2.3b show the CO(2-1) datacubes using 12m and 7m array data separately, whereas Figure 2.3c shows the resulting line cube when combining both datasets.

We image the combined 12m and 7m data and generate a continuum emission image and a CO(2−1) line cube. We describe the imaging process for the continuum map and the procedure to generate the CO(2−1) line cube. We also combine the ALMA CO(2−1) 12m and 7m data with single-dish CO(2−1) observations obtained with the APEX telescope to include the zero spacing emission. The combination of ALMA and APEX data is described in Section 2.1.3.

1.3 mm continuum

We use the standard `clean` task on the 12m and 7m combined data to generate the 1.3 mm (230 GHz) continuum image, removing the spectral channels that contain the CO(2−1) line. We generate the image using both natural weight and Briggs weight. The natural weight lowers the noise and allows point sources to be detected more effectively, but degrades the angular resolution; on the other hand Briggs weighting (also known as robust weighting) provides better resolution and smaller sidelobes of the beam, with a penalty in noise. The Briggs image is generated with a robust parameter $r = 0.5$. The Briggs and natural weighted images resulted in nearly identical rms, 0.18 mJy/beam for Briggs weight and 0.17 mJy/beam for natural weight. We decide to use natural weight for this work, as sensitivity tends to be higher for natural weighted images than Briggs weighted ones.

Figure 2.1 shows the 1.3 mm continuum image done using 12m data only, 7m data only,

[1]http://almascience.eso.org//aq/

[2]https://casaguides.nrao.edu/index.php/DataWeightsAndCombination

and the resulting image from the combined 12m and 7m datasets is shown in Figure 2.2. The continuum image has a field of view (FOV) of 3'×3'.

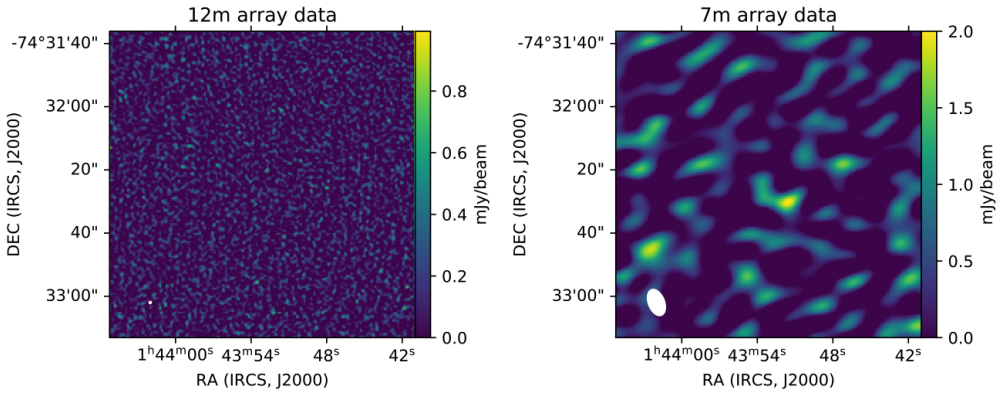

Figure 2.1: ALMA continuum images at 1.3 mm of Magellanic Bridge A, generated using 12m data only (left) and 7m data only (right). All images are done with natural weight. White ellipse in each image represents the beam size.

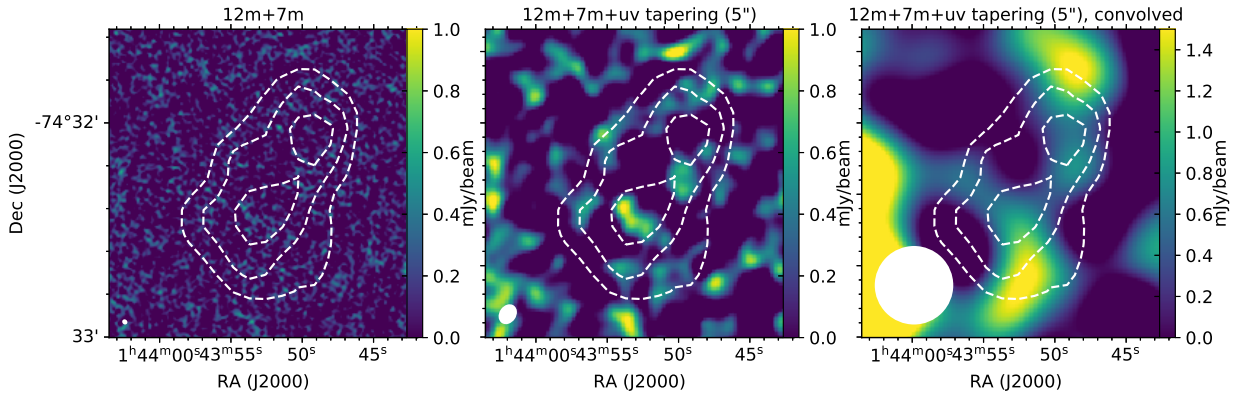

Figure 2.2: ALMA continuum images at 1.3 mm of Magellanic Bridge A, generated using 12m and 7m data, where imaging is performed using natural weight. The left image corresponds to the continuum obtained combining the 12m and 7m array data (from Figure 2.1), without uv tapering. The middle image is the 12m and 7m array continuum with its visibility data tapered using a Gaussian with an on-sky FWHM of 5". The right image is the tapered continuum image convolved to reach a resolution of 22". The white ellipse in the bottom left corner represents the beam size. Dashed contours correspond to continuum emission in the APEX 870 μm map at 25, 30, and 35 mJy/beam.

The 1.3 mm continuum image we use for this work is generated with the 12m and 7m combined dataset, using natural weight and a tapering in the u-v plane. The taper gives more weight to the shorter baselines, which might improve the sensitivity to extended sources but degrades the resolution of the image. We apply a tapering of 5", which results in an image with a resolution of 5.9" × 4.7". To compare with the APEX LABOCA 870 μm image (see Section 2.1.2), we convolved the natural, uv-tapered image to reach a beam FWHM equal to 22". The beam size (described through the FWHM in the major and minor axes $\theta_{\rm major}$ and $\theta_{\rm minor}$) and rms σ of the continuum image, before and after tapering and convolution,

are summarized in Table 2.1. The tapered continuum images (convolved and not convolved to 22") are in Figure 2.2, together with the 1.3 mm continuum image without tapering.

Weight	$\theta_{\rm major}$ (")	$\theta_{\rm minor}$ (")	PA (deg)	σ (mJy/beam)
Natural	1.54	1.37	47.9	0.17
Natural+UVT (5")	5.93	4.71	-34.3	0.35
Natural+UVT (5")*	22.0	22.0	0	1.20
Briggs ($r = 0.5$)	1.26	1.16	44.7	0.18

Table 2.1: Properties of the resulting continuum at 1.3 mm (230 GHz). UVT: uv-tapered images, using the tapering size in parenthesis. *Convolved to reach a beam size of 22".

CO(2-1) line

We perform the `clean` standard routine in the combined 12m and 7m data, using a mask based on the APEX CO(2−1) data described in Section 2.1.2. We use Briggs weighting with a robust parameter of 0.5. We show the CO(2-1) datacubes from the 12m and 7m array data separately, in the channels which show molecular emission, in Figures 2.3a and 2.3b. We show the resulting 12m and 7m combined datacube in the channels which show molecular emission in Figure 2.3c.

The 12m and 7m combined CO(2−1) cube has a FOV of 3'×3', a velocity resolution of 0.5 $\rm km\,s^{-1}$, an angular resolution of 1.22×1.15 (PA=42^o) and variable rms throughout the line cube with values ranging from 22 and 36 mJy/beam per channel.

This ALMA CO(2−1) cube made with the 12m and 7m array combined data is then combined with the CO(2−1) APEX line cube, as described in Section 2.1.3.

2.1.2 APEX observations

We use observations of Magellanic Bridge A performed with the APEX telescope[3], a 12m diameter telescope located in Llano de Chajnantor, Chile. These observations consist of an 870 μm continuum image, which we describe in Section 2.1.2, and a CO(2−1) line emission cube, described in Section 2.1.2.

LABOCA 0.87 mm continuum

We use 870 μm continuum observations of Magellanic Bridge A obtained with the Large APEX Bolometer Camera (LABOCA) on the APEX telescope. LABOCA is an array of bolometers with a central frequency of 345 GHz, a bandwidth of 60 GHz and a total FOV of 11.4' (Siringo et al. 2009).

We use the 870 μm continuum image of Magellanic Bridge A presented in Verdugo (2012). The Magellanic Bridge A data belongs to project C-086.F-0679A-2010 (PI M. Rubio). The

[3]APEX is a collaboration between the Max-Planck-Institut fur Radioastronomie, the European Southern Observatory, and the Onsala Space Observatory.

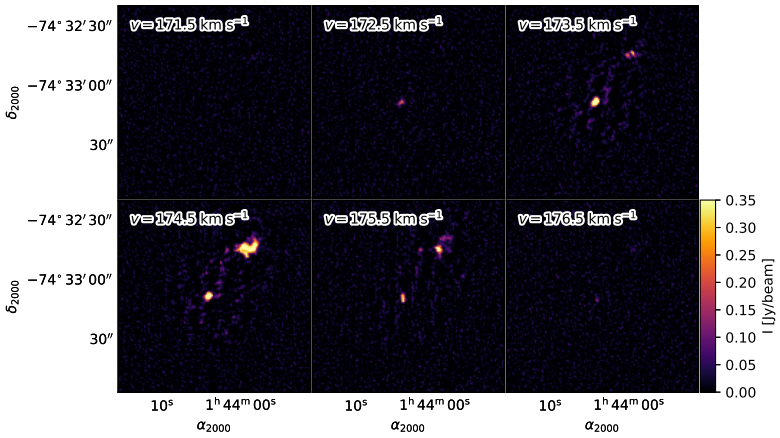

(a) 12m data

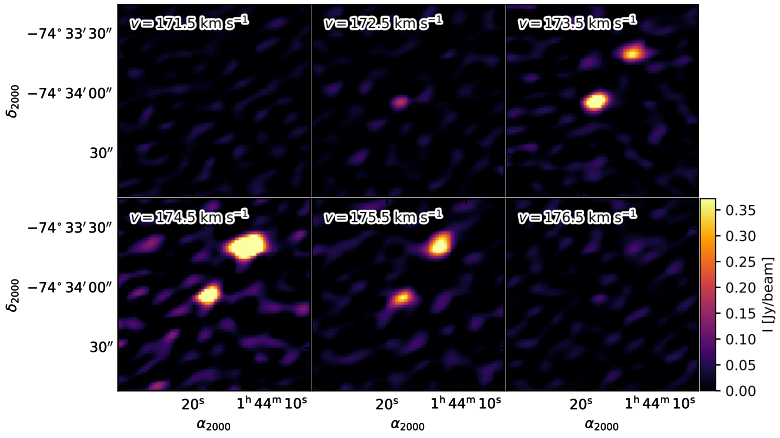

(b) 7m data

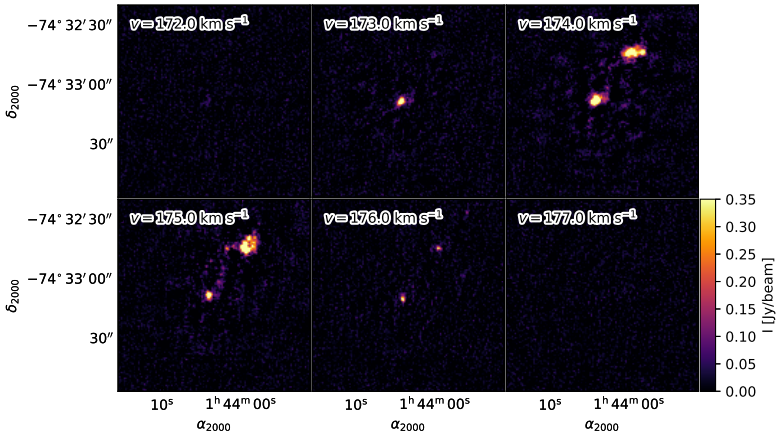

(c) 12m+7m data

Figure 2.3: ALMA CO(2-1) channel maps of Magellanic Bridge A. The velocity range is 171 to 177 km s^{-1}, with 1 km s^{-1} interval between images. (a) Line cube made with 12m data only. (b) Line cube made with 7m data only.(c) Line cube made with the combined 12m array and 7m array datasets.

observations were done in August and October, 2010, with a precipitable water vapour (pwv) content between 0.2 and 0.9 mm. The total integration time of the LABOCA observations was 3.94 hours. The reduction of this continuum image was done with the Bolometric Array Analysis Software (BoA)[4]. The reduction required two calibrations: an opacity (τ) calibration, using the τ values obtained from pwv measurements done with the APEX radiometer, and a flux calibration based on Neptune and Uranus flux observations. The flux calibration has an estimated error of 20%. The final continuum image was generated through an iterative reduction process:

- A first reduction was done with the standard BoA reduction script optimized for weak sources,
- Then, two iterations of the reduction code were done where pixels with S/N over 2.5 were flagged, in order to get rid of extra noise,
- Finally, the reduction code was done 6 times using a mask to detect emission over S/N of 2.5, subtract it, reduce the map without the source and add the source again before the next iteration begins.

The final image is presented in Figure 2.4. It has a beam size of 22.4" (6.4 pc), a FOV of $11.4' \times 11.4'$ and an rms of 5 mJy/beam, which is consistent with the integration time and weather conditions at the time of observation.

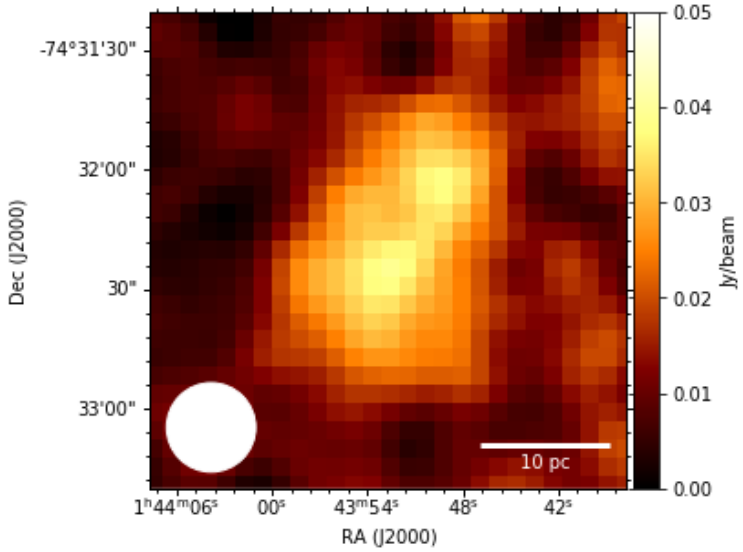

Figure 2.4: APEX-LABOCA continuum image at 870 μm, obtained from Verdugo (2012). The white scalebar represents a 10 pc length. The white circle represents the beam size.

CO(2-1) line

We use CO(2−1) line observations, performed using the On-The-Fly mapping technique with the APEX−1 receiver of the Swedish Heterodyne Facility Instrument (SHeFI) at the APEX telescope. The receiver has a spectral range of 213 − 275 GHz. These observations were

[4]BoA is a data reduction package developed specially to process data acquired with bolometer arrays at APEX telescope. The primary goal is to handle data observed with LABOCA

made in June, 2014, under project C-093.F-9711A-2014 (PI M. Rubio), with pwv between 1.0 and 1.6 mm. The total integration time towards Magellanic Bridge A was 1.28 hours. The mapped area consists of a square of $5.9' \times 5.9'$ covering the central region of the infrarred emission detected by the Herschel telescope (see Fig. 3.1).

We reduce the APEX CO(2−1) line cube through the standard procedure of the CLASS software, Gildas[5]. The antenna temperature T_A^* is delivered by APEX corrected for atmospheric attenuation[6]. We scale T_A^* to the main beam brightness temperature using $T_{mb} = T_A^*/\eta_{mb}$, with a main beam efficiency $\eta_{mb} = 0.72$ for APEX−1 (Vassilev et al. 2008).

The resulting APEX CO(2−1) cube is shown in Figure 2.5, in the same channels as Figures 2.3a, 2.3a and 2.3c. It has a spatial resolution of 28.7", a velocity channel spacing of 0.125 km s^{-1} and an rms of 5.4 Jy/beam (150 mK) per channel. This line cube is combined with the resulting ALMA CO(2−1) line cube and described in Section 2.1.3.

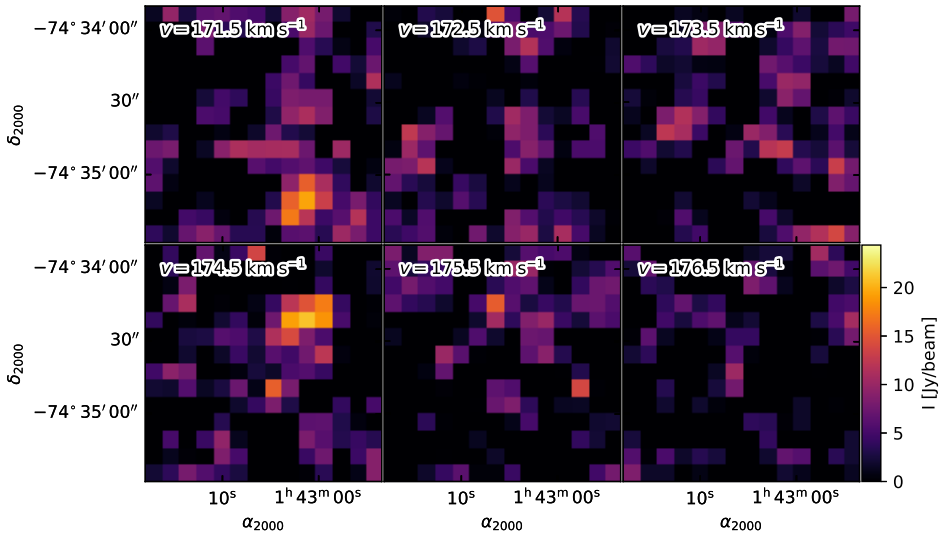

Figure 2.5: APEX CO(2-1) line observations of Magellanic Bridge A. Channel maps are shown in the velocity range 171 to 177 km s^{-1}, with an interval of 1 km s^{-1} per image.

2.1.3 Combined ALMA & APEX CO(2-1) observations

We combine the 12m and 7m ALMA CO(2−1) line cube described in Section 2.1.1, with the single-dish APEX CO(2−1) line cube from Section 2.1.2. To combine the observations, we use the `feather` task from the CASA software, which performs the combination in Fourier space. The final combined CO(2−1) datacube is shown in Figure 2.6, in the same channels as Figures 2.3a, 2.3b, 2.3c and 2.5. It has a FOV of 3'×3', a spatial resolution of 1.22×1.15 (≈ 0.3 pc) and spectral resolution of 0.5 km s^{-1}. This CO(2−1) line cube has a variable rms, with values between 30 and 36 mJy beam^{-1} per channel depending on position.

[5]http://www.iram.fr/IRAMFR/GILDAS/

[6]http://http://www.apex-telescope.org/observing/ (APECS user manual, Revision 4.1 June 5th, 2020)

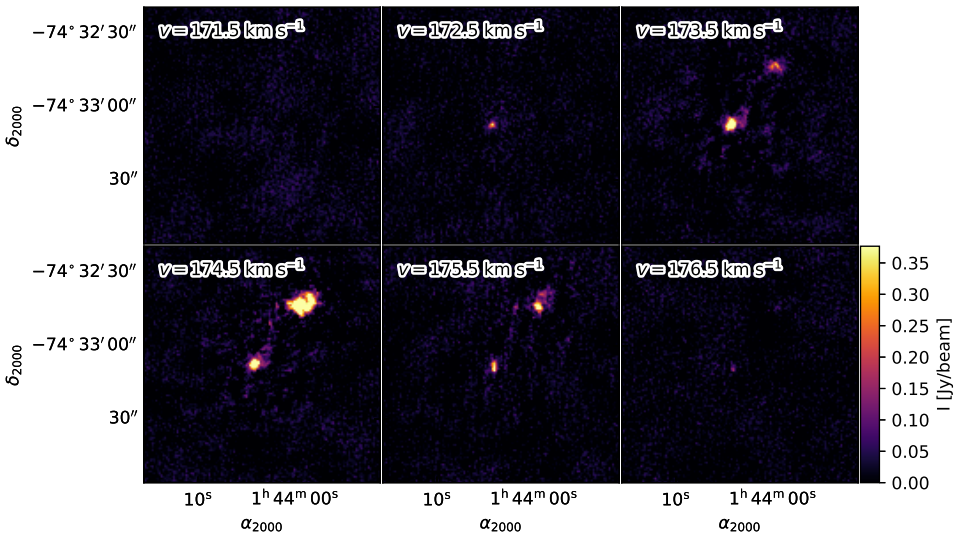

Figure 2.6: Final CO(2-1) line cube of Magellanic Bridge A, which is the combination between the ALMA 12m and 7m array data with the APEX observations of the CO(2-1) line emission. The velocity range is 171 to 177 km s^{-1} with 1 km s^{-1} spacing.

2.1.4 Complementary data

We use Herschel observations from the HERITAGE Herschel key project (Meixner et al. 2013), consisting of maps of the SMC at 100, 160, 250, 350 and 500 μm. We extract a square region of $11' \times 11'$ from these maps, centered at α =1:43:50, δ =-74:32:23 (FK5, J2000), to work with the continuum images centered at Magellanic Bridge A. The angular resolution of the 100, 160, 250, 350 and 500 μm images is 9", 14", 22", 30" and 43" and the rms noise of each image is 9, 6, 0.6, 0.3 and 0.2 MJy/sr, respectively. The flux calibration of these images has an associated uncertainty of 10% and 20% for the 100 and 160 μm images, respectively, and $\sim$8% for the 250, 350 and 500 μm images. We also use the 160 μm Spitzer image, obtained from the Multiband Imaging Photometer for Spitzer (MIPS) for the SAGE-SMC Spitzer Legacy Program (Gordon et al. 2011), and extracted the region containing Magellanic Bridge A in the same way. The Spitzer image has a resolution of 40", an rms of 4 MJy/sr and flux calibration uncertainty of $\sim$10%. All these images were taken from the NASA/IPAC Infrarred Science Archive[7].

We use an Hα image of the SMC from the Southern Hα Sky Survey Atlas (SHASSA) (Gaustad et al. 2001), which contains the Magellanic Bridge. The survey covers 13^o of the southern sky and has a resolution of about $0.8'$. We extract the region containing the Magellanic Bridge A source the same way as with the Hershel images.

[7]https://irsa.ipac.caltech.edu/frontpage/

2.2 Observations and data reduction for 30 Doradus

2.2.1 ALMA observarions

We use Band 7 ALMA observations of 30Dor, performed during Cycle 5 using the 7m ALMA Compact Array (ACA). These observations were done under project 2017.1.00368.S (PI M. Rubio).

The observations have two correlator setups:

1. Setup number 1 is tuned to observe the ^{12}CO(3-2), ^{13}CO(3-2) and CS(7-6) molecular lines and contains one spectral window (spw) to observe continuum emission. Each of the three spws that contain molecular lines have 2048 channels with a channel width of 0.24 MHz (0.21 km s^{-1}), which gives a total bandwidth of 500 MHz (430 km s^{-1}) per spw. The continuum spw has 128 channels with a channel width of 15.62 MHz (13.6 km s^{-1}), giving a total bandwidth of 2 GHz (1735 km s^{-1}).
2. Setup number 2 is tuned to observe the HCO$^+$(4-3) and HCN(4-3) lines and contains two spw to observe continuum emission. The two spw that contain molecular lines have 2048 channels with a channel widrh of 0.49 MHz (0.41 km s^{-1}), which gives a total bandwidth of 1 GHz (841 km s^{-1}) per spw. The two spw that are used to detect continuum emission have 2048 channels with a channel width of 0.98 MHz (0.82 km s^{-1}), which gives a total bandwidth for each spw of 2 GHz (1682 km s^{-1}) per spw.

We decide to re-image the calibrated data instead of working with the data delivered by ALMA. After a visual inspection of the line cubes and the masks delivered, we detected strong negative emission in the spectra, which correspond to the superposition of the negative sidelobes of the antenna response, close to strong line emission. We reduce this effect in our data by doing an interactive CLEAN process, modifying the masks given by ALMA manually.

Molecule	Beam FWHM (")	PA (deg)	Δv_{chan} (km s^{-1})	Pixel size (")	σ (mK)	ν_{rf} (GHz)
^{12}CO(3-2)	4.6 x 4.0	54	0.211	0.7	47	345.796
^{13}CO(3-2)	4.7 x 4.0	79	0.221	0.7	51	330.587
CS(7-6)	4.6 x 4.0	57	0.213	0.7	34	342.883
HCO$^+$(4-3)	4.7 x 3.6	77	0.410	0.7	30	356.734
HCN(4-3)	4.7 x 3.6	76	0.413	0.7	26	354.505

Table 2.2: Characteristics of the resulting line emission cubes. PA is the angle between the x axis and the major axis of the beam, counterclockwise. Δv_{chan} is the change in velocity from one spectral channel to another. ν_{rf} is the rest frequency of the line cube.

We recover the calibrated data using the CASA Pipeline v. 5.4.0.70, using the standard scripts provided by the ALMA Science Archive[8] with the delivered raw data. The phase center of all data is α =05h38m39.95s, δ = -69°05'40'.33 (J2000) and both correlator setups cover a field of view of 1.2'×1.2'. The maximum recoverable scale (MRS) for setup number 1 is 19.1 (4.6 pc at a distance of 50 kpc) and for setup number 2 is 18.6 (4.5 pc at a distance of 50 kpc). The beam size in arcseconds, position angle (PA) in degrees, spectral resolution

[8]http://almascience.eso.org//aq/

Δv_{chan} in km s^{-1}, pixel size in arcseconds, rms σ in mK and rest frequency ν_{rf} in GHz of each line cube are in Table 2.2.

^{12}CO(3-2) line

We produce a line cube for the ^{12}CO(3-2) molecular line emission. Calibrated visibilities are first continuum-subtracted in the uv plane and then deconvolved using the `tclean` task in CASA. The line cube is deconvolved using the Hogbom CLEAN algorithm and Briggs weighting with a robust parameter of 0.5. The resulting ^{12}CO(3-2) line cube is shown in Figure 2.7, between 210 and 285 km s^{-1}. The rest of the line cubes show similar emissions.

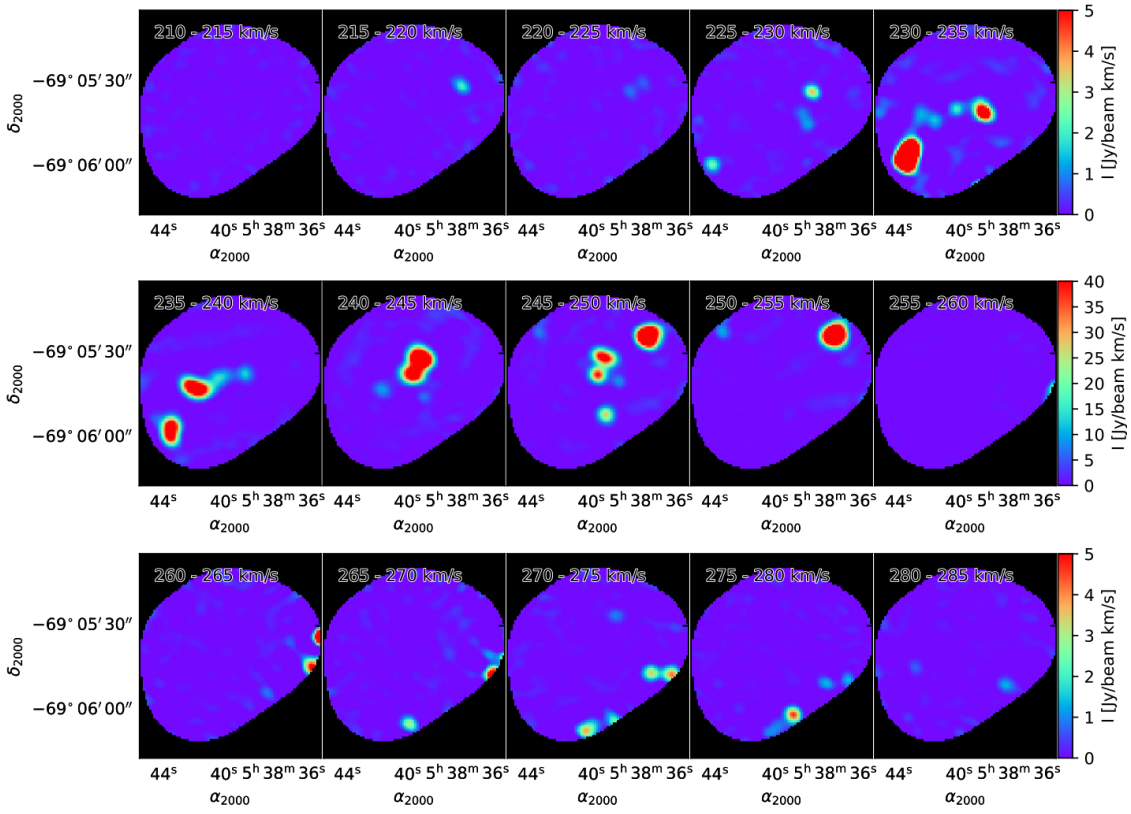

Figure 2.7: Velocity integrated images of the ALMA ^{12}CO(3-2) line cube of 30Dor, every 5 km s^{-1}. Each row has its own intensity range: the first and third row go from 0 to 5 Jy beam^{-1} km s^{-1} and the second row goes from 0 to 40 Jy beam^{-1} km s^{-1}.

880 μm continuum

We produce one continuum image combining the continuum spw from setup number 1 and the two continuum spws from setup number 2. We first concatenate the spws together in one calibrated file using the `concat` routine with a frequency tolerance of 10 MHz. We flag the channels in the first spw from setup number 2 that contain CS(7-6) line emission. This is the only line that falls inside the continuum spw. We flag the channels in the second continuum spw from setup number 2 that present increased amplitude due to the atmospheric transmission, as they add noise to the data. We image the concatenated data using multi-frequency synthesis, implemented in the `tclean` task, with natural weight. We do an

interactive CLEAN to apply a manual mask to the dirty image. The final continuum image is shown in Figure 2.8. It has a central frequency of 338.5 GHz (886 μm), a total bandwidth of 13.5 GHz, a resolution of 4.7 x 3.9, with a position angle of 69 deg, a pixel size of 0.7 and an RMS of 4 mJy/beam.

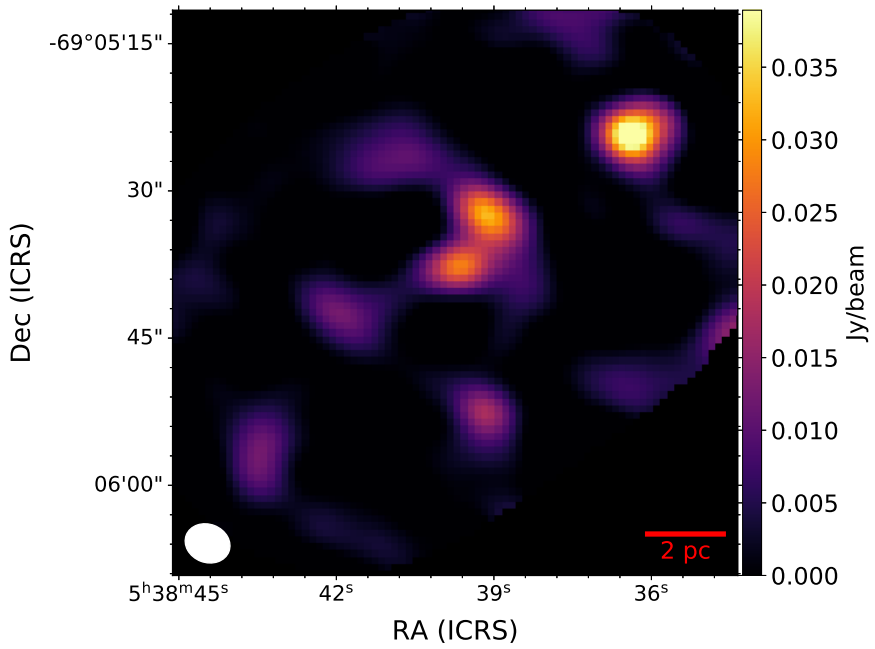

Figure 2.8: ALMA 880 μm continuum image of 30 Doradus in the vicinity of R136. The red scalebar represents a 2 pc length. The white ellipse represents the beam size.

^{13}CO(3-2), CS(7-6), HCO$^+$(4-3) and HCN(4-3) line cubes

We produce line cubes for the ^{13}CO(3-2), CS(7-6), HCO$^+$(4-3) and HCN(4-3) molecular lines. The calibration and imaging is done the same way as for the ^{13}CO(3-2) line cube. The ^{13}CO(3-2), CS(7-6), HCO$^+$(4-3) and HCN(4-3) molecular line cubes show similar emissions as the ones present in the ^{12}CO(3-2) line cube.

All images and line cubes used in this work have primary beam correction applied after deconvolution. For this, we use the primary beam response given by the tclean task after the CLEAN process and divide the line emission image by this response. In the case of the line cubes, each channel was divided by the primary beam response.

2.2.2 Complementary Data

We use a Brγ line emission image obtained with the Cerro Tololo Infrared Imager (CRIM), located on the 1.5 m telescope in Cerro Tololo Inter-American Observatory (CTIO, Guzmán 2010, , M. Rubio priv. comm.). The Brγ line emission is an H_2 recombination line at 2.16 μm, which traces ionized gas content of the ISM. This Brγ line emission image has a resolution of 1.2" and a pixel size of 0.4", with intensity units of erg cm^{-2} s^{-1} sr^{-1}.

We use a radio continuum emission image at 6 cm (4.8 GHz), observed using the Australia Telescope Compact Array (ATCA), part of a survey in the Magellanic Clouds by Dickel et al.

(2005). This image has a resolution of 3.16" $\times$ 2.29" and a pixel size of 2" and intensity units of Jy/beam.

Chapter 3

Molecular clouds in Magellanic Bridge A

In this chapter, we identify the molecular clouds found in gas and dust emission in Magellanic Bridge A and obtain their physical properties using both emissions. These results are published in Valdivia-Mena et al. (2020s, in press).

3.1 Millimeter and submillimeter emission from Magellanic Bridge A

In this section, we study the Magellanic Bridge A dust emission through the millimeter and submillimeter continuum images described in Section 2.1.1, Section 2.1.2 and Section 2.1.4. We first describe the sources present in the 870 μm continuum image. Then, we construct the spectral energy distribution (SED) of Magellanic Bridge A dust using the continuum images and subtracting all contributions that do not come from dust emission (Section 3.1.1). We obtain the dust properties of Magellanic Bridge A by adjusting a Modified Blackbody (MBB) model to the SED (Section 3.1.2). We compare the resulting MBB model with the dust emission derived from the LABOCA 870 μm and ALMA 1.3 mm continuum images (Section 3.1.3). Finally, we use the properties obtained from the model to calculate the total gas mass using dust emission (Section 3.1.4).

We present three different ALMA 1.3mm continuum images using different weights and tapered as explained in Section 2.1.1 and no continuum source is detected in these ALMA continuum images, as seen in Fig. 2.2. There is a hint of emission in the uv-tapered ALMA image convolved to 22", but this emission is not coincident with Magellanic Bridge A in the continuum images from Herschel, Spitzer or LABOCA, so it might be related to antenna noise generating some artifacts. We use the natural weighted, uv-tapered image to obtain an upper limit for the flux density at 1.3 mm (see Section 3.1.1).

We detect continuum emission from Magellanic Bridge A at 870 μm. The APEX continuum image is shown in the bottom right panel of Fig. 3.1. The source is also detected in the Herschel 100, 160, 250, 350 and 500 μm images. We can resolve two peaks with similar

intensities ($\sim$ 40 mJy/beam) and separated by $\sim$ 27" (8 pc), which is near the limit of the APEX resolution. We identify these two sources as North and South throughout this paper. In the Herschel 100 and 160 μm images, the northern peak is not seen, while the southern source can be seen in all images. Unlike the APEX 870 μm continuum, the 350 and 500 μm lower resolution images do not separate well the northern component from the southern one, but it can be seen as an elongated structure. For comparison, we plot the APEX contours over the Herschel continuum images in Fig. 3.1. In the following section, we characterize the dust emission towards Magellanic Bridge A and we also characterize the emission coming from the North and South sources found in the APEX 870 μm image.

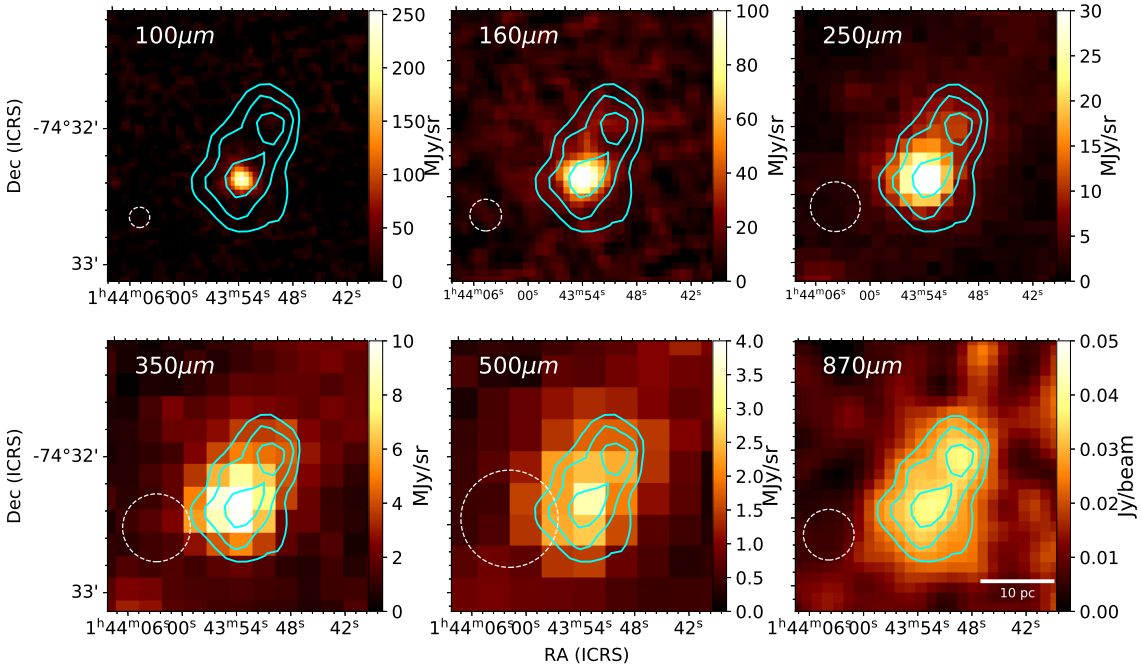

Figure 3.1: Herschel continuum images of Magellanic Bridge A at 100, 160, 250, 350, and 500 μm, together with the LABOCA continuum image at 870 μm. The cyan contours correspond to the LABOCA 870 μm continuum image at 25 (5σ), 30 (6σ), and 35 mJy/beam (7σ). The dashed circles indicate the beam sizes for each image, which correspond to a FWHM of 9" (100 μm), 14" (160 μm), 22" (250 μm), 30" (350 μm), 43" (500 μm) and 22.4" (870 μm). The scale bar in the bottom right panel indicates a 10 pc length.

3.1.1 Spectral energy distribution of Magellanic Bridge A

We build the SED for Magellanic Bridge A using Herschel, Spitzer, APEX and ALMA continuum images. We also build the SED for the North and South sources using Herschel emissions only at 100, 160 and 250 μm, together with the LABOCA and ALMA continuum images. To construct each SED, we perform aperture photometry at each wavelength where emission was detected to obtain the flux densities. Then, we subtract the contributions that are not thermal emission. We determine an upper flux density limit in the ALMA 1.3 mm continuum image, as no emission is detected.

In the following, we describe how we construct the SED and how we determine the contribution from other emission mechanisms.

Flux density measurements

We obtain the flux densities in the Herschel, Spitzer and LABOCA continuum images of Magellanic Bridge A using aperture photometry. We first convolve all images to a common resolution of 43", which corresponds to the resolution of the Herschel 500 μm image, as it has the poorest resolution of all our images. Convolving results in a change in the rms of each image: the new rms are 2.0, 5.0, 0.5 and 0.3 MJy/sr for the Herschel 100, 160, 250 and 350 μm images, respectively. The convolved LABOCA image has an rms of 26 mJy/beam. We measure the total emission coming from Magellanic Bridge A in an aperture with a radius r = 50", centered at α = 1:43:52.68, δ = -74:32:20.23 (FK5, J2000). The position and size of this aperture is shown in Figure 3.2. For all images, we subtract the sky using an annulus centered at the same position as the aperture, with inner radius $r_{in} = 2.5'$ and outer radius $r_{out} = 3.0'$ for Magellanic Bridge A. We do not apply an aperture correction to the photometry results of Magellanic Bridge A because the aperture encloses the source completely and the aperture area is almost 4 times the beam size. The total flux density error is the sum in quadrature of the flux calibration error for the measured flux density and the photometric error ε:

$$\varepsilon = \sqrt{N}\sigma, \tag{3.1}$$

where N is the number of beams inside the aperture and σ is the rms of the image in Jy/beam. The flux densities measured for Magellanic Bridge A are given in the first row of Table 3.1. The 870 μm and 1.3 mm emission have been corrected for free-free emission and CO (2−1) line contribution at the respective wavelength. These corrections are further explained in Section 3.1.1. In the Spitzer 160 μm image (not included in Table 3.1), we measure a flux density $S_{160\mu m} = 1009 \pm 101 \pm 386$, where the first error corresponds to the flux calibration error and the second is the photometric error.

In the case of Magellanic Bridge A North and South, we only use the 100, 160 and 250 μm images from Herschel and the LABOCA 870 μm continuum. We do not use the 350 and 500 μm images because the North and South sources cannot be separated due to the resolution (their beam FWHM are larger than 22"). We convolve the Herschel images to a common resolution of 22" to measure their flux densities. The rms after convolution are 2.2 and 5.5 MJy/sr for the Herschel 100 and 160 μm images, respectively. For the photometry, we use a circular aperture with a common radius r = 11", centered at α = 1:43:49.0, δ = -74:32:00.2 (FK5, J2000) for source North and at α = 1:43:53.8, δ = -74:32:24.5 (FK5, J2000) for source South, which correspond to the peak positions in the LABOCA image. The positions and sizes of these apertures are shown in Figure 3.2. In this case, since the sources are not resolved and the photometry is performed within the FWHM of the spatial beam, we apply an aperture correction factor of 2 in the flux density measurements. The total flux density error is also calculated as the sum in quadrature of the associated flux calibration error and photometric error.

Since there is no emission detected in the ALMA 1.3 mm image, we determine an upper limit for the flux density at 1.3 mm for the source Magellanic Bridge A and sources North and South, based on the ALMA continuum image sensitivity. To do this, we use a value of 3 times the photometric error ε. For Magellanic Bridge A, we obtain a photometric error ε = 5.5 mJy inside an r = 50" circular aperture, which gives a 1.3 mm flux density upper limit for Magellanic Bridge A of 16.5 mJy. The photometric error for the North and South

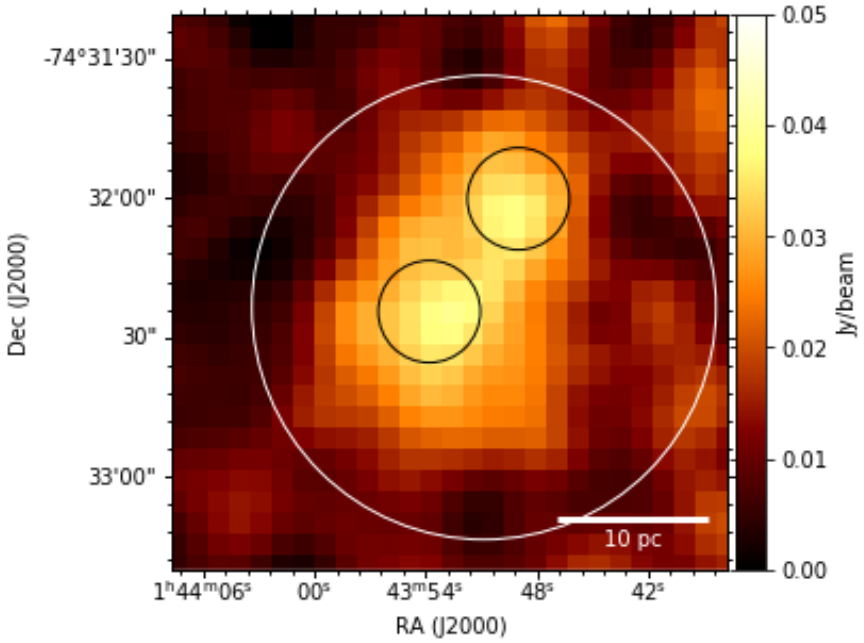

Figure 3.2: APEX-LABOCA continuum image at 870 μm. The white circle shows the position and size of the circular aperture used for the aperture photometry of the Magellanic Bridge A source. The black circles show the position and size of the circular aperture used for the aperture photometry of sources North and South. The scalebar represents a 10 pc length.

sources is $\varepsilon = 2.4$ mJy in a $r = 11$" circular aperture, after applying an aperture correction of a factor of 2. This gives a 1.3 mm flux density upper limit of 7.2 mJy for sources North and South.

The flux densities measured for each source and wavelength, together with the flux density upper limits at 1.3 mm, are summarized in Table 3.1. The 1.3 mm and 870 μm flux densities listed correspond to dust emission only at these wavelengths as free-free emission and CO line contributions have been estimated and subtracted (see Section 3.1.1). Using these flux densities, we build the SED shown in Fig. 3.3.

Free-free and CO(3-2) contribution

The flux density measurement from the APEX 870 μm image contains emission of three different physical processes: 1) thermal dust continuum emission, 2) free-free (bremsstrahlung) emission from ionized gas, and 3) a contribution from molecular lines in the passband (^{12}CO(3-2) in particular, which is the brightest). At 1.3 mm, there is also free-free emission and a molecular line (^{12}CO(2−1)). We are interested in the dust continuum emission; therefore, we need to calculate and remove the other two contributions to the measured flux density. The CO(2−1) line emission is already removed when the ALMA 1.3 mm continuum image is constructed (see Section 2.1.1), so we determine the contribution of free-free to both 870 μm and 1.3 mm continuum emission and the contribution of ^{12}CO(3-2) line emission in the 870 μm continuum image.

Source	R_{ap} (")	$S_{100\mu m}$ (mJy)	$S_{160\mu m}$ (mJy)	$S_{250\mu m}$ (mJy)	$S_{350\mu m}$ (mJy)	$S_{500\mu m}$ (mJy)	$S^{\dagger}_{870\mu m}$ (mJy)	$S^{\ddagger}_{1.3mm}$ (mJy)
MagB. A*	50	$952\pm95\pm151$	$1565\pm313\pm511$	$856\pm68\pm48$	$422\pm34\pm33$	$187\pm15\pm23$	$257\pm52\pm28$	< 16
North**	11	$131\pm13\pm49$	$305\pm61\pm120$	$139\pm11\pm12$			$46\pm9\pm5$	< 7
South**	11	$678\pm68\pm48$	$838\pm168\pm120$	$449\pm36\pm13$			$56\pm11\pm5$	< 7

Table 3.1: Dust emission flux densities in Magellanic Bridge A, North and South. We express the errors on our measurements with the flux calibration error first (Herschel errors obtained from Meixner et al. 2013) and the photometric error last.†Flux density at 870 μm has the free-free emission and CO(3−2) line contributions subtracted. ‡Flux density at 1.3 mm has the free-free emission contribution subtracted. *In Magellanic Bridge A, all images are convolved to a common resolution of 43". **In sources North and South, all images are convolved to a common resolution of 22".

We determine the free-free contribution to continuum emission using Hα emission as described in Section 1.3.2. To obtain the intensity of Hα emission in Magellanic Bridge A, we use the Hα image from SHASSA (Gaustad et al. 2001), which is in decirayleighs (dR). We first transform the map units to rayleighs (R) dividing by 10 and then to erg cm^{-2} s^{-1} sr^{-1} using $1\mathrm{R} = h\nu \times 10^6/(4\pi) = 2.41 \times 10^{-7}$ erg cm^{-2} s^{-1} sr^{-1}, where ν is the frequency corresponding to the Hα line (4.57×10^{14} Hz). The Hα measurements obtained through aperture photometry in the same positions as in section 3.1.1 are $(1.2 \pm 0.2) \times 10^{-13}$ erg cm^{-2} s^{-1} for Magellanic Bridge A, and $(2.3 \pm 0.3) \times 10^{-14}$ erg cm^{-2} s^{-1} and $(2.4 \pm 0.4) \times 10^{-14}$ erg cm^{-2} s^{-1} for the North and South sources, respectively. These values consider an extinction $A_V = 0.140$, obtained for the position of Magellanic Bridge A (Schlafly & Finkbeiner 2011).

To convert the Hα flux density into free-free emission S_ν^{ff}, we use Equation 1.36. We use $T_\mathrm{e} \sim 1.7 \times 10^4$ K, the upper limit for the gas temperature reported in Lehner et al. (2001), and $n(He^+)/n(H^+) \sim 0.08$, which is the value estimated for low-metallicity sources like the Magellanic Clouds (Hunt et al. 2004).

After applying Equation 1.36 using $\nu = 344.8$ GHz (870 μm), we obtain a free-free contribution of 117±22 μJy for Magellanic Bridge A, 22±4 μJy for cloud North, and 23±4 μJy for cloud South. These values represent $\lesssim 0.05\%$ of the total continuum emission. When we use Equation 1.36 with $\nu = 230.8$ GHz (1.3 mm), we obtain a free-free contribution of 122±23 μJy in Magellanic Bridge A, 23±4 μJy in cloud North and 24±4 μJy in cloud South. The values for each source and wavelength are listed in Table 3.2. The flux densites presented in Table 3.1 have these contributions subtracted.

Source	$S^{ff}_{0.87mm}$ (mJy)	$S^{ff}_{1.3mm}$ (mJy)
Magellanic Bridge A*	0.117±0.022	0.122±0.023
North**	0.022±0.004	0.023±0.004
South**	0.023±0.004	0.024±0.004

Table 3.2: Free-free emission for each source at 870 μm and 1.3 mm, obtained through aperture photometry. *Aperture photometry done in a circle with a radius of 50". **Aperture photometry done in a circle with a radius of 11".

We obtain the ^{12}CO(3-2) molecular line contribution to the LABOCA continuum flux density $S_{CO(3-2)}$ in Magellanic Bridge A using Equation 5 of Drabek et al. (2012). We calculate the total flux density present in Magellanic Bridge A from the peak integrated intensity $I_{CO(3-2)}$ using:

$$S_{^{12}CO(3-2)} = \frac{2k\nu^3}{c^3 \Delta\nu_{bol}} \Omega I_{^{12}CO(3-2)} \tag{3.2}$$

where $I_{CO(3-2)}$ is in K km s^{-1}, $\Delta\nu_{bol}$ is the bandpass width in Hz, ν is the frequency of the ^{12}CO(3-2) line in Hz, Ω is the source area in sr and $S_{CO(3-2)}$ is in Jy. We approximate the LABOCA spectral response to a function that is constant over the LABOCA bandpass, so that $g(\nu)_{line} / \int g(\nu) \mathrm{d}\nu = 1/\Delta\nu_{bol}$. We use $I_{^{12}CO(3-2)} = 0.93 \pm 0.07$ K km s^{-1}, the value for the peak $I_{^{12}CO(3-2)}$ in Magellanic Bridge A given in Table 2 of Muller et al. (2014), and its area Ω corresponds to one single ASTE pointing, with $FWHM = 22$". The resultant ^{12}CO(3-2) line contribution to the continuum emission at 870 μm is $S_{CO(3-2)} = 0.85 \pm 0.06$ mJy. This value is subtracted from the total flux density in Magellanic Bridge A at 870 microns, but not from the North and South sources, as there is only one source detected in ^{12}CO(3-2). Nevertheless, the estimated ^{12}CO(3-2) contribution is less than 2% of the 870 μm flux density in sources North and South.

We use the APEX 870 μm flux density measurement with the free-free and ^{12}CO(3-2) line emission contribution subtracted, the ALMA 1.3 mm flux density upper limit with free-free contribution subtracted, and the FIR flux densities obtained from Herschel and Spitzer images to construct the SED of Magellanic Bridge A and the North and South sources. The three SEDs are plotted in Fig. 3.3.

3.1.2 SED modeling

We use the SED constructed in 3.1.1 for Magellanic Bridge A to obtain the dust temperature and dust emissivity index of the region. We also use the SEDs of sources North and South to obtain their dust temperatures. Each SED is modeled assuming that the emission comes from a MBB, which consists of the Planck function multiplied by an emissivity that depends on frequency and dust properties, as described in Section 1.3.1. We derive the physical properties of these dust sources using the parameters of the MBB that best fit each source SED.

We fit the MBB model described by Equation 1.29 for Magellanic Bridge A using the 100, 160, 250, 350, and 500 μm flux densities, obtained from Herschel images in a $r = 50$" radius aperture (see Section 3.1.1). We assume a single dust component and single β dust emissivity index. We have 3 free parameters in the model: C, β and T_{d}. We use χ^2 minimization to determine C, β and T_{d} that best fit the SED, using the function curve_fit of the scipy.optimize package (Virtanen et al. 2020). The MBB that best fits the SED of Magellanic Bridge A gives a dust temperature $T_{\mathrm{d}} = 22.4 \pm 3.4$ K and an emissivity index $\beta = 1.4 \pm 0.5$, listed in Table 3.3. In Fig. 3.3, the solid black line in the left panel represents the best fit MBB for the SED of Magellanic Bridge A.

We fit the MBB model for the North and South sources only using the 100, 160 and 250 μm flux densities, because the 350 and 500 μm beams do not resolve two sources and have poorer resolution than 22" (the 870 μm beam). For these sources, we assume that the dust emissivity

is the same as that found for Magellanic Bridge A, and we therefore fix $\beta = 1.4$ for both sources. We note that assuming a β value for these sources influences the dust temperature obtained, as there is an inverse correlation between β and $T_{\rm d}$ (Shetty et al. 2009). We find the parameters C and $T_{\rm d}$ that best fit the SEDs with χ^2 minimization. The temperature obtained for source South is $T_{\rm d} = 24.5.4 \pm 2.2$ K and source North $T_{\rm d} = 21.7.4 \pm 1.1$ K; these parameters are listed in Table 3.3, and the best fit curves are plotted in In Fig. 3.3 (black line). The best fit results indicate that the North source is colder than the South source by ~ 3 K.

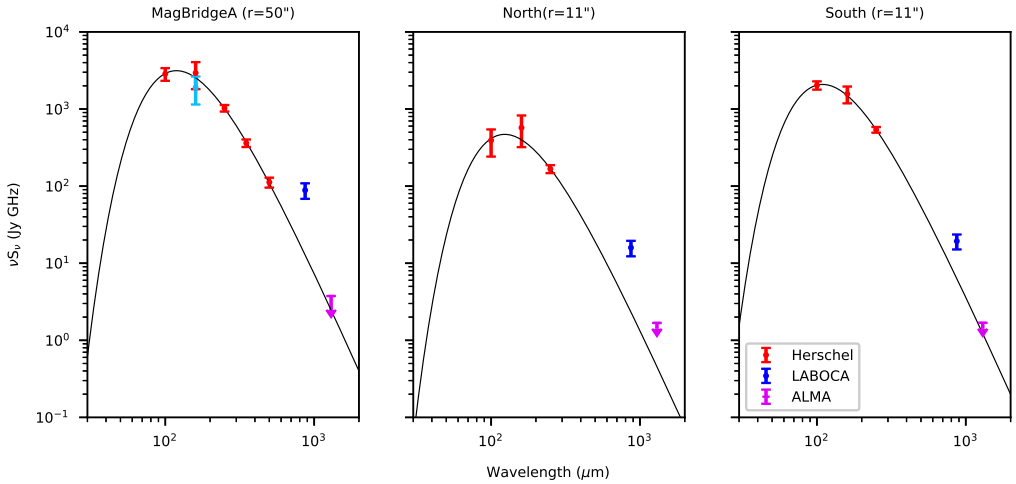

Figure 3.3: SEDs for Magellanic Bridge A and the North and South sources. The points correspond to the energy νS_ν derived from the measured flux density S_λ, obtained using aperture photometry. Red points correspond to νS_ν obtained using Herschel data. Dark blue points correspond to the energy νS_ν obtained using the LABOCA image. The purple arrow corresponds to the νS_ν upper limit at 1.3 mm using the ALMA continuum image. The left panel shows the Magellanic Bride A SED, for which we used the 100, 160, 250, 350 and 500 μm Herschel continuum images, the 160 μm Spitzer continuum image, the 870 μm (LABOCA) and 1.3 mm (ALMA) continuum images with a common resolution of 43". We measure the flux density from Magellanic Bridge A inside a circular aperture of radius $r = 50$". The North and South sources SEDs are shown in the last two panels, constructed with the Hershel 100, 160 and 250 μm continuum images, the 870 μm (LABOCA) and 1.3 mm (ALMA) continuum images at a common resolution of 22". We measure the fluxes from sources North and South in a circular aperture of radius $r = 11$". The MBB model that best fits the Herschel points for each source is shown as a black curve. The parameters of each curve are in Table 3.3.

3.1.3 Submillimeter excess

We define the submillimeter and millimeter excesses $E(\lambda)$ as the ratio of the measured flux density to the predicted flux density from the SED model at $\lambda = 870$ μm and 1.3 mm. We calculate these excesses for each source and summarize our results in Table 3.4.

The submillimeter excess found at 870 μm for Magellanic Bridge A is $E(870\,\mu m) = 6.9 \pm 1.6$ inside an circular aperture with $r = 50$". When we separate Magellanic Bridge A into the

Source	C (sr $Hz^{-\beta}$)	β	$T_{\rm d}$ (K)	χ^2	M_{gas} (10^3 $M_\odot$)‡
MagBridgeA*	$(1.9 \pm 23.4) \times 10^{-29}$	1.4 ± 0.5	22.4 ± 3.4	0.27	6.8 ± 1.5
North**	$(9.0 \pm 3.1) \times 10^{-30}$	1.4†	21.7 ± 2.2	0.5	1.3 ± 0.5
South**	$(2.1 \pm 0.4) \times 10^{-29}$	1.4†	24.5 ± 1.1	0.04	2.9 ± 0.5

Table 3.3: Gas masses and best fit MBB parameters to the cloud SEDs. *Flux densities measured using aperture photometry radius of 50". **Flux densities measured using aperture photometry radius of 11". † β values obtained for Magellanic Bridge A MBB fit. ‡Gas masses derived from the MBB models that best fit the FIR SEDs of each source.

Source	E(870)	E(1.3mm)
MagBridgeA	6.9±1.6	< 1.5
North	6.7±1.6	< 3.7
South	3.0±0.7	< 1.4

Table 3.4: Submillimeter and millimeter excesses for Magellanic Bridge A and sources North and South. Excess is defined as the ratio between the observed flux density and the flux density predicted by the best fit MBB model to the FIR dust flux densities in the SED.

North and South source, this submillimeter excess is also present. For the North source, $E(870\,\mu m) = 6.7 \pm 1.6$, while in the South is $E(870\,\mu m) = 3.0 \pm 1.4$, both considering a photometry aperture radius $r = 11$". Excess emission at 870 μm has been detected in other low-metallicity galaxies using LABOCA (Galametz et al. 2009, 2014; Hermelo et al. 2016) and SCUBA observations (Galliano et al. 2003, 2005; Bendo et al. 2006).

Since we do not detect our sources in the 1.3 mm ALMA continuum, we calculate how much higher the flux density upper limits calculated in Section 3.1.1 are than the predicted flux densities at 1.3 mm. We derive an expected flux density using the MBB model that best fits the FIR SED (see Table 3.3). We obtain an expected flux density of 10.7 mJy for Magellanic Bridge A in an aperture radius $r = 50$", and 2.0 mJy for the North source and 5.3 mJy for the South source within an aperture of radius $r = 11$". The flux density upper limit at 1.3 mm is 16.5 mJy, which is 1.5 times higher than the expected flux density using the MBB model fitted to the FIR flux densities for Magellanic Bridge A. For the individual North and South sources, the upper limits from the ALMA continuum image at 1.3 mm are 7.2 mJy (3.6 times higher than the expected flux density for source North) and 2.2 mJy (1.4 times higher for source South). These values are reported as $E(1.3\,mm)$ in Table 3.4. In summary, our ALMA 1.3 mm data are compatible, within the detection limit, with the MBB fit to the FIR observations, and show no excess at this wavelength. If the excess at 1.3 mm were similar to that at 870 μm, we would have detected the source.

The fact that we do not observe emission at 1.3 mm when there is notable excess emission at 870 μm in our sources is puzzling. The calibration of the LABOCA data was verified as correct by members of our team and the instrument support team, who performed independent reductions of the data that resulted in very similar images. In addition, we note that the morphology of the source at 870 μm in Fig. 3.1 is consistent with emission at 250 to 500 μm continuum images, and the noise of the map is consistent with that expected for the inte-

gration time. In fact, we would have only detected the South source at $\sim 3\sigma$ in the complex if there were no excess. Therefore, we have every expectation that the 870 μm excess is real. If this is so, there are two possibilities to explain the lack of a 1.3 mm detection: either the anomalous emission at 870 μm is present only at that wavelength, or the dust emission is too extended and resolved out in the ALMA 1.3 mm observation. We note that it is very difficult to explain the 870 μm as resulting from an additional very cold dust component, as the lack of an excess at 500 μm would require it to have a dust temperature $T_{\rm d} \sim 3$ K. Through the inclusion of the Morita Array our ALMA observations have a maximum recoverable scale (MRS) of 30.9", although our sensitivity substantially degrades close to that limit. We would expect to see continuum sources similar in size to the CO emitting clouds in this region (Fig. 3.4) if their 1.3 mm flux density had an excess over the MBB fit similar to that measured at 870 μm. If the sources were larger than the 22" used for the photometry, however, they would be at least partially resolved out and undetectable. Clearly future ALMA observations determining the sizes of the sources at 870 μm or deeper observations at 1.3 mm would be extremely useful to establish the nature of the excess.

3.1.4 Gas masses obtained from dust emission

We calculate the total gas masses associated to the 870 μm dust emission for Magellanic Bridge A predicted by the MBB model that best fits the FIR flux densities. For this, we use Equation 1.16, where S_ν is the predicted flux density at frequency ν by the MBB model that best fits the FIR data in Jy. We use a distance $D = 1.85 \times 10^{23}$ cm (the estimated distance to the SMC, 60 kpc, Harries et al. 2003). $B_\nu(T_{\rm d})$ is the spectral radiance at a dust temperature $T_{\rm d}$ in Jy sr^{-1}.

We use the $\varepsilon_{\rm d}(345GHz)$ value presented in Bot et al. (2010a), $\varepsilon_{\rm d}(345GHz) = (3.94 \pm 0.05) \times 10^{-27}$ cm^2, which assumes an absorption coefficient $\kappa_{345GHz} = 1.26 \pm 0.02$ cm^2 g^{-1} and a dust-to-gas ratio that is 1/6 of the ratio in the solar neighborhood. This dust-to-gas ratio is similar to the ratios derived in Magellanic Bridge B and C (Gordon et al. 2009).

For Magellanic Bridge A source, North source and South source, we use the dust temperatures $T_{\rm d} = 22.4 \pm 3.4$ K, $T_{\rm d} = 21.7 \pm 2.2$K and $T_{\rm d} = 24.5 \pm 1.1$ K, respectively, obtained from the best fit MBB to the Magellanic Bridge A SED with $\beta = 1.4$, as derived in Section 3.1.2.

The total gas mass are calculated using the 870 μm flux density predicted from the MBB fit. For Magellanic Bridge A, the gas mass is $(6.8 \pm 1.5) \times 10^3$ M$_\odot$ and for the two separate clouds, North and South, their gas masses are $(1.3 \pm 0.5) \times 10^3$ M$_\odot$ and $(2.9 \pm 0.5) \times 10^3$ M$_\odot$, respectively. There is a difference between the sum of the gas masses of sources North and South and the gas mass of Magellanic Bridge A because dust measurements for the North and South sources are obtained in an aperture of radius $r = 11$", which only includes the peak emission of each cloud, while Magellanic Bridge A is measured inside an aperture of radius $r = 50$", which captures the complete emission from the source. We also estimated the gas masses using an absorption coefficient determined for dust emission at 160 μm by Gordon et al. (2014), $\kappa_{160\mu m} = 9.6 \pm 2.5$ cm^2 g^{-1} as the gas masses are dependant on the chosen $\varepsilon_{\rm d}(\nu)$, which depends on the calibration of κ_ν. Using $\kappa_{160\mu m}$ and the same gas-to-dust ratio 1/6, we obtain a gas mass for Magellanic Bridge of $(9.6 \pm 4.4) \times 10^3$ M$_\odot$, while for source

North is $(1.7 \pm 0.8) \times 10^3$ $M_\odot$ and for source South is $(3.9 \pm 1.4) \times 10^3$ $M_\odot$. These values are within the uncertainties of those obtained using the Bot et al. (2010a) value. For the rest of this work, we use the total gas masses derived from the Bot et al. calibration, listed in the last column of Table 3.3.

3.2 Resolved CO(2-1) molecular clouds

In this section, we study the CO(2−1) molecular line emission in Magellanic Bridge A. We produce the velocity integrated intensity image between 172 and 176 km s^{-1} of the ALMA and APEX CO(2-1) line cube (see Fig. 3.4). We measure an rms of 48 mJy beam^{-1} km s^{-1} in this image, a value which is consistent with the calculated values of 42 and 50 mJy beam^{-1} km s^{-1} using the rms range of the velocity interval (see Section 2.1.3). We resolve two parsec-sized CO(2−1) clouds, which are located towards the North and South 870 μm continuum sources. We extract the spectra of each of these molecular clouds in Section 3.2.1 and determine the physical properties of the molecular clouds in this region in Section 3.2.2.

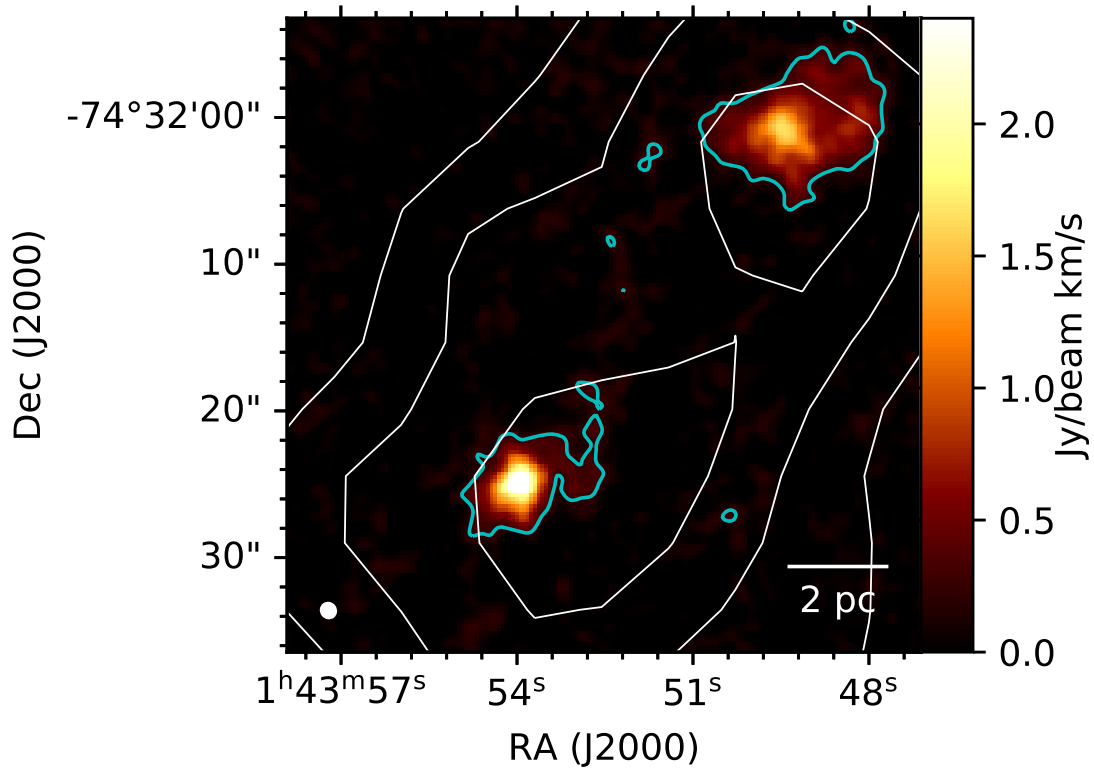

Figure 3.4: Velocity integrated intensity image of the combined ALMA and APEX CO(2−1) cube of Magellanic Bridge A, integrated between 172 and 176.0 km s^{-1}. The cyan contours correspond to 5 times the σ of the integrated image ($\sigma = 48$ mJy/beam km s^{-1}). The white contours correspond to the LABOCA 870 μm continuum image at 25, 30 and 35 mJy/beam, as in Figure 3.1. The white ellipse in the lower left corner represents the beam FWHM (1.22" × 1.15"). The scale bar on the lower right corner indicates a 2 pc length.

3.2.1 CO(2-1) molecular clouds spectra

We identify the molecular clouds in the ALMA and APEX CO(2−1) line cube and extract their spectra. We first identify potential sources in the velocity integrated intensity image as all emission greater than 3σ, being σ the rms of the integrated image. We define the area of each source as the number of pixels inside the 3σ contour. Then we measure the second moments of emission along the major and minor axes of each source in the CO(2−1) integrated emission image. We only keep those sources whose minor second moment is larger than the beam size. The only sources that meet this criterion (survive this decimation) are the two brightest CO(2−1) sources seen in Figure 3.4, which we call CO clouds from now on. These CO clouds spatially coincide with the dust sources characterized in Section 3.1, as seen in Figure 3.4. The peak $I_{CO(2-1)}$ of these clumps in the CO(2−1) integrated image are 1.67±0.05 Jy beam^{-1} km s^{-1} in the North CO cloud and 2.81±0.05 Jy beam^{-1} km s^{-1} in the South CO cloud.

CO Source	RA (J2000)	DEC (J2000)	A (pc^2)	Peak $I^{(a)}_{CO(2-1)}$ (Jy beam^{-1} km s^{-1})	v_{LSR} $^{(b)}$ (km s^{-1})	Δv (FWHM) $^{(b)}$ (km s^{-1})	$S_{CO(2-1)}\Delta v$ $^{(b)}$ (Jy km s^{-1})
North	1:43:49.2	-74:32:00.6	8.1	1.67±0.05	174.6±0.6	1.33±0.03	30.67±2.86
South	1:43:53.8	-74:32:24.7	5.8	2.81±0.05	174.0±0.9	1.93±0.05	21.65±2.05

Table 3.5: Characteristics of the clouds identified in the CO(2−1) line cube. ^{a}Peak values obtained from the CO(2−1) integrated line image between 172 and 176 km s^{-1}. ^{b}Values obtained from the Gaussian fit to the integrated spectra over the cloud area.

We obtain the integrated velocity spectra of each source, adding all spectra in the source area. The resulting spectra for CO sources North and South are shown in Figure 3.5. They have an rms noise of $\sigma = 0.30$ Jy km s^{-1} for CO cloud North and $\sigma = 0.25$ Jy km s^{-1} for CO cloud South, in a velocity channel width 0.5 km s^{-1}. We fit a Gaussian profile to the velocity integrated spectra of clouds North and South to obtain the central velocity v_{LSR} in km s^{-1}, velocity dispersion σ_v in km s^{-1} and integrated flux density $S_{CO(2-1)}\Delta v$ in Jy km s^{-1}. We adjust the Gaussian model to the spectra through least-squares fitting. The Gaussians that best fit each spectra are shown in red in Figure 3.5. We correct σ_v for broadening due to the finite spectral resolution, using Equation 10 of Rosolowsky & Leroy (2006) to obtain the deconvolved velocity dispersion:

$$\sigma_{v,\mathrm{dc}} = \sqrt{\sigma_v^2 - \frac{\Delta V_{chan}^2}{2\pi}}, \tag{3.3}$$

ΔV_{chan} is the velocity difference between two consecutive channels. We report the velocity FWHM Δv calculated from $\sigma_{v,\mathrm{dc}}$. We do not extrapolate σ_v to correct for a sensitivity bias (as suggested in Rosolowsky & Leroy 2006) as the peak emission of the CO clouds North and South is detected with a S/N of 33 and 56, respectively.

The CO cloud North is centered at a velocity of 174.6 ± 0.6 km s^{-1} with a velocity FWHM of 1.33±0.03 km s^{-1}, and the CO cloud South is centered at 174.0±0.9 km s^{-1} with a FWHM of 1.93 ± 0.05 km s^{-1}. The clouds are centered at similar velocities and have similar velocity linewidths. The CO North cloud shows a peak $I_{CO(2-1)}$ emission of 1.67 ± 0.05 Jy beam^{-1} km s^{-1} and cloud South has a peak $I_{CO(2-1)}$ emission of 2.81 ± 0.05 Jy beam^{-1} km s^{-1}. However, as CO cloud North covers an area of 8.1 pc^2 while CO cloud South covers 5.8 pc^2,

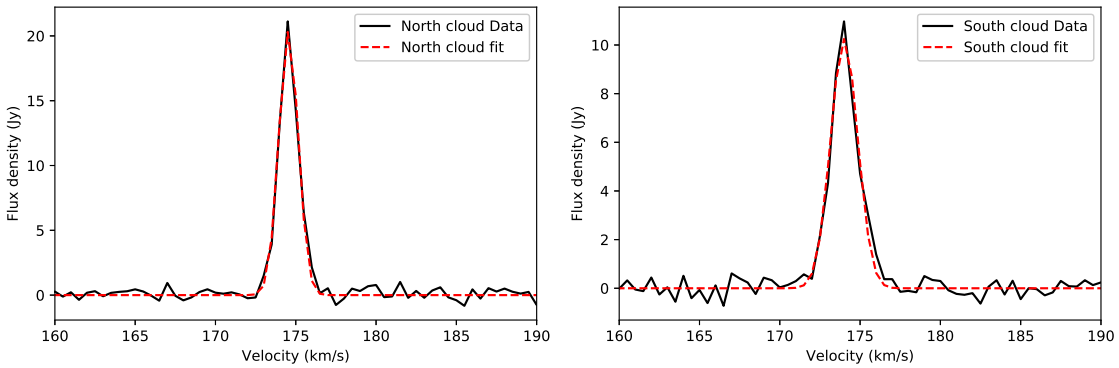

(a) (b)

Figure 3.5: CO(2-1) integrated spectra for Magellanic Bridge A clouds North and South. The black lines correspond to the flux density measured in each channel. The red dashed lines represent the Gaussian fits of the spectra. (a) Spectra for CO cloud North. (b) Spectra for CO cloud South.

the North cloud has a larger emission than the South, with a total flux density $S_{CO(2-1)}\Delta v$ of 30.67 ± 2.86 Jy km s^{-1} and 21.65 ± 2.05 Jy km s^{-1}, respectively.

The results of these fits are summarized in Table 3.5.

3.2.2 Physical properties

We derive the sizes, CO(2−1) luminosities, and virial masses for the CO(2−1) clouds we find in Magellanic Bridge A using the parameters obtained from the integrated spectra for each cloud.

We calculate the radius using Equation 1.2, where σ_{maj} and σ_{min} are the spatial second moments of emission inside the area defined in Section 3.2.1 in radians. We correct σ_r for the spatial broadening ("deconvolve" the radius) due to the beam using:

$$\sigma_r = \sqrt{(\sigma_{maj}^2 - \sigma_{beam}^2)^{\frac{1}{2}}(\sigma_{min}^2 - \sigma_{beam}^2)^{\frac{1}{2}}}, \tag{3.4}$$

where σ_{beam} is the geometric mean of the major and minor axes of the beam in radians: $\sigma_{beam} = \sqrt{\sigma_{maj,beam}\sigma_{min,beam}}$. We do not extrapolate the radius σ_r as we do not expect a significant change in the size σ_r, for the same reason as we did not do it for σ_v: both CO sources are detected with high S/N values as can be seen in Fig. 3.4. We multiply the obtained R by the distance to the cloud D = 60kpc (Harries et al. 2003) to obtain the radii in pc. The radius obtained for the CO clouds are 1.29 ± 0.07 pc for cloud North and 1.04 ± 0.04 pc for cloud South.

We calculate the CO(2−1) luminosities in K km s^{-1} pc^2 using Equation 1.6, replacing $\nu = 230.5$ GHz. This results in:

$$L_{CO(2-1)} = 611.5 S_{CO(2-1)}\Delta v D^2 \tag{3.5}$$

where $S_{CO(2-1)}\Delta$v is the CO(2−1) integrated flux density in Jy km s^{-1}, obtained from the ALMA and APEX combined CO(2−1) line cube, and D is the distance to the Magellanic

Bridge in Mpc. The resulting luminosities are $L_{CO(2-1)} = 67.5 \pm 6.3$ K km s^{-1} pc^2 for CO cloud North, and $L_{CO(2-1)} = 47.7 \pm 4.5$ K km s^{-1} pc^2 for CO cloud South.

We compare the Magellanic Bridge A total luminosity as measured by the single-dish APEX CO(2−1) observations and by the ALMA CO(2−1) observations, to determine any missing diffuse emission. The total luminosity detected by APEX, measured inside a a 58" × 58" box centered at α =1:43:51.3, $\delta = -74$:32:09.2, is 134 ± 9 K km s^{-1} pc^2. The luminosity of clouds North and South in the ALMA CO(2−1) line cube is 66.7 ± 6.0 K km s^{-1} pc^2 and 48.4 ± 4.2 K km s^{-1} pc^2, respectively. If we add the CO luminosities of the two clouds, we obtain a total luminosity for Magellanic Bridge A of 115 ± 10 K km s^{-1} pc^2. Thus, ALMA recovers, within the uncertainties, almost all the luminosity measured in the APEX CO(2-1) line cube, implying that most of the emission in Magellanic Bridge A is concentrated in the two CO(2−1) clouds we characterize in this work.

We determine the virial masses M_{vir} of the clouds using Equation 1.13. We use the deconvolved radii in Table 3.6 and the FWHM in Table 3.5. The virial mass for CO source North is 437.3 ± 26.1 M$_\odot$ and for source South it is 732.9 ± 37.0 M$_\odot$. Even though these clouds are parsec-sized, they contain $\sim 5 \times 10^2$ M$_\odot$, similar to the masses of the most massive molecular clumps in the Milky Way, which have typical radii of ~ 1 pc (see Bergin & Tafalla 2007, and references within).

We estimate the CO-to-H_2 conversion factor $\alpha_{CO} = M_{vir}/L_{CO}$ and the corresponding X_{CO}, which is usually derived for the ^{12}CO(1-0) emission. We do not attempt to correct for variations in the $J = 2-1$ to $J = 1-0$ ratio r_{21}, and simply assume $r_{21} \sim 1$ for the purposes of comparison, which is also a common result for SMC observations (e.g., Lequeux et al. 1994; Rubio et al. 1996a). For CO cloud North, the derived conversion factor is $\alpha_{CO} = 6.5 \pm 0.7$ M$_\odot$ (K kms^{-1} pc^2)$^{-1}$ ($X_{CO} = (3.0 \pm 0.3) \times 10^{20}$ cm^{-2} (K km s^{-1})$^{-1}$) and for cloud South, $\alpha_{CO} = 15.3 \pm 1.6$ M$_\odot$ (K km s^{-1} pc^2)$^{-1}$ ($X_{CO} = (7.1 \pm 0.7) \times 10^{20}$ cm^{-2} (K km s^{-1})$^{-1}$). These values are 1.5 and 3.6 times the canonical value for the Milky Way $\alpha_{CO}(MW) = 4.3$ M$_\odot$ (K km s^{-1} pc^2)$^{-1}$ ($X_{CO} = 2 \times 10^{20}$ cm^{-2} (K km/s)$^{-1}$).

The derived properties R, M_{vir}, $L_{CO(2-1)}$ and α_{CO} are summarized in Table 3.6.

CO Source	R^* (pc)	M_{vir} ($M_\odot$)	$L_{CO(2-1)}$ (K km s^{-1} pc^2)	α_{CO}^{**} ($M_\odot$ (K km s^{-1} pc^2) $^{-1}$)
North	1.29±0.07	437.3±26.1	67.5±6.3	6.5±0.7
South	1.04±0.04	732.9±37.0	47.7±4.5	15.3±1.6

Table 3.6: Physical properties of the emission found in the $^{12}CO(2-1)$ line cube. *Corrected for spatial broadening. **Assumes a CO(2−1) to CO(1−0) ratio $r_{21} \sim 1$.

3.3 Discussion

In this section, we discuss our results and compare them to previous observations of Magellanic Bridge A, other low-metallicity galaxies and the Milky Way.

3.3.1 CO(2-1) in comparison with previous studies

The molecular clouds we find in CO(2−1) emission have spectral properties and masses similar to those inferred from previous unresolved CO measurements in Magellanic Bridge A. The central velocities of CO sources North and South, 174.6 ± 0.6 and 174.0 ± 0.9 km s^{-1}, respectively, are close to the 174.7 km s^{-1} reported for Magellanic Bridge A by Mizuno et al. (2006) through ^{12}CO(1-0) emission with NANTEN (beam $FWHM = 2.6'$). The linewidths of the CO clouds, 1.33 ± 0.03 km s^{-1} for cloud North and 1.93 ± 0.05 km s^{-1} for cloud South, are consistent with the ^{12}CO(1-0) velocity FWHM of 1.6 km s^{-1} reported for Magellanic Bridge A in Mizuno et al. (2006) and with the ^{12}CO(3-2) FWHM of 1.4 km s^{-1}, reported in Muller et al. (2014) observed with ASTE Telescope ($FWHM = 22$"). We find that the sum of the virial masses of the CO clouds North and South, $(1.17 \pm 0.06) \times 10^3$ M$_\odot$, is in agreement with the mass estimated for Magellanic Bridge A by Mizuno et al. (2006), 10^3 M$_\odot$, using $I_{CO(1-0)}$ and a conversion factor of $X_{CO} = 1.4 \times 10^{21}$ cm^{-2} (K km s^{-1})$^{-1}$.

Comparing the CO luminosities found by previous studies of this source is not easy, as they measure different rotational transitions with different resolutions and sensitivities. Nevertheless, by comparing the luminosities over matched areas, together with the similarities in velocity FWHM and virial mass, we estimate that the emission detected in previous observations is mainly associated with the two clouds we observe in this work. The ^{12}CO(1-0) luminosity in the NANTEN detection of Magellanic Bridge A is $L_{CO(1-0)} = 70 \pm 8$ K km s^{-1} pc^2 (Mizuno et al. 2006). The ^{12}CO(3-2) luminosity in the ASTE detection is $L_{CO(3-2)} = 64 \pm 8$ K km s^{-1} pc^2 (Muller et al. 2014). The total CO(2−1) luminosity we measure from both Magellanic Bridge A clouds is $L_{CO(2-1)} = 115 \pm 11$ K km s^{-1} pc^2. The resulting ^{12}CO (3−2)/(2−1) luminosity ratio is $r_{32} = 0.56 \pm 0.09$, which is reasonable for a star-forming cloud. The ^{12}CO (2−1)/(1−0) ratio is $r_{21} = 1.64 \pm 0.24$, which is unusually high with respect to typical values observed in the Milky Way, the Magellanic Clouds, and other galaxies where $r_{21} \sim 1.1 - 0.7$ (e.g., Rubio et al. 1996b; Sorai et al. 2001; Bolatto et al. 2003; Nikolić et al. 2007). Although in localized regions higher ratios can be observed, caused by effective optical depth (Bolatto et al. 2003), it is also possible that the NANTEN ^{12}CO(1-0) luminosity is underestimated. Because of the similarities in velocity, FWHM, and luminosity, it seems that most (if not all) of the CO emission from Magellanic Bridge A detected in previous studies comes from the two compact clouds presented in this work.

The CO emission from the North and South clouds show interesting differences from parsec-sized CO sources present in the Milky Way. Their virial masses are one order of magnitude higher, implying higher densities in the gas. At radii between 1 and 2 pc, clouds in the Milky Way have masses between a few 10 M$_\odot$ to a few 100 M$_\odot$ (Miville-Deschênes et al. 2017), while the clouds found in Magellanic Bridge A have 400 M$_\odot$ and 700 M$_\odot$ for North and South, respectively. We note, however, that most of the clouds in the Miville-Deschênes et al. (2017) catalog have large virial parameters, and as a consequence are not self-gravitating and are unlikely to be forming stars. The assumption of virial, or self-gravitating equilibrium in the Magellanic Bridge A clouds may not be strictly correct, but it is not unreasonable for star-forming clouds. Clouds that have an excess of kinetic energy with respect to their potential energy will be short-lived and very unlikely to locally collapse to form stars. If the CO-emitting cloud is embedded in a large envelope, part of the velocity dispersion may be associated with the external confining pressure associated with the weight of the envelope. In

that case the virial mass estimate effectively includes part of the mass of the envelope. Using the virial mass estimate, the CO clouds North and South have surface densities $\Sigma_{mol} \approx 80$ and 230 $M_\odot\,pc^{-2}$ respectively, and corresponding bulk densities $n(H_2) \sim 700$ and 2600 cm^{-3} assuming spherical geometry. The surface densities of Magellanic Bridge A clouds are similar to typical Σ_{mol} for star-forming clouds in the Milky Way disk (e.g., Heiderman et al. 2010; Evans et al. 2014), but their bulk volume densities are higher than commonly found bulk densities in our Galaxy, which is a reflection of the small size of the clouds in this work. Roman-Duval et al. (2010) find $\Sigma_{mol} \sim 144$ $M_\odot\,pc^{-2}$ and $n(H_2) \sim 230$ cm^{-3} as an average for Milky Way clouds in the Galactic Ring Survey, which tend to be star-forming clouds. The Magellanic Bridge clouds have volume densities that are similar to the densities of clumps in local, star-forming molecular clouds (e.g., Evans et al. 2014). This supports the idea that what we see emitting brightly in CO at low metallicities corresponds to the denser regions of molecular clouds.

In other aspects, the Magellanic Bridge A clouds are similar to clouds found in the Magellanic System and other low-metallicity galaxies. Their CO(2−1) emission has similar velocity dispersion and luminosity to other CO clouds studied in the Magellanic Bridge. Molecular clouds with radii $0.3 - 1$ pc, velocity FWHM $1 - 2$ $km\,s^{-1}$ and CO luminosities $10 - 100$ $K\,km\,s^{-1}\,pc^2$ have been found in Magellanic Bridge B (Saldaño et al. 2018). Magellanic Bridge C ^{12}CO(1-0) emission is concentrated in clouds with radii $0.9 - 1.5$ pc and velocity FWHM $0.5 - 1.4$ $km\,s^{-1}$ (Kalari et al. 2020), similar to the clouds we find in this work. The Magellanic Bridge A clouds have similar radii and slightly narrower linewidths and luminosities than regions in the LMC and SMC with active star formation, observed at similar (subparsec) resolution. For example, in 30 Doradus in the LMC, clouds with radii $\gtrsim 0.5$ pc show lines $1 - 6$ $km\,s^{-1}$ wide and CO(2−1) luminosities $\gtrsim 100$ $K\,km\,s^{-1}\,pc^2$ (Indebetouw et al. 2013). In N83 in the SMC, clouds with radii ~ 0.8 pc have linewidths of ~ 4 $km\,s^{-1}$ and CO(2−1) luminosities $100-200$ $K\,km\,s^{-1}\,pc^2$ (Muraoka et al. 2017). The narrower linewidths in Magellanic Bridge A may be the consequence of lower cloud masses, or alternatively lower external pressures (Field et al. 2011). Small clouds ($1 - 3$ pc radii) with linewidths around $2 - 3$ $km\,s^{-1}$ and high densities ($n(H2) \sim 10^3$ cm^{-3}) have been reported in dwarf galaxies like WLM (Rubio et al. 2015) and NGC6822 (Schruba et al. 2017). In general, our results support the idea that CO in low-metallicity galaxies traces dense regions of the molecular clouds, and is detected as compact, dense CO clouds with narrow linewidths (Rubio et al. 2015).

The α_{CO} CO-to-H_2 conversion factor values estimated in this work using the virial masses are around 2-4 times larger than the standard Milky Way disk value $\alpha_{CO}(MW) = 4.3$ $M_\odot$ $(K\ kms^{-1}\ pc^2)^{-1}$. Although large conversion factors are observed on large scales for low-metallicity galaxies, observations on small scales and in regions where CO is bright in low-metallicity cloud complexes frequently yield conversion factors α_{CO} similar to the canonical value for the Galaxy (e.g., Rubio et al. 2015; Schruba et al. 2017; Wong et al. 2017; Jameson et al. 2018). Rubio et al. (1993) found that in the SMC, X_{CO} decreases with cloud size as $\log X_{SMC} = 0.7 \log R + 20.26$ between 10 and 100 pc. Extending their relation for cloud sizes of $R \sim 1$ pc, the resulting value of X_{CO} is almost the canonical galactic value. For CO cloud North, α_{CO} is in good agreement with the value obtained for clouds sizes ~ 2 pc using the Rubio et al. (1993) relation. Therefore, the α_{CO} values we find in this work are consistent with α_{CO} values found for other low-metallicity regions at similar resolution.

3.3.2 Gas and dust comparison

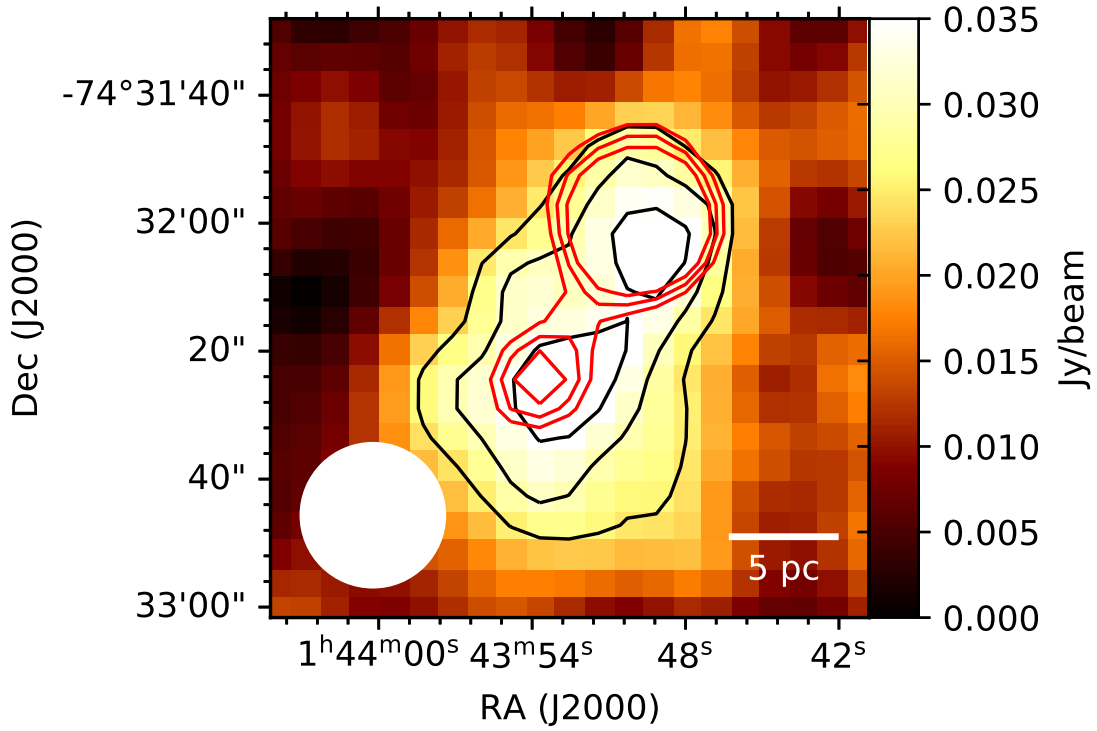

Figure 3.6: LABOCA continuum image at 870 μm, with black contours placed at 25, 30 and 35 mJy/beam, as in Figure 3.1. The white circle represents the beam size (beam FWHM= 22"). Red contours correspond to the ALMA and APEX CO(2−1) combined line emission convolved to the APEX resolution of 22", integrated between 172 and 176 km s^{-1}, at 5σ, 6σ and 7σ, where σ is the rms of the integrated image (σ = 1.8 Jy beam^{-1} km s^{-1}). The scalebar in the lower right corner represents a 5 pc length.

We compare the molecular gas and dust emission in Magellanic Bridge A by convolving the CO(2−1) ALMA and APEX combined cube to 22" resolution. We integrate the convolved CO(2−1) emission between 172 and 176 km s^{-1}. The rms noise of the resultant image is σ = 1.8 Jy beam^{-1} km s^{-1}. The CO(2−1) peaks can still be distinguished as separate sources at this resolution, but they share the same 3σ and 5σ contours (see Figure 3.6).

At this common resolution we can characterize the relative sizes of the sources in dust and CO by fitting two-dimensional Gaussians. In CO(2−1), the FWHM of the Gaussians are (7.1 ± 0.2) pc ×(6.6 ± 0.2) pc for cloud North, and (5.6 ± 0.4) pc ×(4.9 ± 0.3) pc for cloud South. Sources North and South in the 870 μm continuum are described by Gaussians with FWHM of (10.3 ± 0.6) pc ×(10.0 ± 0.7) pc and (16.9 ± 1.1) pc ×(16.5 ± 0.5) pc, respectively. The ratio of the continuum to CO spatial size for the North source is 1.5 ± 0.1, while for cloud South it is 3.0 ± 0.3. This difference in size (in particular for cloud South) suggests the presence of an extended halo of cold material, possibly molecular, that is not bright in CO. The expectation from photodissociation region models is that at low metallicity the region of a cloud that emits brightly in CO shrinks due to the diminished extinction caused by the lower dust-to-gas ratio (Bolatto et al. 2013).

It is interesting to note that not only is the size of the emission is larger in the long-wavelength dust continuum, but the gas mass estimates from the FIR dust continuum MBB fit to sources North and South are also a factor of $\sim 3-4$ higher than virial masses from CO (see Tables 3.3 and 3.6). This result is along the lines of previous studies in the SMC, where the total gas mass derived using CO emission is substantially lower than the cold gas mass obtained from modeling the dust emission (Rubio et al. 2004; Leroy et al. 2007; Bot et al. 2007, 2010a; Bolatto et al. 2011; Jameson et al. 2016). It is consistent with the idea that the CO-emitting regions of molecular clouds at low metallicity are encapsulated in a much larger cold gas envelope, likely molecular, that is not emitting in CO.

3.3.3 Gas and dust in the context of star formation

The North and South clouds in Magellanic Bridge A show differences in the mid-infrarred. In the 8 μm and 24 μm emission images of SAGE-SMC program, source North is detected with a flux density of 0.9 ± 0.1 mJy and 1.0 ± 0.1 mJy, respectively, whereas source South has a flux density of 7.1 ± 0.3 mJy and 60.0 ± 0.7 mJy (Gordon et al. 2011). The 8 μm emission is associated with the presence of polycyclic aromatic hydrocarbons (PAHs), which are components of dust and are usually correlated with star formation activity (Chen et al. 2014). The 24 μm emission is a tracer of warm dust, which is associated with massive star formation. The difference in flux densities at 24 μm is consistent with the presence of a B-type star towards the South cloud.

The CO(2−1) clouds in Magellanic Bridge A have ongoing star formation, with associated YSOs. The North source coincides with a faint YSO candidate (J014349.20-743200.63) classified by Chen et al. (2014), while the South source coincides with a brighter YSO (J014353.94-743224.71) classified as an embedded source in the same work. The South source hosts a compact multiple system, where a B-type star dominates the far-ultraviolet (FUV) light while the YSO in this location dominates the near-infrarred and mid-infrarred light (Chen et al. 2014). The dust temperature reflects this difference in stellar content: the South cloud is being heated by the multiple stars it hosts, in particular a B-type star, while the North cloud might be mostly heated by its fainter YSO. Therefore, it seems that the South molecular cloud has already had an episode of massive star formation, and indeed Chen et al. (2014) speculate that the formation of a group of early B stars $5-10$ Myr ago and the corresponding expansion of their HII regions (still visible in Hα) may have triggered the current star formation activity in Magellanic Bridge A.

Chapter 4

Molecular clouds near R136 in 30 Doradus

In this work, we characterize the emission in the 345 GHz window of the vicinity of R136 in 30 Doradus, between clouds 6 and 10 from Johansson et al. (1998), region which corresponds to the "Stapler Nebula" in Kalari et al. (2018). Section 4.1 describes the molecular clouds found in the vicinity of R136 using ^{12}CO(3-2) emission and how we obtain their properties. We study the ^{13}CO(3-2), CS(7-6) HCO^+(4-3) and HCN(4-3) line emissions in the molecular clouds near R136 in Section 4.2. Section 4.3 describes the submillimeter emission we find near R136 and shows the gas masses derived from dust emission. In Section 4.4, we compare the spatial extension and the total gas mases derived from CO and continuum emission. We discuss our results in Section 4.5.

4.1 Molecular Clouds near R136

A visual inspection reveals that the ^{12}CO(3-2) cube shows emission in the velocity range of 200 and 290 km s^{-1}, approximately. Molecular emissions consist of clumpy structures, mostly concentrated in a diagonal that goes from the northwest to the southeast (see Figure 4.1). We see smaller and less bright clouds outside of this diagonal structure, particularly at the bottom edge of the map.

In section 4.1.1, we identify and characterize the molecular clouds located in the field of view, using ^{12}CO(3-2) line emission, as it presents the strongest line emission of our sample. We obtain the physical properties of the ^{12}CO(3-2) clouds we find in Section 4.1.2.

4.1.1 Cloud identification

We detect molecular clouds near R136 using the ^{12}CO(3-2) line as the primary emission tracer. This cube has a resolution of 4.6" × 4.0" (see Table 2.2), which, at a distance of 50 kpc, allows us to resolve clouds with radii down to $\sim$ 1 pc. Even though we calculate the noise $\sigma = 47$ mK in the ^{12}CO(3-2) line cube, σ is not uniform: as the primary beam response is lower towards the edges than the center, the noise increases radially. To identify ^{12}CO(3-

2) clouds in the ALMA line cube, we apply the algorithm described in Rosolowsky & Leroy (2006) to our ^{12}CO(3-2) data by using the IDL package CPROPS[1], which we describe further in the following. We inspect the results to leave out false detections and compare the results with what we observe in the ^{12}CO(3-2) line cube. We obtain the detection properties of a subset of clouds which are not accurately decomposed by CPROPS using a Gaussian fitting method. We first present the detected emission and then detail how clouds are decomposed.

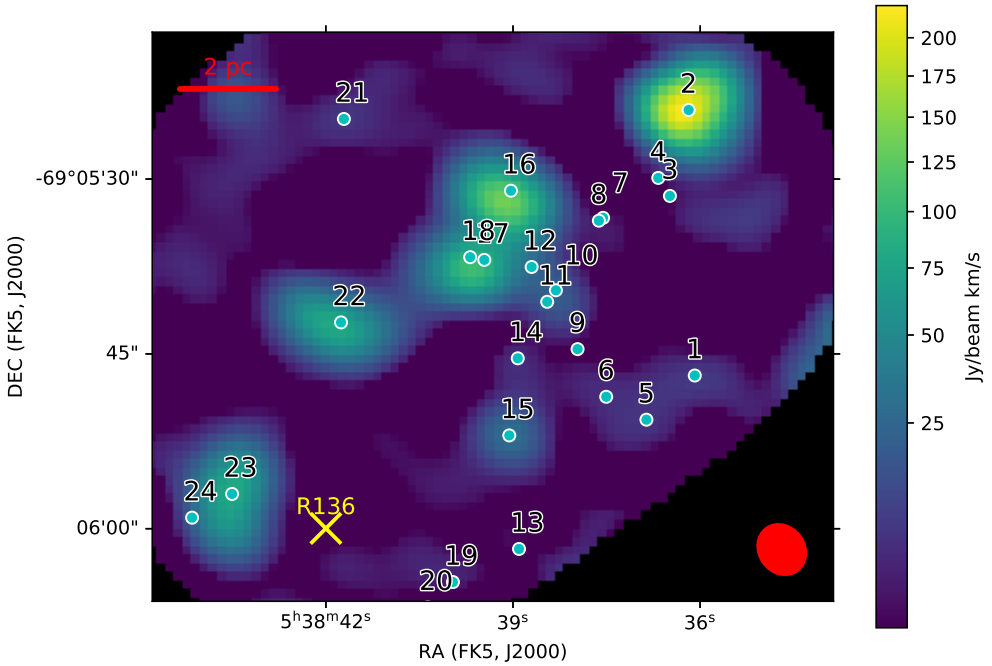

Figure 4.1: ALMA ^{12}CO(3-2) line cube of the vicinity of R136 in 30Dor, integrated between 217 and 285 km s^{-1}. Cyan points with white edges represent the position of the detected clumps in Table 4.1. Each point is labeled according to the corresponding detection no. from Table 4.1. The red solid ellipse in the lower right corner represents the ^{12}CO(3-2) line cube beam FWHM in its major and minor axes. The yellow cross represents the central position of R136. The red scalebar represents a length of 2 pc.

We detect a total of 24 molecular clouds in the ^{12}CO(3-2) line cube. We plot the detections in Figure 4.1 with ellipses that represent the extrapolated (but not deconvolved) radii along the major and minor axes of the clump (see Section 4.1.2), as detected in CPROPS. We present the list and parameters of the 24 clouds in Table 4.1, where we include their identification number, position in right ascension (α) and declination (δ), peak temperature (T_{peak}), central velocity (v), full-width at half-maximum (FWHM, Δv) and luminosity delivered by CPROPS $L_{^{12}CO(3-2)}$ (defined in Section 4.1.2). The clouds which have been characterized by the Gaussian fitting method correspond to clouds no. 7, 8, 16, 17 and 18.

CPROPS cloud identification

We describe how we use the CPROPS algorithm and the parameters used in the following; a more detailed description of the procedure is in the CPROPS user guide[2] and in Rosolowsky

[1]https://people.ok.ubc.ca/erosolo/cprops/index.html
[2]https://people.ok.ubc.ca/erosolo/cprops/man.cprops.pdf

Cloud no.	α (J2000)	δ (J2000)	T_{peak} (K)	v (km s^{-1})	Δv * (km s^{-1})	$L_{^{12}CO(3-2)}$ (K km s^{-1} pc^{-2})
1	05:38:36.1	-69:05:46.9	1.31	271.2 ± 0.6	1.3 ± 0.2	2.2 ± 0.3
2	05:38:36.2	-69:05:24.1	25.74	250.2 ± 1.8	4.2 ± 0.2	268.6 ± 22.1
3[c]	05:38:36.5	-69:05:31.5	0.60	219.2 ± 0.8	1.9 ± 0.2	1.5 ± 0.2
4[c]	05:38:36.7	-69:05:29.9	0.25	221.1 ± 0.5	1.1 ± 0.5	0.2 ± 0.0
5[c]	05:38:36.9	-69:05:50.7	0.50	279.8 ± 1.1	2.5 ± 0.4	1.3 ± 0.1
6[c]	05:38:37.5	-69:05:48.7	0.28	255.0 ± 1.1	2.6 ± 0.5	0.8 ± 0.2
7[†c]	05:38:37.6	-69:05:33.3	0.28	224.7 ± 1.1	2.6 ± 0.2	1.0 ± 0.1
8[†c]	05:38:37.6	-69:05:33.6	0.76	227.6 ± 0.9	2.1 ± 0.1	1.8 ± 0.1
9[c]	05:38:38.0	-69:05:44.6	0.31	228.5 ± 0.8	2.0 ± 0.3	0.7 ± 0.1
10	05:38:38.3	-69:05:39.5	1.75	246.8 ± 1.1	2.5 ± 0.3	6.2 ± 0.6
11	05:38:38.5	-69:05:40.5	1.30	232.5 ± 1.5	3.6 ± 0.2	7.2 ± 0.6
12	05:38:38.7	-69:05:37.5	2.08	237.4 ± 1.2	2.9 ± 0.2	10.4 ± 0.8
13	05:38:38.9	-69:06:01.7	1.00	276.2 ± 1.2	2.7 ± 0.3	3.6 ± 0.3
14	05:38:38.9	-69:05:45.4	1.52	241.3 ± 0.9	2.1 ± 0.3	4.2 ± 0.4
15	05:38:39.1	-69:05:52.0	4.23	247.5 ± 1.6	3.6 ± 0.3	22.6 ± 1.9
16[†]	05:38:39.2	-69:05:31.8	25.13	244.4 ± 1.3	3.1 ± 0.0	216.2 ± 4.2
17[†]	05:38:39.6	-69:05:37.7	9.20	245.4 ± 1.9	4.3 ± 0.3	101.6 ± 3.4
18[†]	05:38:39.8	-69:05:37.5	8.23	241.3 ± 1.0	2.4 ± 0.1	66.9 ± 2.8
19[c]	05:38:40.0	-69:06:04.6	0.64	267.5 ± 0.9	2.2 ± 0.4	1.3 ± 0.1
20	05:38:40.4	-69:06:06.7	0.76	273.2 ± 2.0	4.6 ± 0.5	3.3 ± 0.3
21[c]	05:38:41.7	-69:05:24.8	0.53	254.2 ± 0.8	1.8 ± 0.3	1.3 ± 0.1
22	05:38:41.8	-69:05:42.3	13.15	237.7 ± 1.3	3.0 ± 0.2	107.2 ± 8.9
23	05:38:43.5	-69:05:57.0	11.49	235.9 ± 1.5	3.5 ± 0.2	112.5 ± 9.1
24[c]	05:38:44.1	-69:05:59.1	0.49	227.8 ± 1.2	2.9 ± 0.4	1.3 ± 0.1

Table 4.1: 30Dor detections in the ^{12}CO(3-2) line cube obtained using CPROPS. The CO(3-2) luminosity is calculated by CPROPS according to Equation 4.1. *The velocity FWHM is corrected for sensibility and resolution bias. [†]Characterized using a manual method, described in section 4.1.1.[c] Clouds with low luminosity ($L_{^{12}CO(3-2)} < 2$ K km s^{-1} pc^{-2}) will not be used to calculate physical properties.

& Leroy (2006).

CPROPS identifies emission in "islands" over a certain noise level and decomposes them into single clouds, assigning each pixel in the line cube to a cloud or as background noise. We set the parameters THRESH = 3σ and EDGE = 1.5σ to define the initial mask, from which CPROPS will decompose the emission. To account for the non-uniform noise in our line cube, we input the /NONUNIFORM flag, so that the program calculates the noise σ at each sky position. CPROPS removes islands from the mask which are smaller than a certain area, that present a peak smaller than a certain minimum peak value or possess less than a certain number of channels. We set the minimum area with the MINAREA parameter, which we set to MINAREA = 0.5 resolution elements (beam area). We set the minimum peak value with the MINPEAK parameter, which we set to MINPEAK = 3σ. We set the minimum number of contiguous channels with the MINVCHAN parameter, which we set to

MINVCHAN = 3 channels (which equals 0.6 km s^{-1}). We use the ECLUMP variation of the CPROPS algorithm, which allows emission shared within a single brightness contour level by two clouds to be assigned into the cloud with the closest peak,using the CLUMPFIND algorithm (Williams et al. 1994). A detailed explanation of what the ECLUMP variation does can be found in the CPROPS user guide. Finally, we set BOOTSTRAP = 1000 so CPROPS does 1000 bootstrap iterations to estimate the uncertainties in the detection properties.

We manually inspect the results delivered by CPROPS to check for false detections, possibly caused by artifacts in the interferometric data. The program identifies a total of 49 clouds, 35 of which have a signal-to-noise ratio (S/N) higher than 5 (around 70% of the total). From the 35 clouds with S/N > 5, we determine that 4 of them are false detections caused by the superposition of emission arising from the sidelobes of stronger neighboring clouds. We also discard 8 clouds which are at the borders of the mapped area and, therefore, are not completely sampled.

For the remaining 23, after the manual inspection, we determine that there are 19 clouds identified by CPROPS which are consistent with what we observe in the ^{12}CO(3-2) line cube, and the remaining 4 clouds are not totally consistent with what we see in the visual inspection. We keep the 19 clouds that are consistent with what we observe and use the manual method to obtain the properties of the remaining 4 clouds, which the visual inspection indicates might actually be 5 clouds, described in the following paragraphs.

Gaussian fitting method

Inspecting the 23 clouds identified by CPROPS we realize that in four of them, the properties given by CPROPS are not consistent with the manual and visual inspection of the cube. Three of these clouds, no. 16, 17 and 18 from Table 4.1, turn out to be spatially blended clouds, while the fourth cloud resolves into two different clouds, corresponding to no. 7 and 8 in Table 4.1. In order to obtain the properties of these clouds we do the following.

To obtain the properties of the 3 blended clouds, we integrate the ^{12}CO(3-2) line cube in the velocity range between 236.7 and 250.9 km/s, so as to produce an velocity integrated image of the blended clouds. In this velocity integrated image, we identify two clouds, as shown in the left panel of Figure 4.2a. We define the area of each cloud as the 3σ contour for this image, that has a σ = 2.6 Jy/beam km/s. We obtain the spectra of each cloud by adding up all the spectra inside the area of each cloud. In the cloud seen towards the northwest, corresponding to cloud no. 16 from Table 4.1, its spectra is well fitted using one Gaussian component, with a central velocity of v = 244.40 km s^{-1} and a velocity dispersion σ_v = 1.34 km s^{-1}, as shown in the top right panel of Figure 4.2a. In the case of the cloud seen towards the south east and encircled in red in 4.2a, the spectra is best fitted using 4 Gaussian components, shown in the bottom right panel of Figure 4.2a. The Gaussian components 1 and 3 (the orange and red lines) show central velocities that suggest that these components are associated to different clouds but in the same line of sight. The Gaussian fit to the spectra gives for component 1 (orange line) a central velocity v = 241.30 km s^{-1} and σ_v = 1.04 km s^{-1}, and for component 3 (red line), a central velocity v = 245.40 km s^{-1} and σ_v = 1.85 km s^{-1}. Component 1 corresponds to cloud no. 18 and component 2, to cloud no. 17 from Table 4.1. The other two fit components can be associated to the clouds correctly identified and characterized by CPROPS. The Gaussian component 2 (green line)

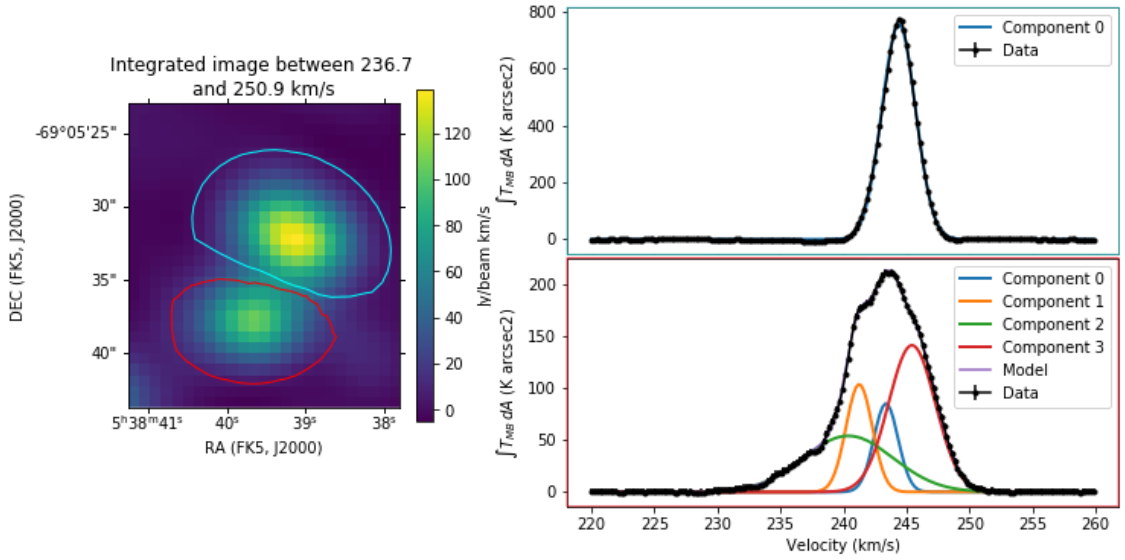

(a)

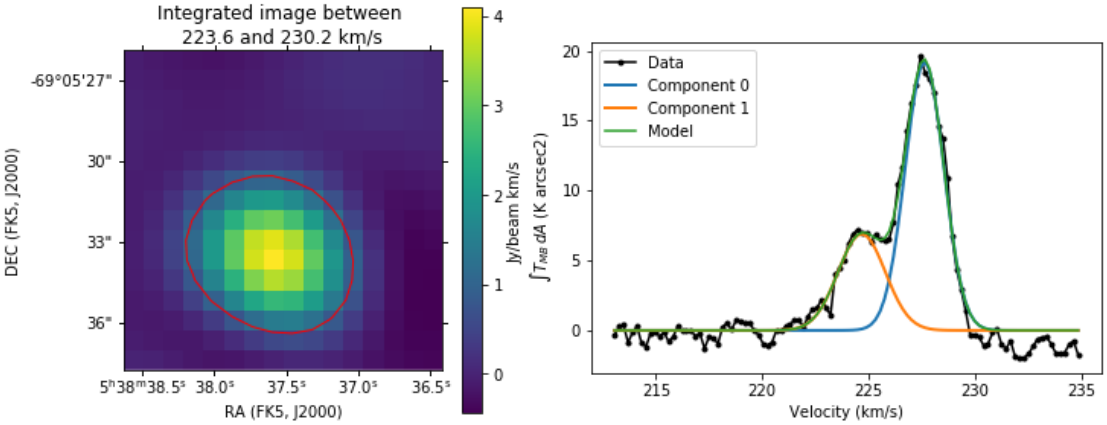

(b)

Figure 4.2: Velocity integrated ^{12}CO(3-2) images of the vicinity of R136 in 30Dor, in the locations of the 5 clouds we characterize manually, together with their integrated spectra. Black points correspond to the integrated spectra in each region. (a) ^{12}CO(3-2) emission integrated between 236.7 and 250.9 km/s of clouds 16, 17 and 18. The top spectra corresponds to the integrated spectra inside the cyan contour, and the bottom spectra corresponds to the red contour. The bottom spectra shows a complex profile, fitted with 4 Gaussian components, each of which is associated with a cloud. (b) ^{12}CO(3-2) emission integrated between 223.6 and 230.9 km/s for clouds 7 and 8, together with the integrated spectra in the red region. The spectra shows two gaussian components, 0 and 1, associated with clouds 8 and 7, respectively.

can be associated to emission from cloud no. 12, which lies in the same line of sight, while the Gaussian component 0 (blue line) is associated to emission from cloud no. 16, the one towards the northwest. To determine the properties of the two clouds associated with the red and orange Gaussian fits, we integrate the ^{12}CO(3-2) line cube in the range $(v-2\sigma_v, v+2\sigma_v)$ for each cloud, to produce the velocity integrated image of each cloud. From this image we determine the central position and the major and minor axis sizes of the clouds using the

same moment method used in CPROPS, described in Rosolowsky & Leroy (2006).

To obtain the properties of the fourth cloud, we proceed in the same way as for the three blended clouds but we integrate the CO line cube in a different velocity range, between 223.6 and 230.2 km s^{-1}. In this cloud the velocity integrated image has $\sigma = 0.3$ Jy/beam km s^{-1} and the area is the one enclosed by the 3σ contour (see Figure 4.2b). We obtain the spectra in the same way as explained in the previous paragraph. The resulting spectra is well fitted by two Gaussian components with different central velocities as shown in the right panel of Figure 4.2b. We thus consider that we have two different clouds which are clearly separated in velocity but are located in the same line of sight. One cloud is associated to the Gaussian component 0 (blue line) with a central velocity $v = 227.6$ km s^{-1} and velocity dispersion $\sigma_v = 0.91$ km s^{-1}. The other cloud, associated with the Gaussian component 1 (orange line) has a central velocity $v = 224.7$ km s^{-1} and velocity dispersion $\sigma_v = 1.11$ km s^{-1}. Component 0 corresponds to cloud no. 8 and component 1, to cloud no. 7, from Table 4.1. We obtain their properties in the same way as described in the previous paragraph.

Through this methodology, we identify 5 individual clouds (no. 7, 8, 16, 17 and 18 from Table 4.1), confirming that the 3 blended clouds identified by CPROPS are indeed 3 individual clouds and that the 4th one, which CPROPS identified as one cloud, consists of two individual sources. Therefore, from the 23 clouds originally identified by CPROPS, we end up with a total of 24 clouds.

4.1.2 Physical properties of molecular clouds near R136

We determine the radius R, the total luminosity L_{CO}^{LMC}, the virial mass M_{vir} and mass derived from CO luminosity (luminous mass) M_{CO} of each cloud. We do not calculate the properties of the candidate clouds in Table 4.1, which have low luminosities and are unresolved. We adopt the standard CPROPS definitions for the radii, velocity dispersion, CO luminosity and virial mass. The CO luminosity of each cloud are in Table 4.1, and the rest are presented in Table 4.2.

The radius is obtained using Equation 1.2, where σ_r is in radians and $D = 50$ kpc (Pietrzyński et al. 2013).

The ^{12}CO(3-2) luminosity of a cloud $L_{^{12}CO(3-2)}$ in K km s^{-1} pc^2 is the sum of the flux of all the voxels in the mask defined by CPROPS that correspond to the cloud, scaled by the square of the distance, using:

$$L_{^{12}CO(3-2)} = F_{^{12}CO(3-2)}(0K) D^2 \Big(\frac{\pi}{180 \times 3600}\Big)^2, \tag{4.1}$$

(Rosolowsky & Leroy 2006) where $F_{^{12}CO(3-2)}(0K)$ is the flux of the cloud corrected for sensitivity bias in K km s^{-1} arcsec^2, D is the distance to the cloud in pc (for 30Dor we use $D = 50$ kpc) and a correction is applied at the end to transform arcseconds to radians.

The virial mass is calculated using Equation 1.13, which assumes that clouds have a spherical shape with a density profile $\rho(r) \propto r^{-1}$.

We also calculate the gas mass traced by CO luminosity, M_{CO}^{LMC}, using Equation 1.8, where

L_{CO} is the ^{12}CO(1-0) luminosity of each cloud. We transform the ^{12}CO(3-2) luminosities of our clouds into ^{12}CO(1-0) luminosities, using a line ratio $R_{\frac{3-2}{1-0}} \sim 2$, as determined by Johansson et al. (1998) for the 30Dor-10 cloud. For the conversion factor, α_{CO}, we use the value obtained by Indebetouw et al. (2013), $\alpha_{CO} = 8.4 \pm 3.0$ M$_\odot$ pc^{-2} (K km s^{-1})$^{-1}$, for 30Dor-10 cloud at 0.6 pc resolution.

For comparison, we also calculate the molecular mass M_{CO}^{MW}, using the canonical Milky Way disk conversion factor $\alpha_{CO}(MW) = 4.3$ M$_\odot$ pc^{-2} (K km s^{-1})$^{-1}$.

We calculate the H$_2$ surface density $\Sigma_{\rm H_2}$ using $\Sigma_{H_2} = M_{CO}^{LMC}/(\pi R^2)$, with the M_{CO}^{LMC} and R values from Table 4.2. This assumes that $M_{CO}^{LMC} \approx M_{\rm H_2}$. We choose to calculate $\Sigma_{\rm H_2}$ using the mass derived from CO luminosity to discuss how close these molecular clouds are to self-gravity in Section 4.5.2.

ID	R (pc)	M_{vir} ($M_\odot$)	M_{CO}^{LMC} ($M_\odot$)	$\Sigma_{\rm H_2}$ ($M_\odot$ pc^{-2})	M_{CO}^{Gal} ($M_\odot$)	$\frac{M_{vir}}{M_{CO}^{LMC}}$
1	$< 0.84 \pm 0.23^{**}$	$< 266 \pm 91$	9 ± 3	$> 4.2 \pm 2.3$	4.9 ± 0.7	$< 28.4 \pm 14.7$
2	0.71 ± 0.10	2414 ± 382	1127 ± 413	712.0 ± 297.9	585.5 ± 48.2	2.1 ± 0.9
10	$0.32 \pm 0.06^{*}$	383 ± 87	26 ± 9	81.5 ± 36.3	13.5 ± 1.2	14.7 ± 6.4
11	$0.40 \pm 0.04^{*}$	995 ± 144	30 ± 11	60.2 ± 23.9	15.7 ± 1.3	32.9 ± 13.0
12	$0.40 \pm 0.06^{*}$	645 ± 115	43 ± 15	86.8 ± 36.0	22.7 ± 1.8	14.8 ± 6.0
13	$< 0.84 \pm 0.19^{**}$	$< 1186 \pm 319$	15 ± 5	$> 6.8 \pm 3.3$	7.8 ± 0.7	$< 79.1 \pm 36.0$
14	$< 0.84 \pm 0.18^{**}$	$< 682 \pm 191$	17 ± 6	$> 7.9 \pm 3.8$	9.1 ± 0.9	$< 39.1 \pm 18.2$
15	$< 0.84 \pm 0.12^{**}$	$< 2118 \pm 375$	95 ± 34	$> 42.9 \pm 17.9$	49.4 ± 4.1	$< 22.3 \pm 9.1$
16	$0.48 \pm 0.01^{*}$	902 ± 19	907 ± 324	1259.3 ± 452.0	471.3 ± 9.1	1.0 ± 0.4
17	$0.33 \pm 0.01^{*}$	1171 ± 103	426 ± 153	1276.8 ± 462.0	221.5 ± 7.5	2.7 ± 1.0
18	$0.44 \pm 0.02^{*}$	498 ± 37	281 ± 101	463.7 ± 169.8	145.9 ± 6.0	1.8 ± 0.7
20	$0.33 \pm 0.05^{*}$	1357 ± 297	13 ± 5	40.0 ± 17.3	7.2 ± 0.7	97.3 ± 41.8
22	0.71 ± 0.14	1225 ± 252	450 ± 165	282.2 ± 128.7	233.8 ± 19.5	2.7 ± 1.1
23	0.67 ± 0.12	1578 ± 310	472 ± 173	336.6 ± 151.3	245.3 ± 19.9	3.3 ± 1.4

Table 4.2: Physical properties of the 30Dor clouds. The table does not include cloud no. 24, because it includes emission from sidelobes of other stronger clouds. These values are corrected for sensitivity and resolution bias. M_{CO}^{LMC} is calculated using $\alpha_{CO} = 8.4 \pm 3.0$ M$_\odot$ pc^{-2} (K km s^{-1})$^{-1}$ (Indebetouw et al. 2013), assuming $R_{\frac{3-2}{1-0}} \sim 2$ Johansson et al. (1998). M_{CO}^{Gal} is calculated using the canonical conversion factor for ^{12}CO(2-1) $X_{CO} = 2 \times 10^{20}$ cm^{-2} (K km s^{-1})$^{-1}$. $\Sigma_{\rm H_2}$ is calculated using M_{CO}^{LMC} and R values in this table. In the cases where clouds are not spatially resolved (both axes unresolved), virial masses are calculated as upper limits. *Minor axis is unresolved. **Both axes are unresolved.

The physical properties in Table 4.2 and the velocity FWHM in Table 4.1 are corrected for sensitivity and resolution bias. Both biases are described in depth in Rosolowsky & Leroy (2006) and are accounted for in the calculation of the second moments σ_r and σ_v. To correct for the sensitivity bias, we extrapolate the clouds second moments to values that would be expected in the limiting case of perfect sensitivity (if the edge of the cloud was at $T = 0$ K). This is done as part of the CPROPS routine. We do not extrapolate the radii for clouds no. 7, 8, 16, 17 and 18 (which are characterized using the manual method described in Section

4.1.1). To correct for resolution bias, we deconvolve the beam size and width of a spectral channel from σ_r and σ_v, respectively. For σ_r, we use 3.4, and for σ_v, we use 3.3.

In several cases, one or both of the second moments of emission along the principal axes of the clump is smaller than σ_{beam}. For these cases, we calculate σ_r using:

$$\sigma_r = \sqrt{\sigma_{beam}(\sigma_{maj}(0K) - \sigma_{beam})}, \tag{4.2}$$

where $\sigma_{maj}(0K)$ is the extrapolated second moment of the major axis. If both axes are smaller than the beam, the cloud is unresolved and we adopt $\sigma_r = \sigma_{beam}$, which is considered as an upper limit to the size of the cloud.

Table 4.2 summarizes R, FWHM Δv, the virial mass M_{vir}, molecular mass estimated from CO luminosity using an LMC conversion factor M_{CO}^{LMC} and molecular masses with the standard galactic conversion factor M_{CO}^{Gal} for the clouds we find in the ALMA ^{12}CO(3-2) line cube. We also add for reference the ratio between the virial mass and the luminous mass using the LMC conversion factor, $\frac{M_{vir}}{M_{CO}^{LMC}}$. The clouds have radii between 0.3 and 0.9 pc, luminosities between 1 and 269 K km s^{-1} pc^2, virial masses between 88 and 2414 M$_\odot$ and luminous masses M_{CO}^{LMC} between 3 and 1128 M$_\odot$.

We plot R v/s Δv and M_{vir} v/s $L_{^{12}CO(1-0)}$ for the molecular clouds which are completely resolved and clouds which have their minor axis unresolved in Figure 4.3, together with the relations between these properties found for molecular clouds in the first quadrant of the Milky Way by Solomon et al. (1987), which are $\Delta v = 1.69R^{0.5}$ (which comes from the relationship between the velocity dispersion σ_v and R, $\sigma_v = 0.72R^{0.5}$) and $M_{vir} = 39(L_{^{12}CO(1-0)})^{0.81}$. The $L_{^{12}CO(3-2)}$ luminosities are transformed to $L_{^{12}CO(1-0)}$ using $R_{\frac{3-2}{1-0}} \sim 2$ (Johansson et al. 1998). Our clouds have larger velocity dispersions than what is predicted for these radii by the relation found by Solomon et al. (1987), which could be related to a larger turbulence in the clouds near R136. This trend was observed in the previous observations in CO(2-1) line emission by Kalari et al. (2018), and was also observed in other 30Dor clouds (Pineda et al. 2009; Nayak et al. 2016). We will further compare the radius and velocity dispersion of the clouds near R136 with other clouds in 30Dor and other galaxies in Section 4.5.2. The clouds with luminosities $L_{^{12}CO(3-2)} > 10$ K km s^{-1} pc^2 (no. 2, 16, 17, 18, 22 and 23) follow the relation between M_{vir} and $L_{^{12}CO(1-0)}$ found in the galaxy, whereas the clouds with $L_{^{12}CO(3-2)} < 10$ K km s^{-1} pc^2 (no. 10, 11, 12 and 20) have a larger virial mass than what is predicted by the Solomon et al. (1987) relation. The latter clouds are unresolved in one of their axis, so the virial mass in these cases might be overestimated as we truncate their size in the minor axis to the size of the beam.

M_{vir} masses are larger than M_{CO}^{LMC} for all clouds except for cloud no. 15, in which the ratio between both masses has an upper limit of 1. As the majority of the clouds are not resolved, their virial masses are an upper limit, so the $\frac{M_{vir}}{M_{CO}^{LMC}}$ ratios are an upper limit as well. For the resolved clouds (no. 2, 22 and 23), the $\frac{M_{vir}}{M_{CO}^{LMC}}$ ratio is between 2 and 3.3. This difference could be explained if the conversion factor in this region is different from the one we assumed, $\alpha_{^{12}CO} = 8.4 \pm 3.0$ M$_\odot$ pc^{-2} (K km s^{-1})$^{-1}$. If we assume $M_{vir} \approx M_{H_2}$, the conversion factor for this region would be between $\alpha_{^{12}CO} = 16.8$ and 27.7 M$_\odot$ pc^{-2} (K km s^{-1})$^{-1}$. These $\alpha_{^{12}CO}$ values are between 4 to 6 times larger than the canonical galactic conversion value of

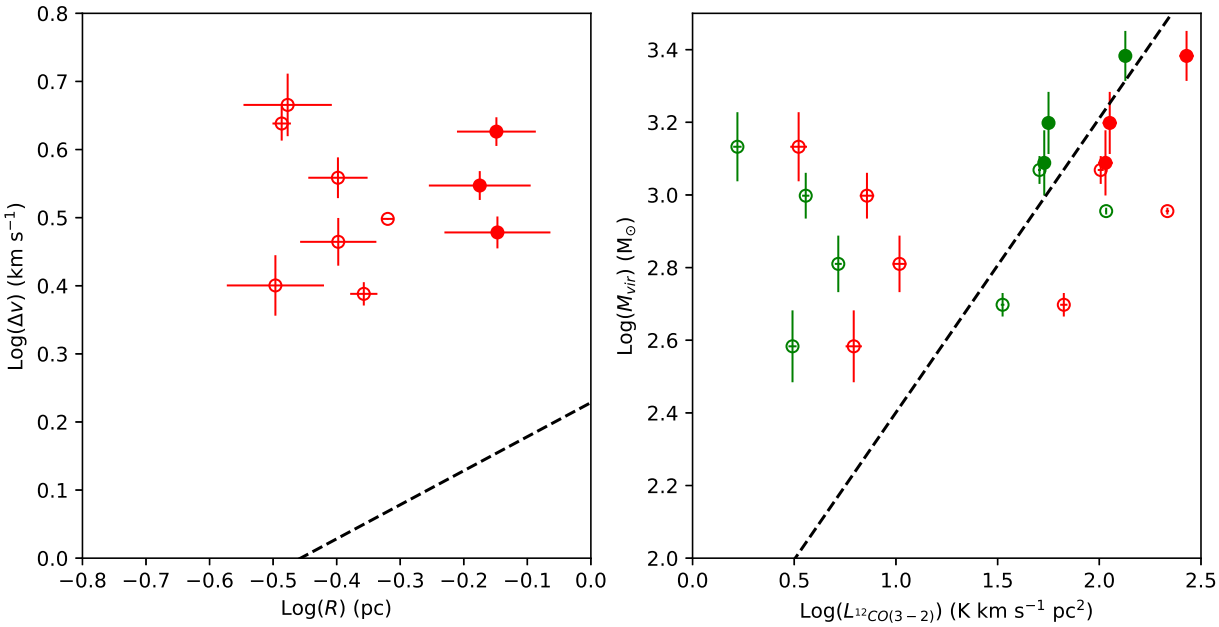

Figure 4.3: Relationships between the physical properties observed in the resolved clouds found near R136 in 30Dor. Filled red circles correspond to completely resolved molecular clouds, whereas empty red circles correspond to molecular clouds where the minor axis is unresolved. Left: relationship between the radius R and the velocity FWHM Δv. The dashed line represents the relationship found for molecular clouds in the first Galactic quadrant by Solomon et al. (1987), $\Delta v = 1.69R^{0.5}$. Right: relationship between the virial mass M_{vir} and the ^{12}CO(3-2) luminosity $L_{^{12}CO(3-2)}$. Green dots plot the relation between M_{vir} and $L_{^{12}CO(1-0)}$ for resolved (filled circles) and not resolved (empty circles) clouds, where the luminosities $L_{^{12}CO(3-2)}$ are transformed to $L_{^{12}CO(1-0)}$ using $R_{\frac{3-2}{1-0}} \sim 2$ (Johansson et al. 1998). Dashed line represents the relationship found for molecular clouds in the first Galactic quadrant by Solomon et al. (1987), $M_{vir} = 39(L_{^{12}CO(1-0)})^{0.81}$.

$\alpha_{^{12}CO} = 4.3$ M$_\odot$ pc^{-2} (K km s^{-1})$^{-1}$. The difference between M_{CO}^{LMC} and M_{vir} could also be the result of the virial mass tracing the external pressure suffered by the clouds as well as the total gas mass. We discuss the virial mass in further detail in Sections 4.5.2 and 4.5.4.

4.2 Molecular Species in the Region

In this section, we investigate the molecular emission from ^{13}CO(3-2), CS(7-6), HCO$^+$(4-3) and HCN(4-3) in the vicinity of R136, and compare it with our findings in ^{12}CO(3-2). We determine the clouds in ^{12}CO(3-2) from Section 4.1 which have emission in ^{13}CO(3-2), CS(7-6), HCO$^+$(4-3) and/or HCN(4-3) in Section 4.2.1. We obtain the integrated line intensities at the peak temperature positions of ^{12}CO(3-2), ^{13}CO(3-2), CS(7-6), HCO$^+$(4-3) and HCN(4-3) detections in Section 4.2.2. We calculate the kinetic temperature and the column density $N(H_2)$, using the local thermodynamic equilibrium (LTE) approximation for the peak emission of each cloud, using the ^{13}CO(3-2), and ^{12}CO(3-2) line emission, in Section 4.2.4.

4.2.1 Identification of molecular emission

We identify the molecular cloud emission in ^{13}CO(3-2), CS(7-6), HCO$^+$(4-3) and HCN(4-3), using CPROPS with the same parameters as those used to identify the ^{12}CO(3-2) clouds (see Section 4.1.1). We also manually inspect the results to leave out false detections provoked by artifacts. We list the detections and their properties (position, central velocity, velocity FWHM and sizes) obtained using CPROPS in Appendix A. We detect 14 molecular clouds in ^{13}CO(3-2), located between 225 and 255 km s^{-1}, 8 in CS(7-6) between 233 and 253 km s^{-1}, 13 in HCO$^+$(4-3) between 225 and 255 km s^{-1} and 7 in HCN(4-3) between 233 and 253 km s^{-1}. In the following, we use the ^{12}CO(3-2) cloud number to identify the clouds in the other molecules. We list which cloud is detected in which molecular line in Table 4.3. The central positions of the detections are plotted over velocity integrated images for each molecule in Figure 4.4 and their positions are plotted all together in Figure 4.5. All molecular emission from ^{13}CO(3-2), CS(7-6), HCO$^+$(4-3) and HCN(4-3) lines is associated to the brightest clouds found in ^{12}CO(3-2) emission, as seen in Figure 4.5. We describe the distribution of the clouds we find in each molecular species in the following. We do not analyze in depth the sizes of the clouds given by CPROPS in this work, as we are only interested in the locations of the different emissions.

Cloud no.	^{13}CO(3-2)	CS(7-6)	HCO$^+$(4-3)	HCN(4-3)
2	x	x	x	x
8	x		x	
9	x		x	
10	x	x	x	x
11	x		x	
12	x		x	
14	x		x	
15	x		x	x
16	x	x	x	x
17	x	x	x	x
18	x	x		
21	x		x	
22	x	x	x	x
23	x	x	x	x

Table 4.3: Summary of the ^{12}CO(3-2) molecular clouds detected in the ^{13}CO(3-2), CS(7-6), HCO$^+$(4-3) and HCN(4-3) line emission cubes. Clouds which are not listed here are only detected in ^{12}CO(3-2) emission.

We find emission of all molecular species associated to six ^{12}CO clouds (no 2, 10, 16, 17, 22 and 23, see Figure 4.5). These clouds are all located in the nortwest-southeast diagonal where we find the strongest ^{12}CO(3-2) emission. The largest T_{peak} values for all molecular

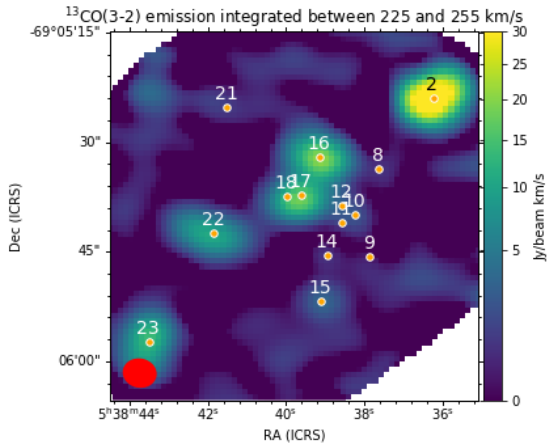

(a) ^{13}CO(3-2) emission integrated between 225 and 255 km/s.*

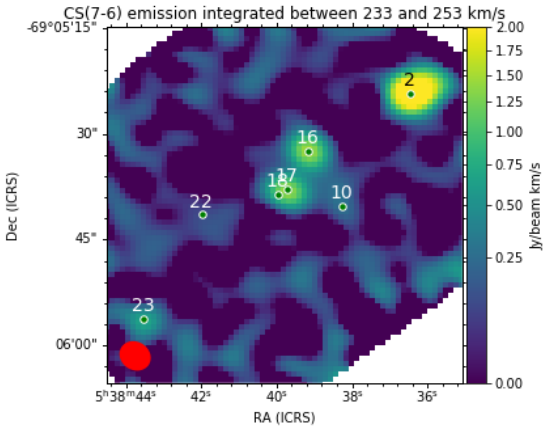

(b) CS(7-6) emission integrated between 233 and 253 km/s.

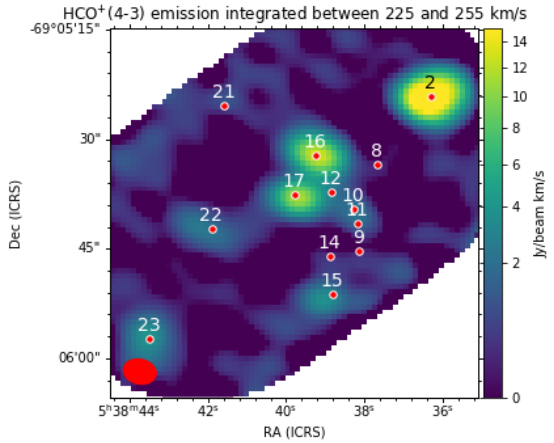

(c) HCO$^+$(4-3) emission integrated between 225 and 255 km/s.

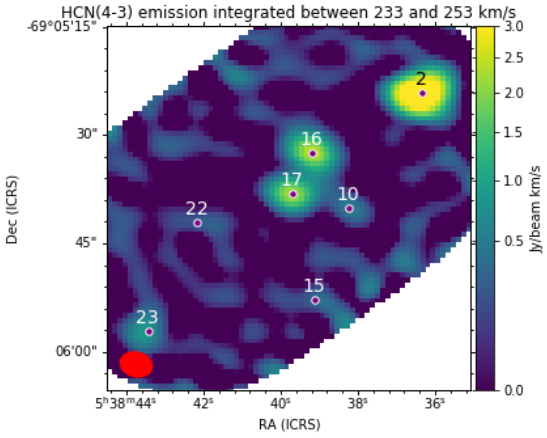

(d) HCN(4-3) emission integrated between 233 and 253 km/s.

Figure 4.4: Velocity integrated images of the different molecular species studied in the vicinity of R136 in 30Dor. Orange labeled dots correspond to the central position of the ^{13}CO(3-2) CPROPS detections. Green labeled dots mark the central position of the CS(7-6) CPROPS detections. Red labeled dots show the central position of the HCO$^+$(4-3) CPROPS detections. Purple labeled dots correspond to the central position of the HCN(4-3) CPROPS detections. The red ellipse in the lower left corner represents the beam size.

species are found in cloud no. 2 (according to the tables in Appendix A), which is the farthest away in proejection from R136. As CS(7-6) and HCN(4-3) have higher critical densities ($n_{crit} \sim 10^7$ cm^{-3} for CS(7-6) and $n_{crit} \sim 10^8$ cm^{-3} for HCN(4-3) at 10 K) than HCO$^+$(4-3) ($n_{crit} \sim 10^6$ cm^{-3} at 10 K), and CS and HCN are found exclusively in the

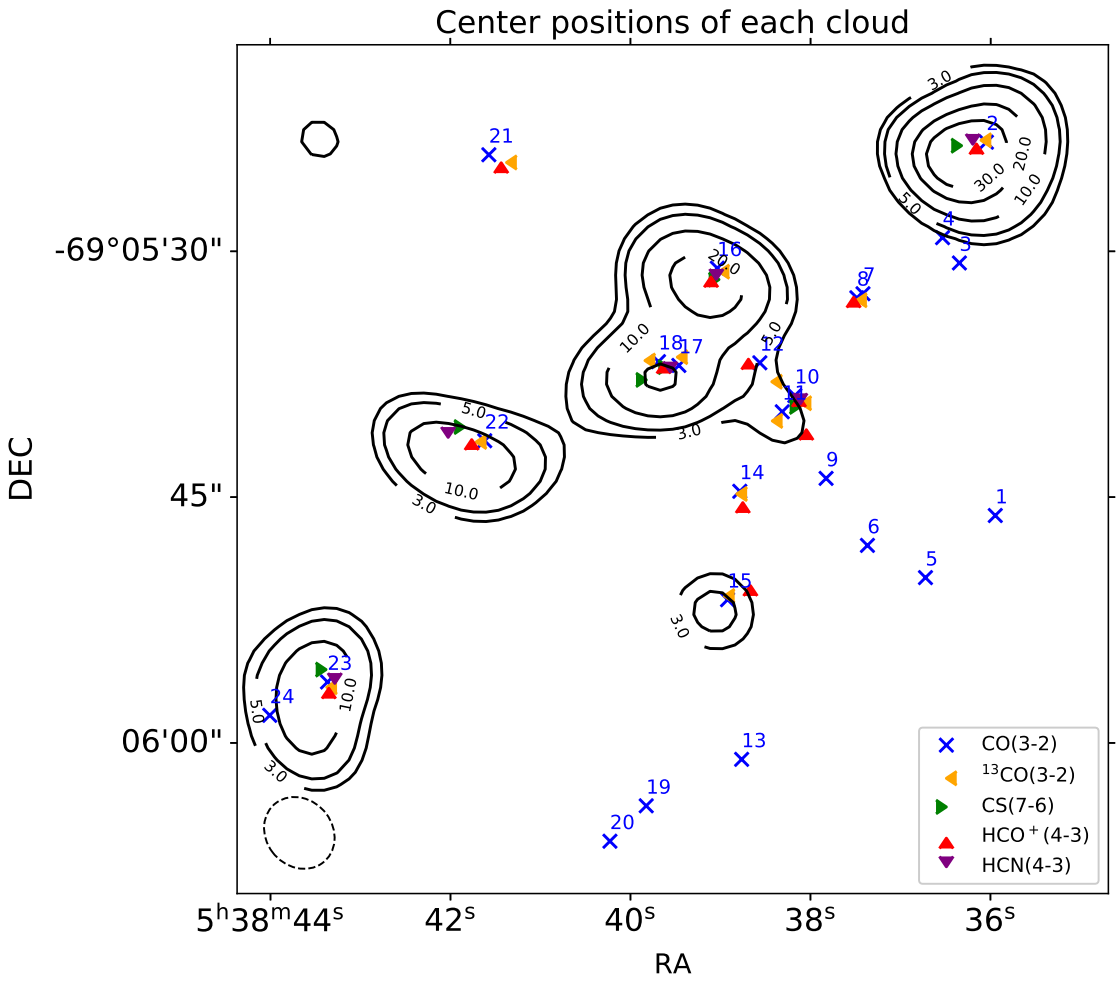

Figure 4.5: Central position of the clouds found in ^{12}CO(3-2), ^{13}CO(3-2), CS(7-6), HCO$^+$(4-3) and HCN(4-3) line observations of the vicinity of R136 in 30Dor. Contours correspond to 3, 5, 10, 20 and 30 times the rms of the image generated by integrating the ^{12}CO(3-2) line cube between 217 and 285 km s^{-1} (rms = 4.92 Jy beam^{-1} km s^{-1}). Blue crosses mark the central position of the clouds found in the ^{12}CO(3-2) in Section 4.1.1. Yellow arrowheads point towards the central position of ^{13}CO(3-2) clouds. Green arrowheads point towards the central position of CS(7-6) clouds. Red arrowheads point towards the central position of HCO$^+$(4-3) clouds. Purple arrowheads point towards the central position of HCN(4-3) clouds. The dashed ellipse in the lower left corner represents the beam size of the ^{12}CO(3-2) line cube.

northwest-southeast, these detections might indicate a trend in density, where the densest clouds are in this diagonal structure. However, density is not the only factor that affects CS and HCN emission (even though they are usually used to trace this property). Therefore, for a more complete evaluation, more tests need to be done using the results in this work. For example, running a non-LTE model with the intensities and line ratios as input can constrain the excitation temperature and density of these clouds.

4.2.2 Integrated line intensities

We determine the integrated line intensity $I = \int T_v \, \mathrm{d}v$ at the peak position of all the identified clouds in ^{12}CO(3-2) and the other molecules, ^{13}CO(3-2), CS(7-6), HCO$^+$(4-3) and HCN(4-3). To do this, we first obtain the spectra at the peak emission position for each molecule and each cloud. Then, we fit a Gaussian profile to the spectra using the `astropy.models.Gaussian1D` module. For clouds no. 8 and no. 18, which are clouds manually characterized in Section 4.1.1, the ^{13}CO(3-2), CS(7-6), HCO$^+$(4-3) spectra also contain two Gaussian components at different velocities, as they show emission from clouds no. 7 (in the case of cloud no. 8) and no. 17 (in the case of cloud no. 18) in the same lines of sight. Then, we integrate in velocity the best fit Gaussian profile to obtain the velocity integrated line intensity, $I = \int T_v \mathrm{d}v$, for each cloud and molecule. The obtained spectra for each molecule in each cloud, together with the best fit Gaussian models, are in Appendix B. Table 4.4 summarises the integrated line intensities for all the clouds identified in the mapped region.

Cloud no.	$I_{^{12}CO(3-2)}$ (K km s^{-1})	$I_{^{13}CO(3-2)}$ (K km s^{-1})	$I_{CS(7-6)}$ (K km s^{-1})	$I_{HCO^+(4-3)}$ (K km s^{-1})	$I_{HCN(4-3)}$ (K km s^{-1})
1	1.98 ± 0.20	-	-	-	-
2	125.12 ± 12.51	28.46 ± 2.85	1.91 ± 0.20	14.20 ± 1.42	3.13 ± 0.32
3	1.37 ± 0.15	-	-	-	-
5	1.13 ± 0.13	-	-	-	-
8	2.22 ± 0.24	0.56 ± 0.11	-	0.34 ± 0.08	-
9	0.69 ± 0.09	-	-	-	-
10	5.40 ± 0.54	0.85 ± 0.12	0.18 ± 0.05	1.02 ± 0.12	0.29 ± 0.06
11	5.57 ± 0.56	0.54 ± 0.11	-	0.35 ± 0.08	-
12	9.21 ± 0.92	0.95 ± 0.13	-	0.73 ± 0.10	-
13	3.06 ± 0.32	-	-	-	-
14	3.92 ± 0.40	0.73 ± 0.10	-	0.19 ± 0.06	-
15	16.82 ± 1.68	1.87 ± 0.21	-	2.04 ± 0.22	-
16	74.78 ± 7.48	12.26 ± 1.23	0.85 ± 0.10	7.36 ± 0.74	1.38 ± 0.15
17	56.48 ± 5.65	11.14 ± 1.12	0.79 ± 0.10	5.96 ± 0.60	1.29 ± 0.15
18	56.22 ± 5.62	9.08 ± 0.91	0.60 ± 0.09	-	-
19	1.99 ± 0.21	-	-	-	-
20	2.42 ± 0.26	-	-	-	-
21	1.06 ± 0.12	0.18 ± 0.07	-	0.18 ± 0.06	-
22	44.57 ± 4.46	6.31 ± 0.64	0.11 ± 0.06	1.22 ± 0.14	0.10 ± 0.06
23	46.36 ± 4.64	7.98 ± 0.80	0.39 ± 0.07	2.26 ± 0.24	0.36 ± 0.07

Table 4.4: Integrated line intensities $I = \int T_v \mathrm{d}v$ for each of the molecular species found in the molecular clouds at the T_{peak} position for each molecule, after fitting a Gaussian profile to each respective spectra.

To compare the peak intensities of the different molecules detected in the clouds, we determine the intensity line ratios with respect to the ^{13}CO(3-2) line intensity $\frac{I_{^{12}CO(3-2)}}{I_{^{13}CO(3-2)}}$, $\frac{I_{CS(7-6)}}{I_{^{13}CO(3-2)}}$, $\frac{I_{HCO^+(4-3)}}{I_{^{13}CO(3-2)}}$ and $\frac{I_{HCN(4-3)}}{I_{^{13}CO(3-2)}}$. The resulting line ratios are shown in Table 4.5, where we also include in the last column the $\frac{I_{HCO^+(4-3))}}{I_{HCN(4-3)}}$ line ratio. The $\frac{I_{^{12}CO(3-2)}}{I_{^{13}CO(3-2)}}$ ratio ranges between

3.94 and 10.30 for these clouds, with a median value of 6.10. The $\frac{I_{CS(7-6)}}{I_{^{13}CO(3-2)}}$ ratio range is typically between 0.02 and 0.07, with a median of 0.07, but cloud no. 10 shows a very different value with a ratio of 0.22, which is almost 10 times larger. The $\frac{I_{HCO^+(4-3)}}{I_{^{13}CO(3-2)}}$ ratio ranges between 0.26 and 1.20 for this sample, with a median value of 0.60. The $\frac{I_{HCN(4-3)}}{I_{^{13}CO(3-2)}}$ ratio lies between 0.02 and 0.34, with a median of 0.11. The $\frac{I_{HCO^+(4-3))}}{I_{HCN(4-3)}}$ ratio for this sample is between 3.51 and 12.22, with a median of 4.98. We will compare these values with line ratios found in other molecular clouds in the LMC in Section 4.5.3. We do not calculate the line ratios for cloud no. 21 because its ^{13}CO and HCO$^+$ detections have a low S/N ratio (≈ 4), which generates a higher uncertainty in their integrated intensities.

ID	$\frac{I_{^{12}CO(3-2)}}{I_{^{13}CO(3-2)}}$	$\frac{I_{CS(7-6)}}{I_{^{13}CO(3-2)}}$	$\frac{I_{HCO^+(4-3)}}{I_{^{13}CO(3-2)}}$	$\frac{I_{HCN(4-3)}}{I_{^{13}CO(3-2)}}$	$\frac{I_{HCO^+(4-3))}}{I_{HCN(4-3)}}$
2	4.40 ± 0.62	0.07 ± 0.01	0.50 ± 0.07	0.11 ± 0.02	4.54 ± 0.65
8	3.94 ± 0.70	-	0.60 ± 0.19	-	-
10	6.36 ± 0.98	0.22 ± 0.08	1.20 ± 0.21	0.34 ± 0.09	3.51 ± 0.69
11	10.30 ± 1.80	-	0.64 ± 0.21	-	-
12	9.66 ± 1.48	-	0.77 ± 0.15	-	-
14	5.37 ± 0.84	-	0.26 ± 0.10	-	-
15	8.98 ± 1.31	-	1.09 ± 0.17	-	-
16	6.10 ± 0.86	0.07 ± 0.01	0.60 ± 0.09	0.11 ± 0.02	5.33 ± 0.77
17	5.07 ± 0.72	0.07 ± 0.01	0.54 ± 0.08	0.12 ± 0.02	4.62 ± 0.68
18	6.19 ± 0.88	0.07 ± 0.01	-	-	-
22	7.06 ± 1.00	0.02 ± 0.01	0.19 ± 0.03	0.02 ± 0.01	12.22 ± 3.51
23	5.81 ± 0.82	0.05 ± 0.01	0.28 ± 0.04	0.04 ± 0.01	6.31 ± 1.14
Median	6.14	0.07	0.60	0.11	4.98
Standard deviation	1.95	0.06	0.31	0.11	2.87

Table 4.5: Intensity line ratios calculated from the intensity at the peak temperature position of each cloud in 30Dor, using the results shown in Table 4.4.

4.2.3 Molecular cloud luminosities in different molecular species

We calculate the luminosity of the molecular clouds in the ^{13}CO(3-2), CS(7-6), HCO$^+$(4-3) and HCN(4-3) molecular emissions where the ^{12}CO(3-2) cloud luminosity was obtained. For this, we apply the mask generated by CPROPS which indicates which voxel belongs to the ^{12}CO(3-2) cloud, in the ^{13}CO(3-2), CS(7-6), HCO$^+$(4-3) and HCN(4-3) line emission cubes. Then, for each of the clouds identified in Section 4.1.1, we sum the intensity in the corresponding voxels to the cloud assingment. We then transform from K km s^{-1} arcsec^2 to K km s^{-1} pc^2 using Equation 4.1. In this case, we do not correct for sensitivity bias as done for the ^{12}CO(3-2) luminosity. The resulting luminosities for each cloud in all the molecular species are presented in Table 4.6. The clouds in the northwest-southeast diagonal structure (clouds no. 2, 16, 17, 18, 22 and 23) present the highest luminosities in our sample, as it was for the peak intensities from Table 4.4.

We calculate the luminosity ratios with respect to the total ^{13}CO(3-2) luminosity $\frac{L_{^{12}CO(3-2)}}{L_{^{13}CO(3-2)}}$,

Cloud no.	$L_{^{12}CO(3-2)}$ (K km s^{-1} pc^2)	$L_{^{13}CO(3-2)}$ (K km s^{-1} pc^2)	$L_{CS(7-6)}$ (K km s^{-1} pc^2)	$L_{HCO^+(4-3)}$ (K km s^{-1} pc^2)	$L_{HCN(4-3)}$ (K km s^{-1} pc^2)
2	268.56 ± 22.11	58.43 ± 5.86	3.52 ± 0.39	49.37 ± 4.95	10.28 ± 1.05
8	1.78 ± 0.08	0.44 ± 0.11	-	0.34 ± 0.08	-
9	0.71 ± 0.10	0.12 ± 0.06	-	0.09 ± 0.04	-
10	6.20 ± 0.57	0.88 ± 0.15	0.14 ± 0.05	1.80 ± 0.21	0.35 ± 0.08
11	7.20 ± 0.59	0.37 ± 0.12	-	0.52 ± 0.11	-
12	10.41 ± 0.82	0.78 ± 0.16	-	1.16 ± 0.17	-
14	4.15 ± 0.41	0.69 ± 0.13	-	0.27 ± 0.08	-
15	22.64 ± 1.87	2.39 ± 0.30	-	4.45 ± 0.48	0.41 ± 0.09
16	216.18 ± 4.17	23.96 ± 2.41	1.24 ± 0.17	23.30 ± 2.34	3.70 ± 0.40
17	101.63 ± 3.43	9.77 ± 1.01	0.46 ± 0.10	8.28 ± 0.85	1.44 ± 0.18
18	66.91 ± 2.76	7.19 ± 0.76	0.17 ± 0.06	7.16 ± 0.74	0.82 ± 0.13
21	1.32 ± 0.12	0.15 ± 0.07	-	0.25 ± 0.07	-
22	107.24 ± 8.92	14.62 ± 1.49	0.08 ± 0.05	5.03 ± 0.54	0.07 ± 0.04
23	112.54 ± 9.15	17.69 ± 1.79	0.66 ± 0.13	7.88 ± 0.82	1.05 ± 0.16

Table 4.6: Luminosities of the ^{12}CO(3-2), ^{13}CO(3-2), CS(7-6), HCO$^+$(4-3) and HCN(4-3) molecular emission in each molecular cloud. The $L_{^{12}CO(3-2)}$ luminosities are the same as the ones presented in Table 4.1.

$\frac{L_{CS(7-6)}}{L_{^{13}CO(3-2)}}$, $\frac{L_{HCO^+(4-3)}}{L_{^{13}CO(3-2)}}$ and $\frac{L_{HCN(4-3)}}{L_{^{13}CO(3-2)}}$. We also calculate the ratio $\frac{L_{HCO^+(4-3)}}{L_{HCN(4-3)}}$ for every cloud detected in these two molecules. The line ratios obtained for each cloud are in Table 4.7. These line ratios give us the global average of the line ratios over the size of each cloud, complementing the information obtained from the peak line ratios determined in Section 4.2.2. We do not calculate the line ratios for clouds no. 9 and 21, as well as the $\frac{L_{CS(7-6)}}{L_{^{13}CO(3-2)}}$ and $\frac{L_{HCN(4-3)}}{L_{^{13}CO(3-2)}}$ ratios for cloud no. 22, because these clouds have very low S/N (between $3-4$) detections, so their line ratios have a high uncertainty.

The $\frac{L_{^{12}CO(3-2)}}{L_{^{13}CO(3-2)}}$ values ranges from 4 to 19. In general all the clouds show $\frac{L_{CS(7-6)}}{L_{^{13}CO(3-2)}}$ ratio are between 0.02 to 0.06, $\frac{L_{HCO^+(4-3)}}{L_{^{13}CO(3-2)}}$ between 0.4 to 1.86 and $\frac{L_{HCN(4-3)}}{L_{^{13}CO(3-2)}}$ between 0.06 to 0.18, except cloud no. 10 which deviates from these range, showing larger ratios of 0.16, 2.04 and 0.40 for each line ratio respectively.

The molecular line ratios $\frac{L_{CS(7-6)}}{L_{^{13}CO(3-2)}}$, $\frac{L_{HCN(4-3)}}{L_{^{13}CO(3-2)}}$ and $\frac{L_{HCO^+(4-3)}}{L_{HCN(4-3)}}$ for each cloud in Table 4.7 have similar values to the line ratios values in the peak temperature positions of Table 4.5. Two clouds, cloud no. 2 and cloud no. 18, show a different behaviour. Cloud no. 2 has a $\frac{L_{HCN(4-3)}}{L_{^{13}CO(3-2)}} > \frac{I_{HCN(4-3)}}{I_{^{13}CO(3-2)}}$, while cloud no. 18 has $\frac{L_{CS(7-6)}}{L_{^{13}CO(3-2)}} < \frac{I_{CS(7-6)}}{I_{^{13}CO(3-2)}}$.

The $\frac{L_{^{12}CO(3-2)}}{L_{^{13}CO(3-2)}}$ ratios in the central part of the map (for clouds no. 11, 12, 16, 17 and 18) are larger than the line ratios found at their peak temperature positions $\frac{I_{^{12}CO(3-2)}}{I_{^{13}CO(3-2)}}$. This reflects that the intensity of the ^{13}CO(3-2) line falls more rapidly than the ^{12}CO(3-2) line intensity toward the borders of the cloud area. The inequality $\frac{L_{^{12}CO(3-2)}}{L_{^{13}CO(3-2)}} > \frac{I_{^{12}CO(3-2)}}{I_{^{13}CO(3-2)}}$ can be

Cloud no.	$\frac{L_{^{12}CO(3-2)}}{L_{^{13}CO(3-2)}}$	$\frac{L_{CS(7-6)}}{L_{^{13}CO(3-2)}}$	$\frac{L_{HCO^+(4-3)}}{L_{^{13}CO(3-2)}}$	$\frac{L_{HCN(4-3)}}{L_{^{13}CO(3-2)}}$	$\frac{L_{HCO^+(4-3)}}{L_{HCN(4-3)}}$
2	4.60 ± 0.60	0.06 ± 0.01	0.84 ± 0.12	0.18 ± 0.03	4.80 ± 0.69
8	4.01 ± 1.02	-	0.76 ± 0.27	-	-
10	7.03 ± 1.37	0.16 ± 0.07	2.04 ± 0.43	0.40 ± 0.11	5.15 ± 1.31
11	19.21 ± 6.37	-	1.39 ± 0.54	-	-
12	13.34 ± 2.88	-	1.49 ± 0.37	-	-
14	6.00 ± 1.26	-	0.40 ± 0.13	-	-
15	9.48 ± 1.43	-	1.86 ± 0.31	0.17 ± 0.04	10.80 ± 2.64
16	9.02 ± 0.92	0.05 ± 0.01	0.97 ± 0.14	0.15 ± 0.02	6.30 ± 0.93
17	10.40 ± 1.13	0.05 ± 0.01	0.85 ± 0.12	0.15 ± 0.02	5.76 ± 0.94
18	9.30 ± 1.05	0.02 ± 0.01	0.99 ± 0.15	0.11 ± 0.02	8.73 ± 1.63
22	7.34 ± 0.97	-	0.34 ± 0.05	-	-
23	6.36 ± 0.83	0.04 ± 0.01	0.45 ± 0.06	0.06 ± 0.01	7.53 ± 1.38

Table 4.7: Molecular line ratios obtained from the luminosities in ^{13}CO(3-2), ^{12}CO(3-2), CS(7-6), HCO$^+$(4-3) and HCN(4-3) of each cloud in Table 4.6 for each ^{12}CO(3-2) molecular cloud.

explained as a selective photodissociation of ^{13}CO at the outer layers of the cloud (Visser et al. 2009) if one assumes that the line ratio resembles the ^{12}CO/^{13}CO abundance ratio. This effect has been used to explain why the ^{12}CO(3-2) luminosity line ratio increases towards the borders of the molecular clouds found in N11 (Celis Peña et al. 2019). Although the other clouds also show a $\frac{L_{^{12}CO(3-2)}}{L_{^{13}CO(3-2)}} > \frac{I_{^{12}CO(3-2)}}{I_{^{13}CO(3-2)}}$, the result is not statistically significant given the line ratio uncertainties.

In the case of the $\frac{L_{HCO^+(4-3)}}{L_{^{13}CO(3-2)}}$ ratios, these are larger than those found the peak position $\frac{I_{HCO^+(4-3)}}{I_{^{13}CO(3-2)}}$ for the clouds in the northwest-southeast diagonal structure (clouds no. 2, 10, 12, 17 and 23) and cloud no. 15. In the other clouds with HCO$^+$(4-3) detections, the $\frac{L_{HCO^+(4-3)}}{L_{^{13}CO(3-2)}} > \frac{I_{HCO^+(4-3)}}{I_{^{13}CO(3-2)}}$, but these larger luminosity ratios given the line ratio uncertainties are not statistically significant. Further investigation on the line ratios of these clouds are required to understand this difference.

4.2.4 Physical properties derived from ^{13}CO(3-2) molecular emission

For the first time, we have simultaneous high resolution ^{12}CO(3-2) and ^{13}CO(3-2) molecular line emissions towards the molecular gas near R136 in 30 Doradus. This allows us to determine the excitation temperature and calculate the column density $N(H_2)$ of the these clouds. To obtain the column density of H_2 molecules $N(H_2)$ for the peak positions of the clouds, under LTE conditions, we use the method shown in Section 1.2.3.4.

First we assume that the excitation temperature for ^{13}CO(3-2) is the same than for ^{12}CO(3-2). Thus we obtain the excitation temperature $T_{ex}(^{12}CO(3-2)) = T_{ex}$ for the ^{12}CO(3-2) molecular transition, in K, using Equation 1.19 replacing $\nu = 345.796$ GHz (the rest frequency

of the ^{12}CO(3-2) line):

$$T_{ex} = \frac{16.59}{\ln(1 + \frac{16.59}{T_{peak}+0.036})} \tag{4.3}$$

where T_{peak} is the ^{12}CO(3-2) peak temperature of the cloud in K. We use the T_{peak} values in Table 4.1 for each cloud where we detect ^{13}CO(3-2) emission. Note that equation 4.3 assumes a beam filling factor of 1, which might not be true for unresolved clouds. We discuss the effect of this assumption further in Section 4.5.3.

Then, we determine the column density of ^{13}CO, $N(^{13}CO)$. To calculate this column density, the ^{13}CO(3-2) emission has to be optically thin, which means that the optical depth of the ^{13}CO(3-2) line $\tau^{13CO} \ll 1$. To confirm that we are in the optically thin regime, we calculate τ^{13CO} using the following formula:

$$\tau^{13CO} = -\ln(1 - \frac{0.063\, T_{peak}^{13CO}}{(\mathrm{e}^{\frac{15.85}{T_{ex}(3-2)}} - 1)^{-1} - 0.003}), \tag{4.4}$$

where T_{peak}^{13CO} is the ^{13}CO(3-2) peak temperature for the cloud in K. The resulting τ^{13CO} are all lower than 1, between 0.1 to 0.4, and are given in Table 4.8. We confirm that emission in is optically thin in all the molecular clouds.

We calculate the ^{13}CO column density $N(^{13}CO)$ in cm^{-2} using Equation 1.20, where $I_{^{13}CO(3-2)}$ is the integrated line intensity at the peak temperature position, obtained from Table 4.4.

Finally, we obtain the column density of H_2 molecules $N(H_2)$ as $N(H_2) = [H_2/^{13}CO]N(^{13}CO)$, where $[H_2/^{13}CO]$ is the abundance ratio between H_2 and ^{13}CO, which we assume to be 1.8×10^6 (Garay et al. 2002; Heikkilä et al. 1999). The obtained T_{ex}, τ^{13CO}, $N(^{13}CO)$ and $N(H_2)$ are in Table 4.8.

The molecular clouds have excitation temperatures T_{ex} ranging from 5.38 to 33.39. The highest temperatures are found in the brightest clouds, no. 2, 16, 17, 18, 22 and 23, belonging to the northwest-southeast structure. These clouds have been detected in HCO$^+$(4-3), CS(7-6) and/or HCN(4-3), so they have a high density ($n \sim 10^6$ cm^{-3}) and thus, one could assume that the derived $T_{ex} \approx T_K$, is the kinetic temperature of the clouds. Their peak column densities range between $4.2 - 23.7 \times 10^{21}$ cm^{-2}. Those clouds with column densities exceeding $\times 10^{22}$ cm^{-2}, clouds no. 2, 8, 16, 17 and 18, are those with the strongest CO emission. In this work, we only calculate the peak excitation temperatures and column densities of each cloud.

4.3 Submillimeter Emission towards R136

From the imaging process described in Section 2.2, we obtain a continuum image at 880 μm with a resolution of 4.7" $\times$ 3.9" (PA = 69 degrees) and an rms of 4 mJy/beam. This 880 μm continuum image is shown in Figure 4.6. Emission is present in the region near R136 and shows a similar pattern as the ^{12}CO(3-2) molecular line emission. At first sight, there are continuum emission clouds concentrated along the diagonal in northwest-southeast direction

	T_{ex} (K)	τ^{13CO}	$N(^{13}CO)$ ($\times 10^{14}$ cm^{-2})	$N(H_2)$ ($\times 10^{21}$ cm^{-2})
2	33.39 ± 0.06	0.375 ± 0.002	131.90 ± 13.20	23.74 ± 2.38
8	5.38 ± 0.33	0.417 ± 0.080	70.79 ± 14.14	12.74 ± 2.55
10	7.11 ± 0.19	0.292 ± 0.033	31.45 ± 4.36	5.66 ± 0.78
11	6.38 ± 0.23	0.118 ± 0.039	30.61 ± 6.23	5.51 ± 1.12
12	7.61 ± 0.17	0.151 ± 0.025	27.91 ± 3.80	5.02 ± 0.68
14	6.76 ± 0.21	0.301 ± 0.037	32.75 ± 4.69	5.89 ± 0.84
15	10.45 ± 0.12	0.174 ± 0.013	23.32 ± 2.63	4.20 ± 0.47
16	32.76 ± 0.06	0.229 ± 0.002	56.81 ± 5.70	10.23 ± 1.03
17	16.13 ± 0.08	0.245 ± 0.006	71.08 ± 7.15	12.80 ± 1.29
18	15.07 ± 0.09	0.147 ± 0.007	62.42 ± 6.29	11.23 ± 1.13
22	20.37 ± 0.07	0.198 ± 0.004	33.35 ± 3.37	6.00 ± 0.61
23	18.60 ± 0.08	0.284 ± 0.005	44.83 ± 4.52	8.07 ± 0.81

Table 4.8: Excitation temperatures, ^{13}CO(3-2) optical depths, ^{13}CO column densities and H_2 column densities for the peak temperature position of each molecular cloud from Section 4.1 which has a ^{13}CO(3-2) detection. We assume the excitation temperature for the ^{12}CO(3-2) and ^{13}CO(3-2) lines are the same so as to calculate the optical depth. We assume an abundance ratio $[H_2/^{13}CO] = 1.8 \times 10^6$ to go from $N(^{13}CO)$ to $N(H_2)$.

and at least, one continuum cloud is seen at the south part of the image. Emission is brightest in the northwest corner of the image and becomes less bright towards the southeast.

In this section, we describe the emission present in the ALMA 880 μm continuum image: we detect individual sources in continuum emission, obtain their sizes and fluxes, and calculate the total gas mass from dust emission near R136.

4.3.1 Cloud identification

We identify clouds in the ALMA 880 μm continuum image through visual inspection. We consider emission over 3σ in the continuum image as a detection, where $\sigma = 4$ mJy/beam is the rms of the ALMA 880 μm continuum image. Using this criterion, we identify 6 sources in the continuum image, which we name A, B, C, D, E and F, naming them in ascending right ascension. Two of these sources, B and D, are close enough to each other so that their emissions share the same 3σ contour. All of these sources coincide with one or more ^{12}CO(3-2) clouds from Section 4.1: source A coincides with cloud no. 2, source B with cloud no. 16, source C with cloud no.15, source D with clouds no. 17 and no. 18, source E with cloud no. 22 and source F with cloud no. 23. We refer to these continuum sources as clouds from now on.

We obtain the areas and radii of each of the detected clouds. We define the area of a cloud in the 880 μm continuum image as the area inside the 1.5σ contour of each detected source. These contours, together with the 3, 4 and 5σ contours are shown in Figure 4.6. There are other 1.5σ contours that do not contain emission over 3σ within them. We do not consider these emissions as clouds as their S/N is lower than 3, so their calculated parameters would

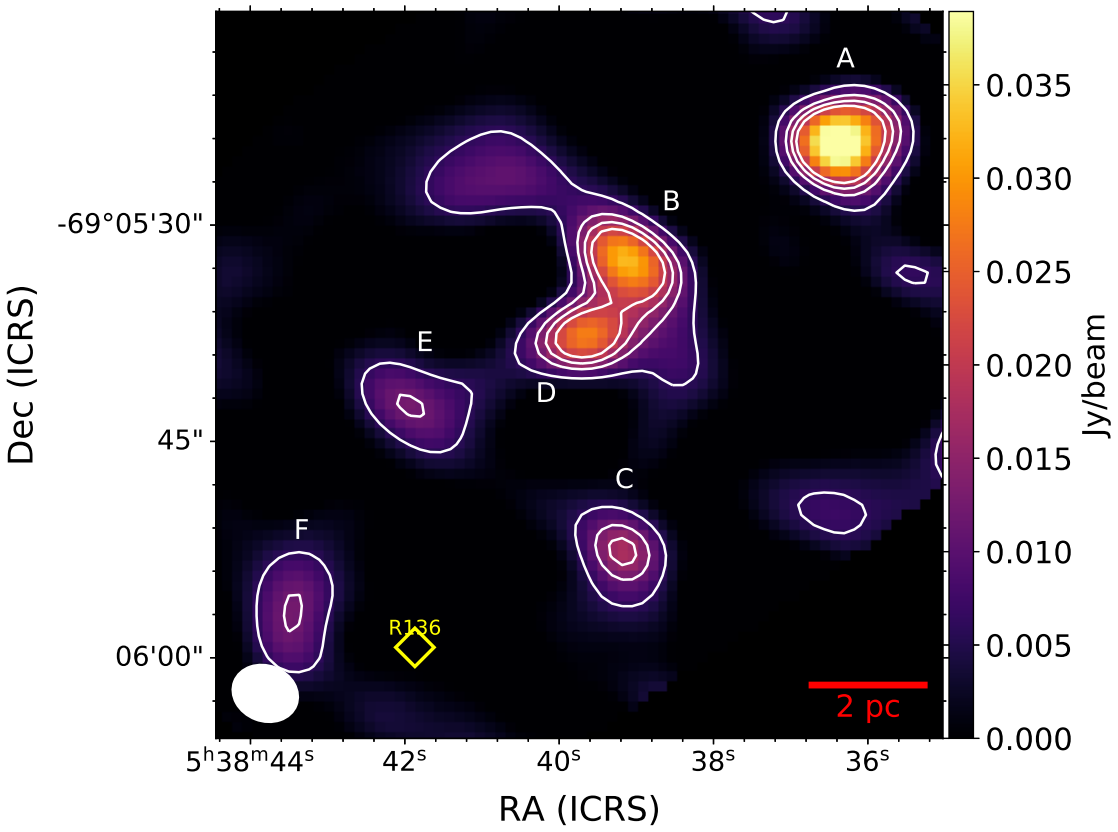

Figure 4.6: ALMA 880 μm continuum image of the vicinity of R136. White contours represent 1.5, 3, 4 and 5 σ levels ($\sigma = 4$ mJy/beam), with labels indicating the contours that correspond to clouds A, B, C, D, E and F. The white ellipse in the lower left corner represents the beam size. The scalebar in the lower right corner represents a 2 pc length.

have significant uncertainties.

Then, we calculate the area of the cloud as:

$$A = N_{pix} \mathrm{d}_{pix}^2, \tag{4.5}$$

where N_{pix} is the number of pixels inside the 1.5σ contour of the cloud and d_{pix} is the diameter of a pixel in pc. To determine the area of clouds B and D, we model the emission from the pixels in both clouds as two elliptical Gaussians, because their emission is blended up to a 5σ level. We use the `astropy.modelling` package to find the best fit for each source. Afterwards, we generate an image where one of the elliptical Gaussians is subtracted and find the area of the cloud which is not subtracted using the resulting image.

We calculate the equivalent radii R_{eq} of the clouds assuming that the cloud has a spherical shape, using Equation 1.1. We also calculate the deconvolved equivalent radii:

$$R_{eq,\mathrm{dc}} = \sqrt{R_{eq}^2 - R_{beam}^2}, \tag{4.6}$$

where R_{beam} is the geometric mean of the radii along the major and minor axes of the beam. This formula is equivalent to Equation 3.4 when applied to a circular cloud. For the ALMA

880 μm continuum image, the beam radii is $R_{beam} = 0.84$ pc. If the equivalent radii of a cloud is smaller than R_{beam}, we adopt $R_{eq,\mathrm{dc}} = R_{beam}$ as an upper limit to the deconvolved radius. The resulting areas and equivalent radii (deconvolved and not deconvolved) for the clouds in the continuum image are in Table 4.9.

Sources	Area (pc^2)	R_{eq} (pc)	$R_{eq,\mathrm{dc}}$ (pc)
A	3.60	1.07 ± 0.13	0.66 ± 0.11
B	3.69	1.08 ± 0.19	0.69 ± 0.15
C	1.96	0.79 ± 0.25	$< 0.84 \pm 0.16$
D	2.76	0.94 ± 0.19	0.42 ± 0.14
E	1.96	0.79 ± 0.35	$< 0.84 \pm 0.22$
F	2.13	0.82 ± 0.37	$< 0.84 \pm 0.25$

Table 4.9: Areas and equivalent radii of the clouds found in the ALMA 880 μm image.

4.3.2 Flux measurements

We determine the total flux coming from the clouds found in the ALMA 880 μm continuum image using aperture photometry with background sky subtraction. The aperture of each cloud is a circle that encloses the area found in Section 4.3.1 (the 1.5σ contour). The radii of each aperture is listed in Table 4.10. The background emission flux is obtained by taking the median intensity at a sample of apertures with a radius of 5", which do not present emission in the ALMA 880 μm continuum. This median is then multiplied by the aperture area of each cloud to determine the background emission. The flux density of each source is the flux present inside the aperture minus the background emission. The uncertainties in the fluxes are the photometric errors inside the aperture area, calculated using Equation 3.1 with $\sigma = 4$ mJy beam $^{-1}$. To obtain the flux coming from sources B and D, we model the emission as two Gaussians and subtract one of the sources when measuring the flux of the other, so as to not include flux from one cloud in the total flux of the other.

The central positions of the aperture (right ascension α_{ctr} in hh:mm:ss.s and declination δ_{ctr} in dd:mm:ss.s), aperture radius r_{ap} in arcseconds and total flux in the continuum image S_{880} in mJy for each cloud are in Table 4.10.

4.3.3 Free-Free Emission near R136

The flux measurement from the ALMA 880 μm continuum image can contain emission of different physical processes: thermal dust continuum emission, free-free (bremsstrahlung) emission from ionized gas, contribution from molecular lines in the passband (in this case, ^{12}CO(3-2)) and synchrotron emission from relativistic particles. We are interested in the dust continuum emission, therefore we need to calculate and remove the other contributions to the measured flux. The ^{12}CO(3-2) line is removed from the continuum image during the imaging process (see Sect. 2.2). Synchrotron emission is negligible in 30 Doradus (Brunetti & Wilson 2019; Guzmán 2010). However, we expect the ALMA 880 μm continuum image to have an important contribution from free-free emission, as the clouds are within an HII region. We determine the free-free emission in the vicinity of R136 in two different ways, using a Brγ emission image and a radio continuum image.

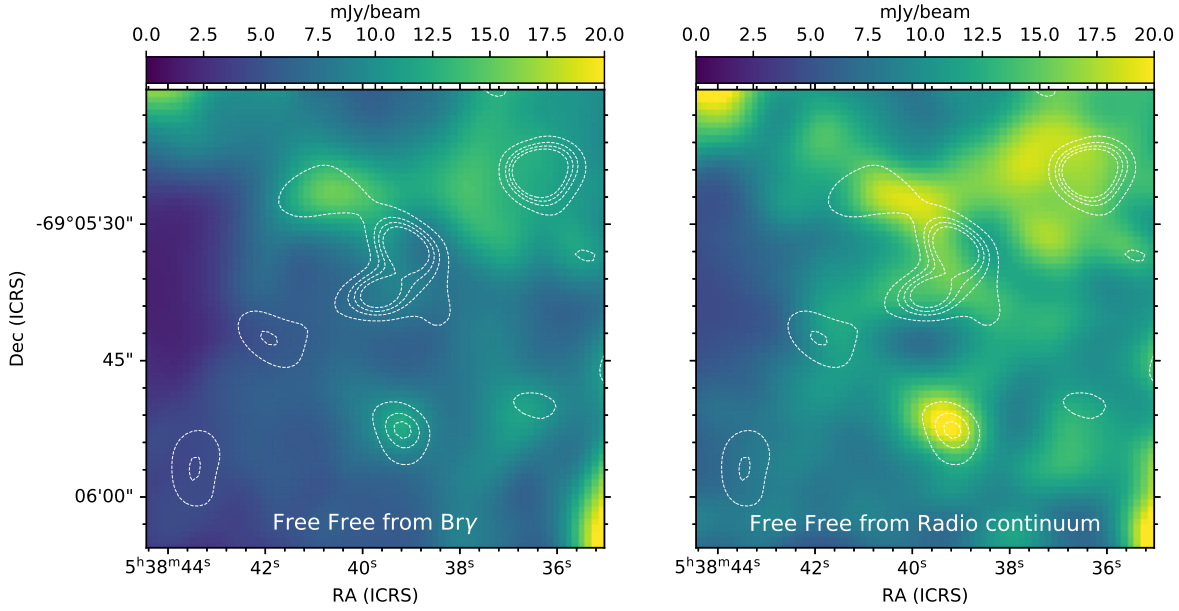

Figure 4.7: Free-free emission images generated from Brγ emission (left) and Radio continuum emission (right). The white dashed contours are the same contours as in Figure 4.6.

We obtain a free-free emission image using the Brγ line emission image obtained with the 1.5 m telescope in Cerro Tololo Observatory (M. Rubio, priv. comm.), with a resolution of 1.2" and a pixel size of 0.4". This image has intensity units of erg cm^{-2} s^{-1} sr^{-1}. We first transform the Brγ emission image into an Hα line image. To do this, we use the ratio between Hα and Brγ intensities of 101.78 for a typical HII region with an electronic temperature $T_{\rm e} = 10^4$ and electron density of 100 cm^{-3} (Osterbrock & Ferland 2006) and convert the Brγ image to an Hα image. Then, we transform the Hα image intensity I_α in erg cm^{-2} s^{-1} sr^{-1} to a free-free emission image I_ν^{ff} in mJy sr^{-1}, using :

$$I_\nu^{ff} = 1.16\Big(1 + \frac{n(\mathrm{He}^+)}{n(\mathrm{H}^+)}\Big)\Big(\frac{T_{\rm e}}{10^4}\Big)^{0.62}\nu^{-0.1}\Big(\frac{I_\alpha}{10^{-12}}\Big) \tag{4.7}$$

(derived from Hunt et al. 2004) which is Equation 1.36 divided by the solid angle in sr. We use $\nu = 338.5$ GHz, the frequency of our ALMA continuum image. We use $T_{\rm e} = 10^4$ K and $n(He^+)/n(H^+) \sim 0.08$, which is a typical value estimated for low metallicity sources like the Magellanic Clouds (Hunt et al. 2004). We convolve the image to the same resolution of 4.7"$\times$3.9" as the ALMA 880 μm continuum image and transform the image units from mJy/sr to mJy/beam by multiplying each pixel by the area of the beam in sr. The resulting free-free emission image is shown in the left panel of Figure 4.7 and has an rms of 4.5 mJy/beam.

We obtain a second free-free emission image using the 6 cm (4.8 GHz) image from Dickel et al. (2005) taken with the Australia Telescope Compact Array (ATCA). This image has a resolution of 3.16" $\times$ 2.29" and a pixel size of 2" and intensity units of Jy/beam. We assume that emission at 6 cm does not contain synchrotron emission. This assumption is safe as there is no considerable synchrotron emission in this region (Brunetti & Wilson 2019). We extrapolate the ATCA image from 6 cm to 880 μm (338.5 GHz) adopting the free-free power

law in the optically thin regime (from Equation 1.33):

$$S_{ff}(338.5GHz) = \left(\frac{338.5GHz}{4.8GHz}\right)^{-0.1} S_{ff}(4.8GHz) \tag{4.8}$$

where $S_{ff}(338.5GHz)$ is the resulting free-free emission intensity in Jy/beam and $S_{ff}(4.8GHz)$ is the intensity present in the 6 cm radio continuum image in Jy/beam. Lastly, we convolve the resulting free-free image to the same resolution as the ALMA 880 μm continuum image. This free-free emission image has an rms of 6.9 mJy/beam. The resulting free-free emission image is shown in the right panel of Figure 4.7.

Comparing both images in Figure 4.7, we can see that the free-free emission calculated from Radio continuum shows the same morphology as the free-free emission calculated using Brγ, but the one from radio continuum show stronger free-free emission than the one from Brγ. Both show extended free-free emission towards the northwest corner of the image and one free-free source towards continuum cloud C, better seen in the free-free image from Radio continuum.

We determine the free-free emisssion towards the 880 μm sources from both free-free images. We use the same apertures and aperture positions from Section 4.3.2. The obtained free-free fluxes, $S_{ff,Br\gamma}$ from free-free derived from Brγ and $S_{ff,radio}$ from free-free obtained from Radio continuum emission, are summarized in Table 4.10. The free-free fluxes determined using both images are almost the same within the errors, but the free-free flux obtained from Radio continuum is between $1.4-2$ times larger than the free-free flux from Brγ emission. The measured free-free fluxes represent between 50 and 85% of the total 880 μm flux measured in the ALMA images, confirming that the free-free contribution to the continuum is high, as expected in an HII region. Cloud C presents the largest free-free contribution with respect to the total 880 μm emission. In Figure 4.7, there is a free-free emission source in the location of cloud C, which explains why the free-free emission contribution to the total flux is so important.

We choose to estimate the dust flux density subtracting $S_{ff,Br\gamma}$ from the flux density in the 880 μm continuum image S_{880} as the uncertainties tend to be lower. This is a direct result of the smaller rms in the free-free image derived from Brγ emission in comparison with the free-free emission image obtained from Radio continuum emission. The resultant dust flux density S_{dust} is in the last column of Table 4.10.

4.3.4 Gas mass from dust emission

We calculate the total gas masses of the molecular clouds near R136 using the dust fluxes obtained in Section 4.3.3. We use Equation 1.16 with $D = 1.55 \times 10^{23}$ cm (50 kpc). To express the total mass in solar masses we divide by mass of the Sun $M_\odot = 1.9 \times 10^{33}$ gr. This equation is obtained considering dust emission is optically thin.

We calculate the gas masses from dust emission using the dust fluxes S_{dust} from Table 4.10. We use a dust temperature $T_d = 25$ K, as the area close to R136 in 30 Doradus has temperatures $\sim 24-26$ K (Planck Collaboration et al. 2011). We note that this assumption is very general, as Planck data resolution is around 5'.

Sources	RA (FK5)	DEC (FK5)	r_{ap} (")	S_{880} (mJy)	$S_{ff,Br\gamma}$ (mJy)	$S_{ff,\mathrm{radio}}$ (mJy)	S_{dust} (mJy)
A	5:38:36.3	-69:05:24.3	4.9	61.2 ± 7.7	32.2 ± 9.6	36.2 ± 13.4	29.0 ± 17.2
B	5:38:39.1	-69:05:32.6	6.0	49.1 ± 9.4	37.5 ± 11.7	47.4 ± 16.4	11.6 ± 21.1
C	5:38:39.2	-69:05:52.7	3.9	19.3 ± 6.1	16.5 ± 7.6	24.4 ± 10.7	2.9 ± 13.7
D	5:38:39.7	-69:05:37.8	5.3	32.9 ± 8.3	22.1 ± 10.4	30.6 ± 14.5	10.7 ± 18.7
E	5:38:41.9	-69:05:42.5	4.2	17.6 ± 6.6	7.3 ± 8.2	11.8 ± 11.5	10.4 ± 14.8
F	5:38:43.4	-69:05:57.0	4.3	18.6 ± 6.7	4.9 ± 8.4	5.2 ± 11.8	13.8 ± 15.1

Table 4.10: Results of the aperture photometry in the ALMA 880 μm continuum image, the free-free images obtained in Section 4.3.3 and in the dust images generated by subtracting the free-free images. RA and DEC are the right ascension and declination of the aperture center, and r_{ap} is the aperture radii. S_{880} is the flux obtained from the ALMA continuum image. $S_{ff,Br\gamma}$ and $S_{ff,\mathrm{radio}}$ are the fluxes obtained from the free-free images done with Brγ emission and radio continuum emission, respectively. $S_{\mathrm{d}ust}$ dust fluxes obtained by subtracting $S_{880} - S_{ff,Br\gamma}$.

Source	M_{gas} ($\mathrm{M}_\odot$)
A	1353 ± 803
B	541 ± 985
C	135 ± 639
D	499 ± 873
E	485 ± 691
F	644 ± 705

Table 4.11: Gas masses obtained from dust emission using Equation 1.16. M_{gas} and correspond to the gas masses obtained from dust fluxes $S_{\mathrm{d}ust}$ from Table 4.10.

To obtain the emissivity of dust per H atom ε_H at 338.5 GHz, we use Equation 1.14. We assume the dust grain properties in 30 Dor are similar to the ones present in the molecular ring of the Milky Way, so that we can use the dust absorption coefficient $\kappa(870\mu m) = 1.26 \pm 0.02$ cm^2 g^{-1} found by Bot et al. (2010a). Just for completeness, we transform $\kappa(870\mu m)$ to $\kappa(880\mu m)$, using Equation 1.28 with a dust emissivity index $\beta = 2$. This gives $\kappa(880\mu m) = 1.23 \pm 0.02$ cm^2 g^{-1}. Assuming the dust to gas ratio scales linearly with metallicity and using $Z(LMC) = 0.5Z(\odot)$ (Rolleston et al. 2002), the dust to gas ratio in the LMC is half the dust to gas ratio in the Solar neighborhood, $x_{\mathrm{d}}(LMC) = 0.5x_{\mathrm{d}}(\odot) = 3.5 \times 10^{-3}$. Using these values of $\kappa(880\mu m)$ and x_{d}, the resulting dust emissivity per H atom is $\varepsilon_H(880\mu m) = (9.8 \pm 0.2) \times 10^{-27}$ cm^2. This value is used in Equation 1.16 to derive the gas masses.

The gas masses obtained from Equation 1.16 are in Table 4.11. All masses are within 10^2 and 10^3 $\mathrm{M}_\odot$, the same orders of magnitude as the virial masses obtained in Section 4.1.2 for the clouds in the northwest-southeast diagonal structure.

4.4 Comparison between molecular and continuum emission near R136

The molecular clouds contain molecular gas and dust. In this work, the molecular gas in R136 has been studied by the emission of ^{12}CO(3-2) line and the dust emission by the sub-millimeter 880 μm continuum emission, both of which have similar resolution (4.7" $\times$ 3.9" for the continuum image and 4.6" $\times$ 4.0" for the ^{12}CO(3-2) molecular line cube). Therefore, we can make a comparison of some properties derived from both components assuming that the dust continuum emission is associated to the molecular cloud. First, in Section 4.4.1, we determine the size of the ^{12}CO(3-2) clouds and compare it to the size of the dust clouds. Then, in Section 4.4.2, we determine the ^{12}CO(3-2) emission in the same area covered by 880 μm continuum emission, obtain the gas masses for each cloud and compare the obtained gas masses from molecular gas with total gas masses obtained using dust emission.

4.4.1 Extensions of CO and continuum emission

We use the areas of the dust clouds given in Table 4.9 for this comparison.

To determine the area of the ^{12}CO(3-2) clouds, we make velocity integrated images for each cloud, integrating in the velocity range in which emission is detected. The velocity range used for the integration is $[v - 2\sigma_v, v + 2\sigma_v]$ for each cloud, where v and σ_v correspond to the central velocity and velocity dispersion of the cloud given in Table 4.1. This range contains 95.4% of the total emission from the cloud, assuming emission follows a Gaussian distribution in velocity. We determine the rms for the velocity integrated image for each cloud and define the extension of the cloud as the area enclosed by the 3σ contour. The velocity ranges used for integration in km s^{-1}, the resulting rms of the velocity integrated image in Jy beam^{-1} km s^{-1} and the calculated areas in pc^2 are in Table 4.12.

In the specific case of the dust sources B and D, we had to apply a different method to determine the ^{12}CO counterpart source's size as we know that the ^{12}CO emission has three different clouds, no. 16, 17 and 18, separated in velocity but in the same line of sight. Thus, we integrated the ^{12}CO(3-2) line cube between 238 and 249 km s^{-1} and determine the area enclosed in the 3σ rms contour of the resulting image. For reference, we also calculate the area shared by sources B and D in the 880 μm continuum image. This area corresponds to $A = 6.16$ pc^2.

Figure 4.8 shows the ^{12}CO(3-2) velocity integrated images in the velocity ranges of each cloud with the 3, 5 and 10σ contours shown in color red. Superimposed to each integrated velocity image we show in color white the ALMA 880 μm 1.5 and 3σ continuum contours (which correspond to the white contours in Figure 4.6). We see that in all the identified clouds the ^{12}CO(3-2) clouds are larger in size that the associated dust cloud as the ^{12}CO(3-2) velocity integrated images 3σ contours cover a larger area than the ALMA 880 dust μm continuum image 1.5σ contour. Also, the calculated areas for the^{12}CO(3-2) clouds in Table 4.12 are larger than the areas from the corresponding 880 μm continuum sources in Table 4.9.

It is interesting to see that clouds no. 2, 15, 16, 17 and 18 ^{12}CO(3-2) sizes obtained through

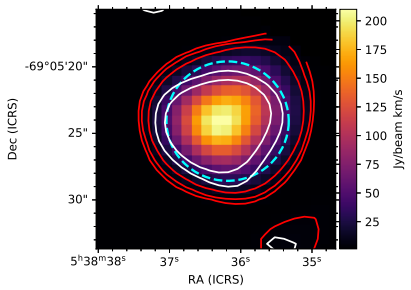

(a) Cloud no. 2 velocity integrated image, between 246.6 and 253.8 km s^{-1} (σ = 1.3 mJy beam^{-1} km s^{-1}), with continuum source A contours in white.

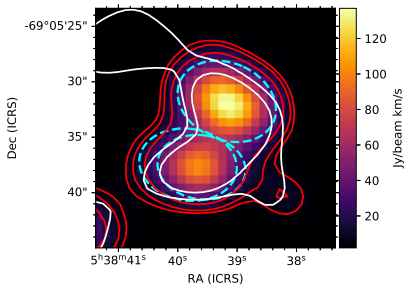

(b) Clouds no. 16, 17 and 18 velocity integrated image, between 238.0 and 249.0 km s^{-1} (σ = 2.0 mJy beam^{-1} km s^{-1}), with continuum sources B and D contours in white.

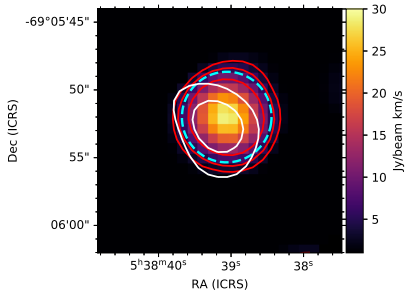

(c) Cloud no. 15 velocity integrated image, between 244.4 and 250.6 km s^{-1} (σ = 1.0 mJy beam^{-1} km s^{-1}), with continuum source C contours in white.

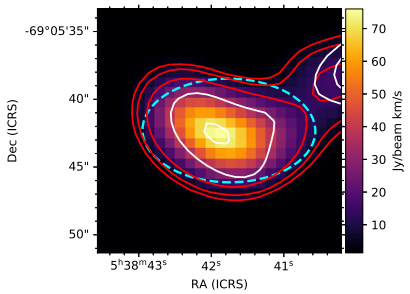

(d) Cloud no. 22 velocity integrated image, between 235.1 and 240.3 km s^{-1} (σ = 1.4 mJy beam^{-1} km s^{-1}), with continuum source E contours in white.

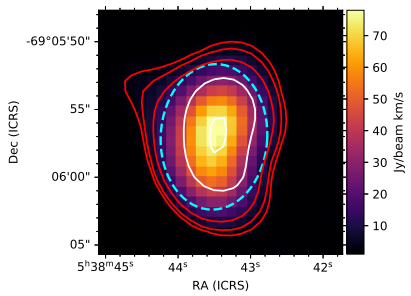

(e) Cloud no. 23 velocity integrated image, between 232.9 and 238.9 km s^{-1} (σ = 1.0 mJy beam^{-1} km s^{-1}), with continuum source F contours in white.

Figure 4.8: Velocity integrated images of ^{12}CO(3-2) emission for clouds no. 2, 15, 16, 17, 18, 22 and 23. The red contours correspond to 3, 5 and 10σ, where σ is the rms of each velocity integrated image (given in the respective captions). White contours correspond to the 1.5 and 3σ contours of the ALMA 880 μm continuum image, as in Figure 4.6. Dashed cyan ellipses represent the size of the major and minor axes found in Section 4.1.1.

the moments method (Rosolowsky & Leroy 2006) and shown in dashed, cyan color ellipses in the same figure, are similar to the continuum dust continuum sources' size, while clouds no. 22 and no. 23 are bigger than their continuum source counterparts. The similarity and difference in extension seen between the ^{12}CO(3-2) cloud and the dust cloud are dependent on the sensitivity of the observations. We expect that dust clouds would have a larger extension than the ^{12}CO(3-2) clouds in low metallicity as there is a larger envelope of H_2 not traced by ^{12}CO(3-2) and that should be traced by the dust. The fact that we see for these clouds that the dust emission cloud is smaller in size than the ^{12}CO(3-2) emission may be indicating that there is continuum emission we are not detecting due to the noise level of the ALMA 880 μm continuum image.

ID	880 μm Source	Vel. range (km s^{-1})	rms (Jy beam^{-1} km s^{-1})	A_{CO} (pc^2)
2	A	$246.6 - 253.8$	1.3	7.66
16, 17, 18	B/D	$238.0 - 249.0$	2.0	9.85
15	C	$244.4 - 250.6$	1.0	2.93
22	E	$235.1 - 240.3$	1.4	6.50
23	F	$232.9 - 238.9$	1.0	7.18

Table 4.12: Velocity ranges used to integrate the CO line cube to find the areas and radii of the CO clouds, together with the corresponding ALMA 880 μm dust source for each cloud, the rms noise of each velocity integrated image and the areas found for each cloud.

4.4.2 Gas masses obtained through CO and dust emission

In the previous section, we have determined the sizes of the molecular clouds in ^{12}CO(3-2) and compare them with the sizes of molecular clouds in dust 880 μm continuum emission. We now compare the gas mass determination of the clouds using using the dust emission and the virial mass determination. We can further determine the molecular mass from the CO emission and compare the result obtained.

To perform this comparison we need to use similar cloud areas on all cases. The sizes that we adopt are the sizes of the dust clouds as given in Table 4.9. The gas masses from dust emission were calculated in Section 4.3.4 for the chosen areas.

We determine the virial masses associated to the dust cloud areas $M_{vir}^{A_{880\mu m}}$ using Equation 1.13, adopting the sizes of the dust clouds and using the ^{12}CO(3-2) velocity FWHM of each cloud from Table 4.2. To determine the radius, we use the area as given in Table 4.9 and assumed that the cloud is spherical and obtained an equivalent radius using Equation 1.1 for each cloud. We deconvolve this equivalent radii with the ALMA beam using Equation 4.6 and used this value for the virial mass determination.

We also determine the cloud mass using ^{12}CO(3-2) luminosity inside the dust cloud area $M_{CO}^{A_{880\mu m}}$. For this determination we assume a line ratio $R_{\frac{3-2}{1-0}} \sim 2$ (Johansson et al. 1998) and a conversion factor between CO luminosity and mass, $\alpha_{^{12}CO} = 8.4 \pm 3.0$ M$_\odot$ (K km s^{-1} pc^2)$^{-1}$ (Indebetouw et al. 2013), as we did in Section 4.1.2.

The resulting ^{12}CO(3-2) luminosities and gas masses are in Table 4.13.

In the case of sources B and D, we calculate M_{gas} from the dust flux emission inside the common area, which, as said in Section 4.4.1, is $A = 6.16$ pc^2. We subtract the corresponding free-free emission $S_{ff,Br\gamma} = 44.3 \pm 11.3$ mJy to the measured continuum emission of $S_{880} = 80.5 \pm 9.0$ mJy inside this area. We obtain a total dust flux of $S_{dust} = 36.2 \pm 20.3$ mJy. Using equation 1.16, with the same $T_{\rm d}$ and ε_H as in Section 4.3.4, we obtain a gas mass $M_{gas} = 1689 \pm 949$ M$_\odot$ for sources B and D together.

ID.	$L^{A_{880\mu m}}_{^{12}CO(3-2)}$ (K km s^{-1} pc^2)	$M^{A_{880\mu m}}_{CO}$ (M$_\odot$)	$M^{A_{880\mu m}}_{vir}$ (M$_\odot$)	M_{gas} (M$_\odot$)	$\frac{M^{A_{880\mu m}}_{CO}}{M_{gas}}$	$\frac{M^{A_{880\mu m}}_{vir}}{M_{gas}}$
2	212.3 ± 2.7	892 ± 319	2260 ± 396	1353 ± 803	0.7 ± 0.5	1.7 ± 1.0
16, 17, 18	214.1 ± 6.9	899 ± 323	$2484 \pm 589^{\dagger}$	$1688 \pm 949^{*}$	0.5 ± 0.4	2.6 ± 1.6
15**	15.2 ± 1.1	64 ± 23	2118 ± 453	135 ± 639	0.5 ± 2.2	15.7 ± 74.0
22	57.0 ± 1.5	239 ± 86	1444 ± 393	485 ± 691	0.5 ± 0.7	3.0 ± 4.3
23	62.5 ± 1.1	263 ± 94	1983 ± 595	644 ± 705	0.4 ± 0.5	3.1 ± 3.5

Table 4.13: Luminosities and gas masses traced by ^{12}CO(3-2) emission, obtained within the areas covered by the 880 μm continuum sources, together with the gas mass traced by dust emission in the same areas (from Table 4.11) and the ratios $M^{A_{880\mu m}}_{CO}/M_{gas}$ and $M^{A_{880\mu m}}_{vir}/M_{gas}$. †We use $R_{\rm eq,dc} = 1.26 \pm 0.22$ pc to calculate M_{vir} for clouds no. 16, 17 and 18 together, and we use the FWHM of cloud no. 17 as the FWHM because it is the largest FWHM of the three clumps. *Mass of B and D clouds together, obtained from the dust flux in the region shared by both clouds in 880 μm continuum emission. **Cloud not resolved, so the values are not considered for analysis.

The gas masses traced by dust emission are consistently larger than the gas masses traced by ^{12}CO(3-2) luminosity $M^{A_{880\mu m}}_{CO}$, even though continuum emission seems to cover a smaller area than ^{12}CO(3-2) emission. The ratios $M^{A_{880\mu m}}_{CO}/M_{gas}$ for our sample are between 0.41 and 0.66, although in some of them (in particular for cloud no. 15/source C and cloud no. 22/source E) their uncertainties are large enough that the ratio could be > 1.

The ratios $M^{A_{880\mu m}}_{vir}/M_{gas}$ for these clouds, on the other hand, are 1.67 and 2.62 for CO clouds no. 2 and the combined emission from no. 16, 17 and 18 (where the radii in the 880 μm continuum image is resolved), with large uncertainties due to the uncertainties in M_{gas}. The upper limit of this ratio for clouds no. 15, 22 and 23, where the continuum radii is not resolved, is 3.3, 3.0 and 3.1, respectively. We expect that dust clouds trace a larger mass than the virial mass obtained from CO emission. We discuss this result in Section 4.5.4.

4.5 Discussion

4.5.1 Spatial variation in properties of CO clouds

The velocity integrated images of the ALMA ^{12}CO(3-2) line cube, integrated in 5 km s^{-1} intervals, are shown in Figure 4.9. A visual inspection of these integrated images reveals a velocity gradient in the molecular clouds near R136 with central velocities between 230 and

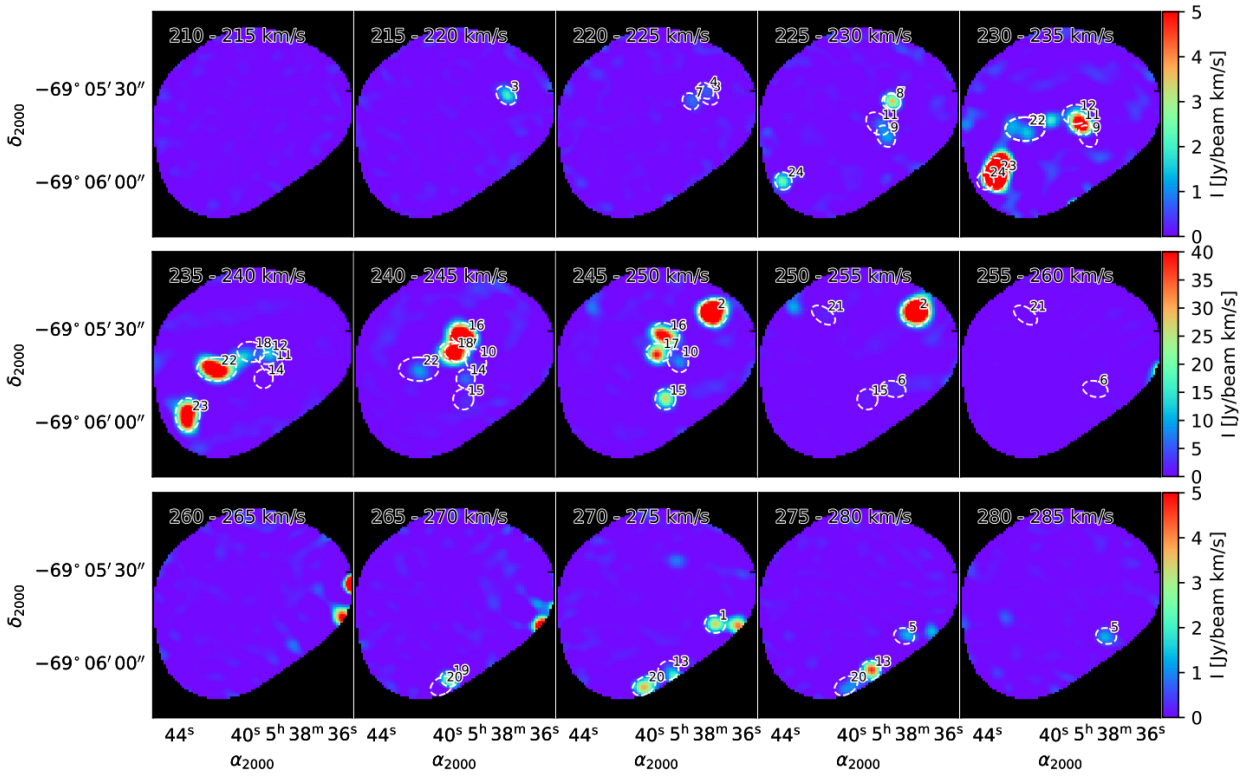

Figure 4.9: Velocity integrated images of the ALMA ^{12}CO(3-2) line shown previously in Figure 2.7. White dashed labeled ellipses represent the position and sizes of the major and minor axes of the clouds described in Section 4.1.1.

255 km s^{-1}. The clouds farther away from R136 in projection have larger central velocities. The clouds which present this velocity gradient are the brightest clouds found in Section 4.1, which belong to a northwest-southeast structure. This velocity gradient is consistent with the gradient of ^{12}CO(2-1) clouds found in Kalari et al. (2018). The largest central velocity in the gradient is at $\sim$ 250 km s^{-1}, which coincides with the R136 cluster velocity, as determined from the mean local standard of rest (LSR) radial velocity of the stars in R136 (Evans et al. 2015). Cloud no. 2 from Table 4.1 is the cloud which has the closest central velocity to this mean, with v = 250.2 km s^{-1}, and the rest of the clouds which present a velocity gradient are blueshifted with respect to R136. This supports the idea that the molecular clouds in the nortwest-southeast diagonal lie slightly in front of the YMC, as suggested by Kalari et al. (2018). The rest of the clouds, which are located outside of the northwest-southeast structure, do not seem to show a velocity gradient. These clouds are fainter in CO emission that the clouds in the northwest-southeast diagonal structure. Five of them (clouds no. 1, 5, 13, 19 and 20) have higher central velocities than the R136 cluster velocity, over 260 km s^{-1}, and thus would be redshifted from R136. Seven of them (clouds no. 3, 4, 7, 8, 9, 11 and 24) have central velocities lower than 235 km s^{-1}, and thus would be blueshifted from R136.

We plot the central velocities v_{LSR} and virial masses M_{vir} for resolved clouds that belong to the northwest-southeast diagonal in Figure 4.10. We calculate the projected distance from R136a1, a Wolf Rayet star which is taken as the center of R136, to the central position of

each cloud. We observe that there is a concentration of clouds between 7 and 9 pc which have large velocity differences. These clouds correspond to KN-2 from Kalari et al. (2018), which, as they say, is a promising region of star formation. We discuss the relation of this region with star formation in Section 4.5.5. There does not seem to be a clear correlation between distance to R136 and virial masses. Clouds from 1 to 9 pc tend to have decreasing virial masses, and the most massive cloud, no. 2, lies farthest away from R136 in projection.

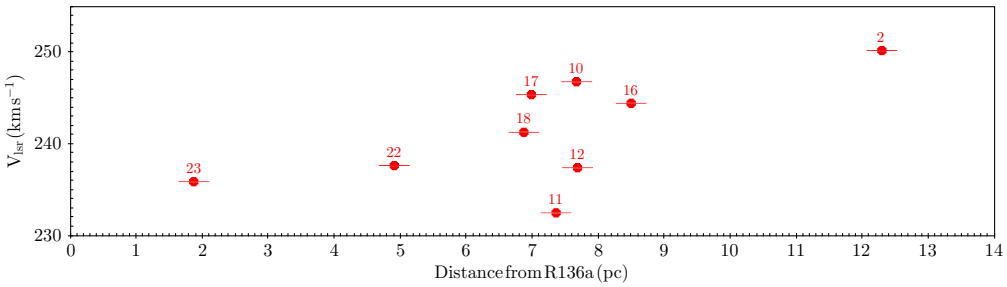

(a) Central velocity v_{LSR} plotted against the projected distance from R136a.

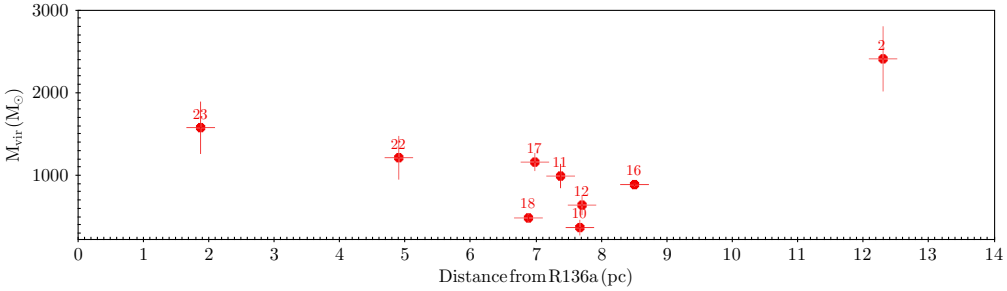

(b) Virial mass M_{vir} plotted against the projected distance from R136a.

Figure 4.10: Central velocity and virial mass plotted as a function of projected distance from R136a

4.5.2 Comparison with CO emission in previous works

As stated in Section 1, molecular gas line emission was first detected in the vicinity of R136 by Rubio et al. (2009) and was further studied by Kalari et al. (2018). We compare our results with the molecular clouds detected in these previous works.

Our results confirm the suggestions of a clumpy structure in this region in Rubio et al. (2009) using CO(2-1) and CS(2-1) observations. We resolve sub-parsec size clouds, some of them very close to each other. Cloud no. 17 coincides in position and velocity with their strongest CO and CS component. Clouds no. 2 and no. 12 coincide with the other two velocity components. Our clouds no. 11, 12 and 15 have $\frac{I_{^{12}CO(2-1)}}{I_{^{13}CO(2-1)}}$ line ratios (10.3, 9.7 and 9.0, respectively) similar to the ratios found by Rubio et al. (2009) for this region, and the rest of the clouds have smaller line ratios, between 3.9 and 7.1.

The brightest clouds in our sample coincide spatially and spectrally with the three "knots" reported by Kalari et al. (2018) using SEST ^{12}CO(2-1) observations at $\sim$ 5.6 pc resolution. Clouds no. 22 and no. 23 coincide spatially and spectrally with KN-1. KN-2 is resolved into three clouds, no. 16, 17 and 18 in our work. Cloud no. 16 is the strongest in CO emission

of these three clouds and its center velocity coincides with that of the peak emission from KN-2. Cloud no. 2 coincides with KN-3 and both are the strongest detections in each of the samples.

In Figure 4.11, we plot the size-linewidth relation, R vs σ_v, and the σ_v^2/R vs $\Sigma_{\rm H_2}$ relation for our clouds, using the R, σ_v and $\Sigma_{\rm H_2}$ from Tables 4.1 and 4.2. For comparison, we also plot these relationships for the previously mentioned KN molecular clouds in Kalari et al. (2018) using ^{12}CO(2-1) emission, molecular clouds in 30Dor further away from R136 (from Nayak et al. (2016) with $\sim$ 0.5 pc resolution, and from Pineda et al. (2009) with $\sim$ 15 pc resolution), clouds in other regions of the LMC from Wong et al. (2011), with a resolution of $\sim$ 15 pc, and clouds in the Milky Way from Heyer et al. (2009).

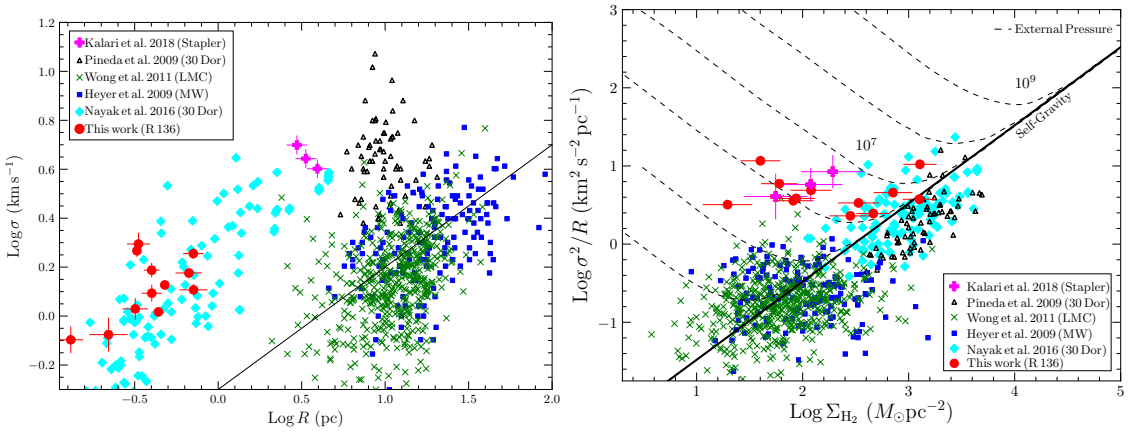

(a) (b)

Figure 4.11: Relationships between physical properties of our sample, together with results in this same region found in Kalari et al. (2018), in 30Dor from Nayak et al. (2016) with $\sim$ 2" resolution ($\sim$ 0.5 pc) and Pineda et al. (2009) with 45" resolution ($\sim$ 15 pc), in the LMC from Wong et al. (2011). (a) Size-linewidth R vs σ_v relationship for molecular clouds in different galaxies, including our results and other regions in 30Dor, the LMC and the Mikly Way. The black line represents the canonical relation $\sigma_v = 0.72R^{0.5}$, followed by the Milky Way clouds. (b) σ_v^2/R vs Σ_{H_2} relationship for molecular clouds in different galaxies, including our results and other regions in 30Dor, the LMC and the Milky Way. The solid black line represents the approximate σ_v^2/R value for increasing Σ_{H_2} of an isolated virialized cloud confined by self-gravity. Dashed lines mark the external pressure required to confine a cloud for a given σ_v^2/R value, assuming a centrally concentrated cloud in hydrostatic equilibrium. Dashed lines cover the range $P/k_B = 1 \sim 10^3 - 10^9$ cm^{-3} K.

The molecular clouds found in this work have similar sizes, velocity dispersions and surface densities in comparison to other clouds located further away from R136 in 30Dor. Our clouds lie in the same region in the size-linewidth relation as the molecular clouds found by Nayak et al. (2016). Clouds in 30Dor from our work, Nayak et al. (2016), Kalari et al. (2018) and Pineda et al. (2009) seem to follow the same linear trend as the canonical relation for Milky Way clouds, but with larger velocity dispersions for a certain radii.

Molecular clouds confined by self-gravity follow a linear relation in the σ_v^2/R vs Σ_{H_2} plot. The clouds with largest Σ_{H_2}, which are located in the nortwest-southeast diagonal structure

mentioned in Section 4.1, fall approximately on the self-gravity equilibrium line, together with molecular clouds farther away from R136 from Nayak et al. (2016), other clouds in the LMC and the Milky Way. These clouds fall in a different region in the σ_v^2/R vs Σ_{H_2} relation than clouds from Kalari et al. (2018). These bright clouds from our work might not be affected by the external radiation pressure from R136. According to theoretical models (Dale et al. 2012), dense molecular gas should be evacuated within a $10-15$ pc radius from R136. Even though these clouds are, at least, less than 20 pc away from R136 (Chevance et al. 2016; Kalari et al. 2018), they seem to be unaffected by the radiation pressure. The effect of R136 over these clouds might be reflected in the velocity gradient found in Section 4.5.1 and not in their individual physical properties. For the clouds that are over the self-gravity line in Figure 4.12, this might be a reflection of the larger external pressures they suffer due to their proximity to R136. The CO clouds near R136 are in a region where external pressure is $\sim (0.85-1.2)\times10^6$ cm^{-3} K (Chevance et al. 2016), which is consistent with the external pressure needed to keep these clouds in equilibrium, according to Kalari et al. (2018). In conclusion, the brightest clouds in our sample seem to be very similar to other clouds farther away from R136, even though they are close to a YMC, and the smallest, less bright clouds might be sustained by the external radiation pressure.

4.5.3 Comparison between molecular line emission in R136 and the LMC

The excitation temperatures T_{ex} obtained from ^{12}CO(3-2) emission are smaller than the temperatures obtained for other regions in 30Dor, but similar to the temperatures obtained in other HII regions in the LMC, when assuming LTE. The maximum T_{ex} of our sample is for cloud no. 2, with 33.39 K, whereas the T_{ex} at the peak of the clumps in the 30Dor-10 region, calculated with ^{12}CO(2-1) line emission, are between $\sim$ 40 and 60 K (see Figure 10 of Indebetouw et al. 2013). The difference in T_{ex} is expected, because ^{12}CO(2-1) emission in 30Dor-10 is at least $\sim$ 5 times larger than ^{12}CO(2-1) emission near R136 (Kalari et al. 2018). T_{ex} in clouds no. 17, 18, 22 and 23 are similar to the excitation temperature found for the N113 region, $T_{ex} \sim 20$ K (Paron et al. 2014). T_{ex} in clouds no. 2 and no. 16 is larger than in N113 by $\sim$ 10 K. T_{ex} for clouds no. 8, 10, 11, 12, 14 and 15, which have the lowest excitation temperatures of our sample, are similar to the ones found in N11 clouds by Celis Peña et al. (2019), which range from 7 K to 13 K. These low temperatures could be because these clouds are not completely resolved (or in the case of clouds no. 8, 14 and 15, not resolved at all, according to Table 4.2), and therefore they do not fill the beam size completely. This results in a lower T_{ex} than the real value. In general, the excitation temperatures of the clouds in this work are similar to excitation temperatures in LMC HII regions which are less bright than 30Dor.

The column densities $N(H_2)$ and $N(^{13}CO)$ in our molecular clouds, obtained through ^{12}CO(3-2) and ^{13}CO(3-2) emissions and assuming LTE, are smaller than the column densities in 30Dor, but the brightest clouds of our sample have comparable densities to those obtained in other regions in the LMC (with the same assumptions). For example, $N(^{13}CO)$ for clouds in the 30Dor-10 region are $(1-5)\times10^{16}$ cm^{-2} (Indebetouw et al. 2013), an order of magnitude larger than $N(^{13}CO)$ for clouds in this study. Similarly for the peak $N(H_2)$ column densities. The only cloud from our sample which has comparable $N(^{13}CO)$ and $N(H_2)$ is cloud no. 2 (the cloud farthest away from R136 in projection), with $N(^{13}CO) = 1.32 \pm 0.13 \times 10^{16}$ cm^{-2}

and an $N(H_2) = 2.23 \times 10^{22}$ cm^{-2}. The clouds which have the largest $N(H_2)$ column densities of our sample, located in northwest-southeast diagonal structure (no. 2, 16, 17, 18, 22 and 23), have $N(H_2)$ between $(0.6 - 2.4) \times 10^{22}$ cm^{-2}, similar to $N(H_2)$ peak column densities found in the N11 region in the LMC, between $(1 - 3.9) \times 10^{22}$ cm^{-2} (Celis Peña et al. 2019). The 30Dor-10 and N11 clouds were observed with different spatial resolution, 0.5 pc and 5.6 pc respectively, and thus the column densities could be different as the first totally resolve the CO clouds. The rest of the clouds have lower $N(H_2)$ densities than clouds in N11. In general, the molecular clouds in the vicinity of R136 have lower $N(H_2)$ densities than other bright regions in 30Dor farther away from R136, and our brightest clouds have similar peak densities than clouds in N11 in the LMC.

There are a few studies in the LMC in which different isotopes of the CO molecule have been observed and even fewer in other different molecular species such as the ones we present. These are concentrated mainly towards the regions N113 (Paron et al. 2014), N159 (Minamidani et al. 2011; Paron et al. 2016), and N11 (Celis Peña et al. 2019), and only a couple include the 30Dor region (Indebetouw et al. 2013; Minamidani et al. 2011; Rubio et al. 2009). The regions N113, 1159, N44 and N105 in the LMC have been observed in the millimeter and in lower rotational transitions by Seale et al. (2012). We compare the line ratios calculated for the clouds near R136 with the line ratios found in the mentioned works.

We find ^{12}CO(3-2)/^{13}CO(3-2) line ratios that are consistent with ^{12}CO/^{13}CO line ratios in 30Dor and other regions in the LMC. The $\frac{I_{^{12}CO(3-2)}}{I_{^{13}CO(3-2)}}$ line ratios we find in the 30Dor clouds near R136, with values between 3.9 and 10.3, are consistent with $\frac{I_{^{12}CO(3-2)}}{I_{^{13}CO(3-2)}}$ line ratios found in 30Dor clouds farther away from R136, between 5.5 and 8.2 (Minamidani et al. 2011, with $\sim$ 10 pc resolution). Only two clouds no. 11 and no. 12, have a higher ratio value of 10.3 and 9.7, respectively, while clouds no. 2 and no. 8 show ratios lower than 5. Our clouds also have a similar range of $\frac{^{12}CO(3-2)}{^{13}CO(3-2)}$ ratios than clouds in N11, between 6.5 and 13 (Celis Peña et al. 2019, with $\sim$ 5" resolution), except for clouds no. 2 and no. 8 which show a smaller ratio. Clouds no. 10, 14, 15 to 18, 22 and 23 have similar line ratios than in N159 and N113 (between 5.5 and 8.2 Minamidani et al. 2011; Paron et al. 2016, 2014), whereas clouds no. 11 and no. 12 have similar ratios than in N132 and N166 (Paron et al. 2016, 10.31 and 11.14, respectively), which are less bright HII regions than N159. The higher ^{12}CO/^{13}CO ratio in clouds no. 11 and no. 12 might suggest that they receive less UV radiation than the rest of the clouds in our sample, as they have similar ^{12}CO/^{13}CO ratios to less bright HII regions.

Based on the large velocity gradient (LVG) model (which is a non-LTE radiative transfer approximation) done in Minamidani et al. (2011), and assuming a ^{12}CO/^{13}CO abundance ratio of 50 as they do, the $\frac{I_{^{12}CO(3-2)}}{I_{^{13}CO(3-2)}}$ line ratios in our clouds indicate that they have a volume density $n(H_2) \approx 10^3 - 10^4$ cm^{-3}, where the clouds with a higher $\frac{I_{^{12}CO(3-2)}}{I_{^{13}CO(3-2)}}$ have a lower density. However, as ^{12}CO is optically thick, this ratio might be tracing the conditions towards the surface of the cloud. The critical densities of CS(7-6) and HCN(4-3) are higher than the $n(H_2)$ given here ($\sim 10^7$ and 10^8 cm $^{-3}$, respectively Evans 1999), and they trace the interior of the cloud. A non-LTE analysis using the CS and HCN lines could return a higher density.

In the following, we compare the line ratios of CS(7-6), HCO$^+$(4-3) and HCN(4-3) with

respect to ^{13}CO(3-2), with the results found for these molecular species in N159 and N113, by Paron et al. (2016) and Paron et al. (2014), the only two other regions in the LMC that have observations of CS, HCO$^+$ and HCN in the 345 GHz window:

- The $\frac{I_{CS(7-6)}}{I_{^{13}CO(3-2)}}$ ratios in most of the clouds of the northwest-southeast diagonal structure (no. 2, 16, 17 and 18, all of which have a ratio $= 0.07 \pm 0.01$) are similar to the $\frac{I_{CS(7-6)}}{I_{^{13}CO(3-2)}}$ ratio found in N113, of 0.06 ± 0.01 (Paron et al. 2014). Two clouds, no. 22 and no. 23, deviate from this value and have a smaller ratio of 0.02 and 0.05, respectively. These two clouds are the closest to R136 and their ratios are similar to the line ratio 0.03 ± 0.01 found in N159. Assuming the CS(7-6) line is optically thin as well as the ^{13}CO(3-2) line, the CS/^{13}CO ratio is a proxy for gas volume density, where a higher $\frac{I_{CS(7-6)}}{I_{^{13}CO(3-2)}}$ fraction traces a higher gas density. The $\frac{I_{CS(7-6)}}{I_{^{13}CO(3-2)}}$ ratios in these clouds might suggest a trend in density, where the clouds that are farther away from R136 are denser, as they present a higher ratio. Cloud no. 10, on the other hand, has a much higher $\frac{I_{CS(7-6)}}{I_{^{13}CO(3-2)}}$ ratio of $0.22 \approx 3$ times larger than median value (0.07) for the clouds in our sample, suggesting this cloud in particular might have a higher density.

- The $\frac{I_{HCO^+(4-3)}}{I_{^{13}CO(3-2)}}$ ratios of clouds no. 2, 8, 11, 12, 16 and 17 are between 0.5 and 0.77, and these ratios are similar to those found in N159, $= 0.58 \pm 0.12$ (Paron et al. 2016). Smaller $\frac{I_{HCO^+(4-3)}}{I_{^{13}CO(3-2)}}$ ratios of 0.26 and 0.28 are found in clouds no. 14 and no. 23, respectively, and are similar to the ratio of $= 0.36 \pm 0.01$ found in N113. The lowest $\frac{I_{HCO^+(4-3)}}{I_{^{13}CO(3-2)}}$ ratio, 0.19, is found in cloud no. 22. This value is smaller the ratios found both in N159 and N113 regions. Interestingly, clouds no. 10 and no. 15 have $\frac{I_{HCO^+(4-3)}}{I_{^{13}CO(3-2)}}$ line ratios > 1, higher than the ratios found in the in the other region studied in the LMC. The HCO$^+$/^{12}CO ratio is correlated to star formation (Heikkilä et al. 1999), with a larger ratio reflecting a greater star formation activity. Clouds no. 10 and no. 15 are the ones with the largest HCO$^+$/^{12}CO ratio, as well as the HCO$^+$/^{13}CO ratio, and both these clouds have associated YSO candidates (see Section 4.5.5).

- The $\frac{I_{HCN(4-3)}}{I_{^{13}CO(3-2)}}$ of most of the clouds in our samples show ratios between 0.11 and 0.34. These ratios are between 2 and 6 times higher than the 0.06 and 0.07 values found in N159 and N113 (Paron et al. 2014, 2016), respectively. On the other hand, clouds no. 22 and no. 23 show ratios of 0.02 and 0.04, respectively, which are $1.5 - 2$ times lower than the ratio found in N159 and N113. These clouds are the closest ones in projection to R136 located in the diagonal structure mentioned in Section 4.1. As with the CS/^{13}CO line ratio, the HCN/^{13}CO ratio indicates where the gas volume density is higher, so these lower values could also reflect a trend in density as the distance to R136 decreases as suggested from the $\frac{I_{CS(7-6)}}{I_{^{13}CO(3-2)}}$ ratio.

In general, the CS(7-6) and HCO$^+$(4-3) line ratios with respect to ^{13}CO(3-2) are similar to these ratios found in other HII regions in the LMC. In particular, clouds no. 22 and no. 23 show the lowest $\frac{I_{CS(7-6)}}{I_{^{13}CO(3-2)}}$ and $\frac{I_{HCN(4-3)}}{I_{^{13}CO(3-2)}}$ ratios, and as CS and HCN are density tracers molecules, these clouds may be the less dense clouds of our sample, which is consistent with the lowest column density $N(H_2)$ derived among the resolved clouds as reported in Table

4.8.

In the case of the HCN(4-3), the HCN(4-3) line ratio with respect to ^{13}CO(3-2) is in general higher than the ratios in other regions of the LMC. A special case is cloud no. 10, as this cloud shows a higher CS(7-6) to ^{13}CO(3-2) ratio than the HCN to ^{13}CO(3-2) ratio, opposite to the trend in all the other clouds in which this HCN is stronger than CS. This different trend can be clearly seen in the cloud spectra of the different molecules shown in Appendix B. The CS, HCO$^+$ and HCN peaks of cloud no. 10 have peak temperatures closer to the ^{12}CO and ^{13}CO temperatures value. However, inspecting each molecular line species profile in more detail (see Figure B.21), the CS and HCN emission spectra show non-Gaussian profiles different to ^{12}CO and ^{13}CO emission and thus, one Gaussian might not fit well the observed spectra. Further investigation of this cloud is needed to determine why it shows this different behaviour in the line ratios than the rest of the sample, as the detection is clear with a good S/N ratio.

The $\frac{I_{HCO^+(4-3))}}{I_{HCN(4-3)}}$ line ratios of most of the clouds are between 3.5 and 6.3. These line ratios are similar to the ratios of 4.8 ± 1.1 in N113 but lower than the ratio of 8.7 ± 1.8 in N159, obtained with ASTE ($\sim$ 5.5 pc resolution) by Paron et al. (2016). The only cloud that shows a different ratio is cloud no. 22 with a ratio of 12.2. It is interesting to compare these ratios with those obtained in the HCO$^+$(1-0) and HCN(1-0) transitions with with ATCA at 1.2 and 1.7 pc resolution towards the LMC regions N159, N113, N44 and N105 found by Seale et al. (2012). Their HCO$^+$(1-0)/HCN(1-0) mean ratio, determined for the four LMC regions, is = 5.3 for clouds without YSOs and = 3.7 for clouds with YSOs. According to Seale et al. (2012), a lower HCO$^+$(1-0)/HCN(1-0) ratio correlates to a higher volume density, which correlates with star formation. Clouds no. 10 and no. 17, have $\frac{I_{HCO^+(4-3))}}{I_{HCN(4-3)}}$ ratios of 3.51 and 4.62, respectively, which are the lowest ratio of our sample. These two clouds show an association to YSO's as discussed Section 4.5.5. The rest of the clouds do not have a YSO and have higher ratios than clouds no. 10 and no. 17, except for cloud no. 2 which has a low ratio of 4.54.

Finally, some ^{12}CO clouds in our sample do not show detection of ^{13}CO(3-2), CS(7-6), HCO$^+$(4-3) and/or HCN(4-3) emission lines. To determine if these clouds could have emission from these molecules, we estimate the peak temperatures of the emission lines assuming that the line ratios in these positions would be equal to the median values of the line ratios observed in our sample at each different molecule (Table 4.5). We find that the estimated peak temperatures for each molecular line are below the 3σ detection sensitivity limit in all the clouds where these lines were not detected. Therefore, it is possible that these clouds have ^{13}CO(3-2), CS(7-6), HCO$^+$(4-3) and HCN(4-3) molecules and higher sensitivity observations would be required to detect them.

In summary, these results we obtain suggest that the chemical properties of molecular clouds that near R136 are similar to those found in other regions in the LMC, and that they do not show difference with increasing projected distance from R136.

4.5.4 Comparison between gas and dust emission

In Section 4.4, we find that the areas covered by ^{12}CO(3-2) emission over 3σ are larger than the areas covered by the same clouds in the 880 μm continuum image over 1.5σ. Our results are different to what is found in other regions of the LMC and SMC. In the N11 star forming region, Herrera et al. (2013) found that dust clouds have a similar extension than the ^{12}CO emission. However, in the SMC, Bot et al. (2007) and Rubio et al. (2004) found CO emission which covers a smaller area than 1.2 mm continuum emission. It is most probable that there is an extended dust emission and that the present ALMA 880 μm continuum are not deep enough to detect this emission below the threshold used to determine the dust cloud size. The 880 ALMA μm continuum images is largely contaminated by the free-free emission in the region and therefore the continuum emission arising from the dust emission is under the actual sensitivity of the observations. Deeper observations with ALMA are required to detect any missing continuum emission.

The mass ratios M_{vir}/M_{CO}, $M_{vir}^{A_{880\mu m}}/M_{gas}$ and $M_{CO}^{A_{880\mu m}}/M_{gas}$ are similar to these same mass ratios in previous works in the LMC, but differ from results in the SMC. Our M_{vir}/M_{CO} and $M_{vir}^{A_{880\mu m}}/M_{gas}$ ratios are similar to these same ratios found by Herrera et al. (2013) for N11, which is the second brightest nebula in the LMC. While our $M_{CO}^{A_{880\mu m}}/M_{gas}$ are consistently < 1 in our sample, around half of the dust clouds in Herrera et al. (2013) have $M_{CO}/M_{gas} < 1$ and the other half have $M_{CO}/M_{gas} > 1$. Also, similar M_{vir}/M_{CO} ratios were found for this region by Kalari et al. (2018).

We plot the $M_{vir}^{A_{880\mu m}}/M_{gas}$ found in our clouds in Figure 4.12, together with this same ratio found in the LMC by Herrera et al. (2013), the SMC and the Milky Way by Bot et al. (2007). Our $M_{vir}^{A_{880\mu m}}/M_{gas}$ results differ from what is seen in the SMC, where Bot et al. (2007, 2010a) show that virial masses are lower than gas masses obtained from dust fluxes, and for GMCs in the Milky Way, virial masses are larger than gas masses from dust. The ratios found in this work and in Herrera et al. (2013) replicate what is found in Milky Way GMCs. We plot the M_{gas}/M_{vir} values from Bot et al. (2007), Herrera et al. (2013) and this work in Figure 4.12. Almost all clouds in the LMC from the plotted sample are below the $M_{gas}/M_{vir} = 1$ line. The difference between the molecular clouds in the southwest region of the SMC and the ones shown in this work is that our clouds are near a YMC. There appears to be a tendency in the LMC and SMC molecular clouds in Figure 4.12, where the larger the mass of the cloud, the closer the virial mass is to the gas mass from dust emission. We do not analyze this result further, but it would be interesting to investigate it in future works.

The fact that $M_{CO}/M_{gas} < 1$ but $M_{vir}/M_{gas} > 1$ for the resolved CO clouds in our sample is consistent with the possibility that we are not tracing the complete dust emission in this region, specially for those continuum sources with low signal to noise ratios like E and F Nevertheless, the difference between the observed M_{vir}, M_{CO} and M_{gas} values for each cloud in Table 4.13 are, in general, within a factor $2-3$, which means that these masses are consistent with each other. Their differences could be explained by the large error fractions in M_{gas} and also by the assumptions we made for α_{CO} (for 30Dor clouds found by Indebetouw et al. 2013) in the calculation of M_{CO}, κ (Bot et al. 2010a, assuming dust grain properties similar to the Milky Way, from) in the calculation of M_{gas} and the assumption of virial equilibrium for M_{vir}. The only cloud that has significant differences in its M_{vir}, M_{CO} and

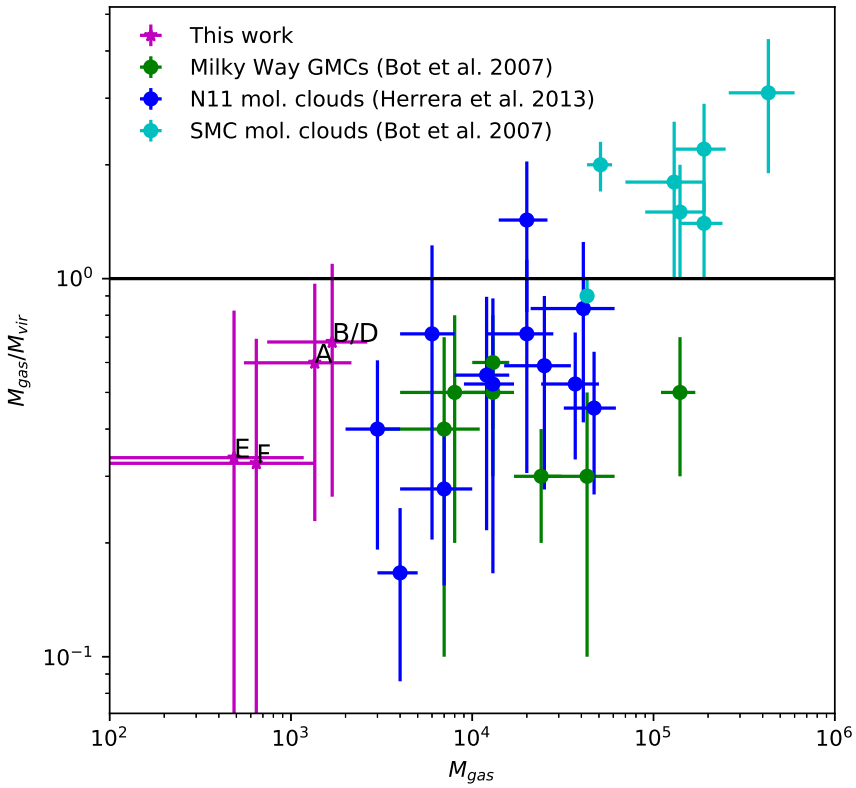

Figure 4.12: M_{gas}/M_{vir} ratio for molecular clouds found in the LMC, SMC and the Milky Way. M_{gas} is the total gas mass determined through dust emission and M_{vir} is the virial mass. We include the ratios found by Bot et al. (2007) in the SMC in cyan, Herrera et al. (2013) in N11 in blue, Milky Way values calculated in Bot et al. (2007) in green and our values in magenta stars. Our clouds are labeled according to their 880 μm continuum labels. The horizontal black line marks the $M_{gas}/M_{vir} = 1$ equality.

M_{gas} values is cloud 15/source C.

For a better estimation of M_{CO}/M_{gas} and M_{vir}/M_{gas}, we require to know M_{gas} with a smaller uncertainty, for which we require a deeper observations at 880 μm with ALMA. Single dish observations are required to recover any missing emission which covers an extension larger than 4.6 pc. Also, ALMA 12m array observations are needed to resolve the sizes of those clouds with unresolved radii, which would help in determining the M_{vir}/M_{gas} ratio for this region.

4.5.5 Gas and dust in the context of star formation

We investigate if the molecular clouds in the vicinity of R136 region show signpost of star formation. For this, we compare the molecular clouds with YSO's and embedded infrared sources found in this region in previous works. Figure 4.13 shows the velocity integrated image between 235 and 250 km s^{-1} of the ^{12}CO(3-2) line emission cube and label clouds no. 10, 11, 12, 14, 15, 17 and 18 in it. The central part of the map contains four NIR sources identified in HST/NICMOS images (Rubio et al. (1998)), some of which are identified as YSO candidates by Gruendl & Chu (2009) using Spitzer photometry. These sources are

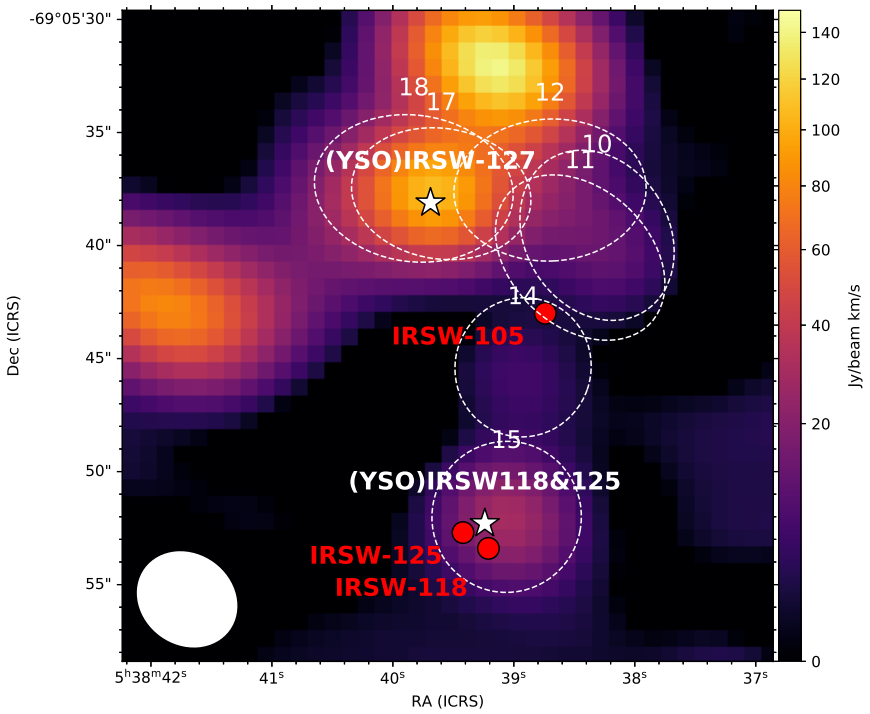

Figure 4.13: Velocity integrated image of ^{12}CO(3-2) emission between 235 and 250 km s^{-1}. White dashed ellipses represent the position and sizes of the major and minor axes of the molecular clouds no. 10, 11, 12, 14, 15, 17 and 18 found in Section 4.1.1. The white numbers over the ellipses are the cloud labels. Red points indicate the IR sources from the Rubio et al. (1998) catalog, with their corresponding lables in bold red letters. White stars represent the YSO candidates from the Gruendl & Chu (2009) Spitzer catalog, with the corresponding labels in white. The white ellipse in the bottom left corner represents the beam size.

located towards or at the border of the molecular clouds found in ^{12}CO(3-2) line emission. We describe the case of each cloud in the following:

- We find that our cloud no.15/continuum source C, detected for the first time in this work shows two NIR sources, IRSW-118 and IRSW-125, both located at the southeast (lower left) border of the cloud. These NIR sources do not show large IR excesses in the $(J-H)$ v/s $(H-K_s)$ color-color diagram, with 0.5 $<(H-K_s)<1$, Rubio et al. (1998). In this same position Gruendl & Chu (2009) reports a YSO candidate (source 053839.24-690552.3 in their catalog) but could not associate it with one specific NIR sources due to the much poorer resolution, 2", of Spitzer's IRAC images than the Las Campanas Observatory (LCO) near Infrared images with resolution of 0.35" and typical seeing of 0.8". It is interesting to note that cloud no. 15 has the largest contribution of free-free emission to the 880 continuum ALMA flux as presented in section 4.3.3. The IRSW-118 source has been associated with an optical counterpart, P702 (Parker 1993), classified as an O9.5 type star. This star could be the ionizing source that produces the free-free emission in the area (Walborn et al. 2014). We determine a smaller continuum dust emission toward cloud no. 15, continuum source C, and thus the NIR excess seen for IRSW-118 could be due to extinction towards the line of sight in that direction, while IRSW-125 could be an embedded NIR source as it is associated to a nebular knot

Rubio et al. (1998).

- Towards the position of the molecular clouds no. 17 and no. 18, we find the NIR source IRSW-127 Rubio et al. (2009) and a YSO candidate, source 053839.69-690538.1 Gruendl & Chu (2009). IRSW-127 the NIR source with the highest IR excess, $(H-K_s)$ = 2.85 the Rubio et al. (1998) catalog. In this direction, a very dense molecular cloud had been discovered by its CS emission line emission Rubio et al. (2009) and a large and strong CO molecular cloud, KN2-A had been mapped in CO by Kalari et al. (2018) who confirmed the YSO candidate as a Class II YSO based on Spitzer colors and SED fit. We have resolved KN2-A peak in two clouds, both showing CS emission. Cloud no. 17 has a central velocity of 245.4 km s^{-1} and cloud no. 18 center velocity is 241.1 km s^{-1} (see Table A.2). Cloud no. 17 has a stronger CS emission than cloud no. 18 and also shows HCN(4-3) and HCO+(4-3), indicating that this cloud is denser than cloud no. 18 as the critical density for HCN(4-3) is 10^8 cm^{-3} (Takakuwa et al. 2007). Therefore, we could conclude that cloud no. 17 is most probably the molecular cloud which has evidence of star formation.
- In the direction of the molecular clouds no. 10, 11 and 14, the NIR source IRSW-105 is located. This NIR source was associated to the outskirts of the CO cloud mentioned by Rubio et al. (2009). We can see in Figure 4.13 that its position cannot be associated to any of our resolved clouds. IRSW-105 has an very little IR excess in the $(J-H)$ v/s $(H-K_s)$ color-color diagram from Rubio et al. (1998) and its colors are consistent with a highly reddened O3 V type star.

In summary, some of the molecular clouds found in this work appear correlated with NIR sources from Rubio et al. (2009) and YSOs from Kalari et al. (2018) and Gruendl & Chu (2009), detected in the region. The parsec size resolution obtained with ALMA has allowed us to identify sources IRSW-118 and IRSW-125 with the molecular cloud no 15 and confirm the association of IRSW-127 to the densest and strongest CO cloud no. 17 towards the line of sight.

Chapter 5

Conclusion

We study the molecular gas and dust emission in Magellanic Bridge A and in the vicinity of R136 in 30Dor. In Magellanic Brdige A, we find two molecular clouds in gas and dust emission. Near R136, we find 24 individual molecular clouds using ^{12}CO(3-2) line emission and 6 individual continuum sources at 880μm. We summarize our results for each region in the following.

In Chapter 3, we characterize the molecular gas and dust emission from the Magellanic Bridge A molecular clouds using ALMA 1.3 mm continuum and CO(2−1) observations at subparsec resolution, together with APEX 870 μm continuum and CO(2−1) line observations at $\sim$ 6 pc resolution and Spitzer and Herschel FIR archival data.

At this resolution, Magellanic Bridge A separates into two components, North and South. Their dust emission has temperatures of $T_{\rm d} = 21.7 \pm 2.2$ K and $T_{\rm d} = 24.5 \pm 1.1$ K respectively, with an emissivity exponent $\beta \approx 1.4$ obtained from the MBB fitting to the FIR emission of Magellanic Bridge A at $\lambda \leq 500$ μm. The difference in temperature is consistent with the fact that the North source is not detected at 100 and 160 μm, and that its star formation activity seems to be weaker than that of the South source. Using the MBB model that best fits the FIR dust fluxes we obtain total gas masses of $(1.3 \pm 0.3) \times 10^3$ M$_\odot$ at source North and $(2.9 \pm 1.2) \times 10^3$ M$_\odot$ at source South, and a total gas mass of $(6.8 \pm 1.5) \times 10^3$ M$_\odot$ for the entire complex.

After removing possible contributions from free-free and CO line emission, the bolometer measurement at 870 μm from LABOCA shows a very significant submillimeter excess of a factor of $\sim$ 6.7 for source North and 3.0 for source South over their FIR fits. The 870 μm image exhibits morphology consistent with that of the FIR images, peaking at the location of the CO clouds. The calibration of the data does not appear to be at fault, and the noise in the image is entirely consistent with a priori expectations: in fact, without the excess there would have been a marginal detection of the source. A similar excess, however, is not detected in the ALMA 12m and Morita Array imaging at 1.3 mm. The upper limits for flux density at 1.3 mm are consistent with the predicted fluxes by the MBB model. This requires that either: 1) emission is extended enough that it is filtered out by the interferometer, or 2) that the excess is caused by a process that peaks at 870 μm (perhaps similar to the Anomalous

Microwave Emission detected at lower frequencies, Dickinson et al. 2018). High resolution observations at 870 μm with ALMA will help to establish the nature of the excess.

We find dense molecular clouds in Magellanic Bridge A using ALMA+APEX combined CO(2−1) line emission, which spatially coincide with the North and South dust sources. These two clouds have radii $\sim$ 1 pc, velocity FWHM of 1.3 and 1.9 km s^{-1} and virial masses of $\sim$ 400 and 700 M$_\odot$ for clouds North and South, respectively. Accordingly, their bulk volume densities are $n(H_2) \sim 700$ and 2600 cm^{-3}, significantly higher than the typical density of clouds in the Milky Way ($n \sim 230$ cm^{-3}, Roman-Duval et al. 2010). The total interferometric $L_{CO(2-1)}$ of the complex is 85% of the luminosity $L_{CO(2-1)}$ measured with the APEX single-dish, which suggests that most (if not all) CO(2−1) emission from Magellanic Bridge A comes from these two clouds. Using the virial mass, we find a CO-to-H_2 conversion factor α_{CO} of 6.5 ± 1.2 M$_\odot$ (K kms^{-1} pc^2)$^{-1}$ and 15.3 ± 1.6 M$_\odot$ (K km s^{-1} pc^2)$^{-1}$ for the North and South clouds respectively, consistent with the trend of α_{CO} approaching Milky Way values on the small spatial scales.

We compare the CO(2−1) and dust emissions at a common resolution of 22'. We find that CO(2−1) emission covers a smaller area than continuum emission in the South cloud, whereas they have a similar spatial extent on the more quiescent North cloud. The total gas mass derived from the dust emission $\sim$ 4 times larger than the sum of virial masses obtained for both clouds.

In Chapter 4, we characterize the molecular gas and dust emission in the vicinity of the R136 YMC in 30Dor, using ALMA band 7 observations of 880 μm continuum and molecular emission, with $\sim$ 1 pc resolution, and resolved the molecular and dust emission in sub-parsec clouds.

Our ALMA map resolves 24 ^{12}CO(3-2) molecular clouds, mainly concentrated in the region identified by Kalari et al. (2018) as the "Stapler Nebula". New CO clouds, previously undetected, are identified outside of this region. These clouds are much fainter and thus required deeper sensitivity and spatial resolution, as our ALMA data, to be detected. Several of the molecular clouds are also detected in ^{13}CO(3-2), CS(7-6), HCO$^+$(4-3) and/or HCN(4-3).

We first characterize the physical properties of molecular clouds through ^{12}CO(3-2) emission. Our clouds are mostly concentrated in a northwest-southeast diagonal in the ^{12}CO(3-2) ALMA line cube. These clouds have radii between 0.3 and 0.9 pc, velocity widths (FWHM) between 1.1 and 4.3 km s^{-1}, and CO luminosities ranging from 0.2 to 268.6 K km s^{-1} pc^2. We derive the clouds' masses using different methods and find virial masses between 88 and 2414 M$_\odot$ and masses derived from CO luminosity between 5 and 1128 M$_\odot$. Several of the CO clouds are not resolved and therefore their virial masses represent upper limits. For those resolved clouds, the virial masses we determine have values between $2-3$ times larger than the gas masses derived from ^{12}CO(3-2) luminosity in resolved clouds, using a conversion factor $\alpha_{CO} = 8.4 \pm 3.0$ M$_\odot$ pc^{-2} (K km s^{-1})$^{-1}$ (Indebetouw et al. 2013), $\sim$2 times the canonical galactic value ($\alpha_{CO} = 4.3$ M$_\odot$ pc^{-2} (K km s^{-1})$^{-1}$, see Bolatto et al. 2013, and references within). This means that, if we estimate α_{CO} for this region using the virial masses and CO luminosities, α_{CO} is $4-6$ times the canonical galactic value. The surface densities, based on the CO luminosities, range from 10 to 1276 M$_\odot$ pc^{-2} for these clouds, about an order of

magnitude smaller than surface densities in other molecular clouds in 30Dor, farther away from R136. We find that the brightest clouds have a velocity gradient, where the farther from R136, the larger their central velocity is, similar to what was found for ^{12}CO(2-1) clouds by Kalari et al. (2018).

For the first time, we have high spatial resolution observations of ^{13}CO(3-2), CS(7-6), HCO$^+$(4-3) and/or HCN(4-3) for this region. We find that, from the 24 ^{12}CO(3-2) clouds, 13 show emission in ^{13}CO(3-2), 7 show CS(7-6) line emission, 12 clouds show HCO$^+$(4-3) emission and 6 clouds show HCN(4-3) emission. The 6 clouds which present emission from all 4 molecular species are located in the northwest-southeast diagonal and tend to be the ones with the strongest emission in ^{12}CO(3-2). The presence of CS(7-6) and HCN(4-3) emission in these clouds suggest that they have a high density ($n > 10^6$ cm^{-3}). Using our results for ^{12}CO(3-2) and ^{13}CO(3-2) molecular emission, we calculate the excitation temperatures T_{ex} and the H_2 column densities $N(H_2)$ at the peak positions of our clouds, assuming LTE. The excitation temperatures for our clouds are between 5 and 33 K and there seems to be no correlation between the projected distance with T_{ex}. The resulting $N(H_2)$ for our sample ranges from 4.2 to 23.7 $\times$ 10^{21} cm^{-2}, about an order of magnitude smaller than $N(H_2)$ in molecular clouds studied in the 30Dor region but farther away form R136.

We derive line ratios for the different molecular species detected in the clouds in R136. The $\frac{I_{^{12}CO(3-2)}}{I_{^{13}CO(3-2)}}$ line ratios are between 3.9 and 10.3 and the $\frac{I_{HCO^+(4-3))}}{I_{HCN(4-3)}}$ ratios are between 3.5 and 12.2. These values are similar to the ^{12}CO/^{13}CO and HCO$^+$/HCN line emission ratios found in studies in N113 in the LMC. The $\frac{I_{CS(7-6)}}{I_{^{13}CO(3-2)}}$ line ratios are between 0.02 and 0.22, and the $\frac{I_{HCO^+(4-3)}}{I_{^{13}CO(3-2)}}$ ratios range between 0.19 and 1.2. These two line ratios are similar to these same ratios in other regions of the LMC, except for our cloud no. 20, which has a higher ratio of $\frac{I_{CS(7-6)}}{I_{^{13}CO(3-2)}} = 0.22$. The $\frac{I_{HCN(4-3)}}{I_{^{13}CO(3-2)}}$ ratios are between 0.02 and 0.34 for our clouds, and most of our clouds have a higher ratio than those found in other regions in the LMC. The main difference is that N11, N159 and N113 are less bright HII regions than 30Dor.

The dust continuum map at 880 μm in the vicinity of R136 shows emission with a similar spatial distribution as the molecular line emission. The continuum emission mapped by ALMA is dominated by the free-free emission, contributing between 50 to 85% of the total 880 μm continuum flux in the observed clouds, as expected in an HII region. We subtract the free-free emission from the continuum flux to obtain the dust continuum emission of the clouds. The continuum dust clouds have resolved sizes with radii values ranging between 0.42 and 0.66 pc. These radii are smaller than the radii found for the resolved ^{12}CO(3-2) clouds. The difference in the observed size between the dust cloud and the CO cloud may be explained due to a the different sensitivity achieved in the observations. There could be extended continuum dust emission which is below the detection threshold and thus not detected by our ALMA 880 μm continuum observations. We derive the total gas masses from the dust emission and found dust clouds masses between 135 and 1353 M$_\odot$.

We compare the mass of the clouds obtained through the different methods. The virial masses, the molecular masses derived from the CO luminosity and the gas mass from dust emission are determined in the same area for each cloud observed in continuum emission to make the comparison. We find that the virial masses in this case are $2-3$ times larger

than the gas masses obtained from dust emission in the same area, which is consistent with previous findings in the LMC where virial masses are larger than the gas masses derived from dust emission. On the other hand, gas masses obtained from dust emission are similar than the gas masses obtained from CO luminosity. When using a fixed conversion factor of $\alpha_{^{12}CO} = 8.4 \pm 3.0$ M$_\odot$ (K km s^{-1} pc^2)$^{-1}$ which is twice the canonical Milky Way conversion factor, the two masses are similar within a factor of 2. The M_{vir}/M_{gas} ratios are similar to these comparisons in other regions in the LMC, but different to results in the SMC.

The properties of the studied molecular clouds near R136 seem to be very similar to other molecular clouds properties located in different environments when analyzed with a similar spatial resolution. These CO clouds tend to have higher surface densities which is required to be able to shield the UV radiation field that will produce a higher photodissociation of the CO in low metallicity and low dust to gas-ratio environment. We see no evidence of an important effect on the cloud properties due to the fact that these clouds are so close to R136 and immerse and a strong UV radiation field.

Further work is required to better understand how these clouds survive close to R136. Non-LTE models such as RADEX could be applied to estimate the volume densities and kinetic temperatures of these clouds, using the line intensities and ratios found in this work. Deeper ALMA observations, together with Total Power array observations, would allow to resolve the size of the molecular clouds in 880 μm continuum. Also, higher resolution observations would allow to resolve the individual molecular clouds in gas and dust, and continuum observations with similar or better resolutions in other wavelengths can allow a deeper study of the physical properties of dust in this region.

It is interesting to compare the physical properties of the molecular clouds found in Magellanic Bridge A and 30Dor using CO emission. Both regions are observed with ALMA at a similar spatial resolution of 0.3 pc and 1 pc, respectively. Although they are observed in different CO rotational transitions $J = 2 - 1$ and $J = 3 - 2$, the derived properties are not affected by this in an important way. The results for both regions are the following:

1. Molecular clouds found in Magellanic Bridge A have larger radii than resolved clouds in 30Dor: Magellanic Bridge A North and South clouds have$R$ = 1.3 pc and 1.0 pc, respectively, while radii for clouds in 30Dor range from 0.3 to 0.9 pc.
2. Magellanic Bridge A clouds North and South have CO luminosities lower than clouds in 30Dor: while clouds North and South have L_{CO} of 68 and 48 K km s^{-1} pc^2 respectively, resolved clouds in 30Dor have luminosities that range from 67 to 268 K km s^{-1} pc^2.
3. Surface densities in Magellanic Bridge A clouds, 80 M$_\odot$ pc^{-2} for source North and 230 M$_\odot$ pc^{-2} for source South, are lower than the surface densities in 30Dor resolved clouds, which range from 280 to 1260 M$_\odot$ pc^{-2} .
4. Virial masses in Magellanic Bridge A are smaller than virial masses in 30Dor. While Magellanic Bridge A clouds North and South have virial masses of 437 and 733 M$_\odot$, respectively, near R136 the virial masses range from $\sim$ 100 to 2400 M$_\odot$ for resolved clouds.
5. The derived α_{CO} conversion factors in Magellanic Bridge A are around 2-4 times the canonical galactic value $\alpha_{CO} = 4.3$ M$_\odot$ (K km s^{-1} pc^2)$^{-1}$, whereas α_{CO} estimated using the virial masses in 30Dor gives a conversion factor 4-6 times the canonical galactic

value.

We analize the physical properties found in the molecular clouds in Magellanic Bridge A and 30Dor and see how the properties could be affected to the different environment in which they are located.

First, these two regions have different metallicities and different gas-to-dust ratios. The metallicity in 30Dor is $\sim Z_{\odot}/2$ (Rolleston et al. 2002), whereas in Magellanic Bridge A is $\sim Z_{\odot}/5$ (Lee et al. 2005) and the gas to dust ratos are 380 for the LMC (Roman-Duval et al. 2014) and 1200 for the Magellanic Bridge (Gordon et al. 2009). These two might have an effect in the CO luminosities because, as the metallicity decreases and the gas to dust ratio increases, the CO cloud is smaller in size with an increasing larger envelope of molecular H_2 gas. (Bolatto et al. 2013).

Second, the larger virial masses in 30Dor are a consequence of the larger velocity widths (FWHM) in comparison with those in Magellanic Bridge A, as the size of the clouds are not too different. The larger velocity dispersion (FWHM) in 30Dor could be because of a higher turbulence in the medium, due to a high energy input from the hundreds of massive stars in R136 as well as strong winds. This larger energy input might also explain why the sizes of 30Dor clouds are about 0.2 pc smaller than clouds in Magellanic Bridge A, as for a stronger radiation field, the area where CO is not photodissociated is smaller Bolatto et al. (2013). On the contrary, the Magellanic Bridge A region is a more quiescent region with only a few O type stars radiating close to the molecular clouds and thus not exposed to high UV radiation nor strong stellar winds.

In general, the molecular clouds studied in this thesis show properties which are quite similar to properties of molecular clouds characterized in the LMC and SMC. The smaller sizes would explain why the α_{CO} factor tends to reach the value of the canonical Galactic conversion factor as the CO cloud is completely resolved and covers the same area as the H_2 cloud which are the conditions found in the molecular clouds in GMC's in the Milky Way.

We see no evidence that Magellanic Bridge A clouds are different from clouds in the SMC, and that clouds near R136 have different physical properties than clouds farther away from the central YMC. Our results seems to show that once the conditions in the ISM are those that allow the formation of a molecular cloud, the cloud properties become independent of the medium in which is formed.

Bibliography

Bendo, G. J., Dale, D. A., Draine, B. T., et al. 2006, ApJ 652, 283

Bergin, E. A. & Tafalla, M. 2007, ARA&A 45, 339

Besla, G., Kallivayalil, N., Hernquist, L., et al. 2012, MNRAS 421, 2109

Bica, E., Santiago, B., Bonatto, C., et al. 2015, MNRAS 453, 3190

Bica, E. L. D. & Schmitt, H. R. 1995, ApJS 101, 41

Bolatto, A. D., Leroy, A., Israel, F. P., & Jackson, J. M. 2003, ApJ 595, 167

Bolatto, A. D., Leroy, A. K., Jameson, K., et al. 2011, ApJ 741, 12

Bolatto, A. D., Leroy, A. K., Rosolowsky, E., Walter, F., & Blitz, L. 2008, ApJ 686, 948

Bolatto, A. D., Wolfire, M., & Leroy, A. K. 2013, ARA&A 51, 207

Bot, C., Boulanger, F., Rubio, M., & Rantakyro, F. 2007, A&A 471, 103

Bot, C., Rubio, M., Boulanger, F., et al. 2010a, A&A 524, A52

Bot, C., Ysard, N., Paradis, D., et al. 2010b, A&A 523, A20

Brunetti, N. & Wilson, C. D. 2019, MNRAS, 483, 1624

Celis Peña, M., Paron, S., Rubio, M., Herrera, C. N., & Ortega, M. E. 2019, A&A, 628, A96

Chen, C. H. R., Indebetouw, R., Muller, E., et al. 2014, ApJ 785, 162

Chevance, M., Madden, S. C., Lebouteiller, V., et al. 2016, A&A, 590, A36

Chu, Y.-H. & Kennicutt, Robert C., J. 1994, ApJ, 425, 720

Cioni, M. R. L., van der Marel, R. P., Loup, C., & Habing, H. J. 2000, A&A, 359, 601

Dale, J. E., Ercolano, B., & Bonnell, I. A. 2012, MNRAS, 424, 377

Dickel, J. R., McIntyre, V. J., Gruendl, R. A., & Milne, D. K. 2005, AJ, 129, 790

Dickinson, C., Ali-Haïmoud, Y., Barr, A., et al. 2018, New A Rev. 80, 1

Drabek, E., Hatchell, J., Friberg, P., et al. 2012, MNRAS 426, 23

Draine, B. T. & Hensley, B. 2012, ApJ 757, 103

Dufour, R. J., Shields, G. A., & Talbot, R. J., J. 1982, ApJ 252, 461

Evans, C. J., Kennedy, M. B., Dufton, P. L., et al. 2015, A&A, 574, A13

Evans, Neal J., I. 1999, ARA&A, 37, 311

Evans, Neal J., I., Heiderman, A., & Vutisalchavakul, N. 2014, ApJ 782, 114

Field, G. B., Blackman, E. G., & Keto, E. R. 2011, MNRAS 416, 710

Galametz, M., Albrecht, M., Kennicutt, R., et al. 2014, MNRAS 439, 2542

Galametz, M., Madden, S., Galliano, F., et al. 2009, A&A 508, 645

Galliano, F., Madden, S. C., Jones, A. P., Wilson, C. D., & Bernard, J. P. 2005, A&A 434, 867

Galliano, F., Madden, S. C., Jones, A. P., et al. 2003, A&A 407, 159

Garay, G., Johansson, L. E. B., Nyman, L. Å., et al. 2002, A&A, 389, 977

Gardiner, L. T., Sawa, T., & Fujimoto, M. 1994, MNRAS 266, 567

Gaustad, J. E., McCullough, P. R., Rosing, W., & Van Buren, D. 2001, PASP, 113, 1326

Gordon, K. D., Bot, C., Muller, E., et al. 2009, ApJL 690, L76

Gordon, K. D., Meixner, M., Meade, M. R., et al. 2011, AJ 142, 102

Gordon, K. D., Roman-Duval, J., Bot, C., et al. 2014, ApJ 797, 85

Gruendl, R. A. & Chu, Y.-H. 2009, ApJS, 184, 172

Guzmán, V. 2010, Master's thesis, Universidad de Chile

Harries, T. J., Hilditch, R. W., & Howarth, I. D. 2003, MNRAS 339, 157

Harris, J. 2007, ApJ 658, 345

Heiderman, A., Evans, Neal J., I., Allen, L. E., Huard, T., & Heyer, M. 2010, ApJ 723, 1019

Heikkilä, A., Johansson, L. E. B., & Olofsson, H. 1999, A&A, 344, 817

Hermelo, I., Relaño, M., Lisenfeld, U., et al. 2016, A&A 590, A56

Herrera, C. N., Rubio, M., Bolatto, A. D., et al. 2013, A&A, 554, A91

Heyer, M., Krawczyk, C., Duval, J., & Jackson, J. M. 2009, ApJ, 699, 1092

Hildebrand, R. H. 1983, QJRAS 24, 267

Hindman, J. V., Kerr, F. J., & X.McGee, R. 1963, Australian Journal of Physics, 16, 570

Hunt, L. K., Dyer, K. K., Thuan, T. X., & Ulvestad, J. S. 2004, ApJ 606, 853

Indebetouw, R., Brogan, C., Chen, C. H. R., et al. 2013, ApJ 774, 73

Israel, F. P. 1997, A&A 328, 471

Jameson, K. E., Bolatto, A. D., Leroy, A. K., et al. 2016, ApJ 825, 12

Jameson, K. E., Bolatto, A. D., Wolfire, M., et al. 2018, ApJ 853, 111

Johansson, L. E. B., Greve, A., Booth, R. S., et al. 1998, A&A, 331, 857

Kalari, V. M., Rubio, M., Elmegreen, B. G., et al. 2018, ApJ 852, 71

Kalari, V. M., Rubio, M., Saldaño, H. P., & Bolatto, A. D. 2020, MNRAS submitted

Larson, R. B. 1981, MNRAS 194, 809

Lee, J. K., Rolleston, W. R. J., Dufton, P. L., & Ryans, R. S. I. 2005, A&A 429, 1025

Lehner, N., Howk, J. C., Keenan, F. P., & Smoker, J. V. 2008, ApJ 678, 219

Lehner, N., Sembach, K. R., Dufton, P. L., Rolleston, W. R. J., & Keenan, F. P. 2001, ApJ 551, 781

Lequeux, J. 2005, The Interstellar Medium (Springer)

Lequeux, J., Le Bourlot, J., Pineau des Forets, G., et al. 1994, A&A 292, 371

Leroy, A., Bolatto, A., Stanimirovic, S., et al. 2007, ApJ 658, 1027

Lisenfeld, U., Israel, F. P., Stil, J. M., & Sievers, A. 2002, A&A 382, 860

MacLaren, I., Richardson, K. M., & Wolfendale, A. W. 1988, ApJ 333, 821

McClure-Griffiths, N. M., Pisano, D. J., Calabretta, M. R., et al. 2009, ApJS 181, 398

McKee, C. F. & Ostriker, E. C. 2007, ARA&A 45, 565

McMullin, J. P., Waters, B., Schiebel, D., Young, W., & Golap, K. 2007, in Astronomical Society of the Pacific Conference Series, Vol. 376, Astronomical Data Analysis Software and Systems XVI, ed. R. A. Shaw, F. Hill, & D. J. Bell, 127

Meixner, M., Panuzzo, P., Roman-Duval, J., et al. 2013, AJ 146, 62

Meny, C., Gromov, V., Boudet, N., et al. 2007, A&A 468, 171

Minamidani, T., Tanaka, T., Mizuno, Y., et al. 2011, AJ, 141, 73

Miville-Deschênes, M.-A., Murray, N., & Lee, E. J. 2017, ApJ 834, 57

Mizuno, A., Onishi, T., Yonekura, Y., et al. 1995, ApJL 445, L161

Mizuno, A., Yamaguchi, R., Tachihara, K., et al. 2001, PASJ 53, 1071

Mizuno, N., Muller, E., Maeda, H., et al. 2006, ApJ, 2, 107

Muller, E., Mizuno, N., Minamidani, T., et al. 2014, PASJ 66, 4

Muller, E. & Parker, Q. A. 2007, PASA 24, 69

Muller, E., Staveley-Smith, L., Zealey, W., & Stanimirovic, S. 2003a, MNRAS, 339, 105

Muller, E., Staveley-Smith, L., & Zealey, W. J. 2003b, MNRAS 338, 609

Murai, T. & Fujimoto, M. 1980, PASJ, 32, 581

Muraoka, K., Homma, A., Onishi, T., et al. 2017, ApJ 844, 98

Nayak, O., Meixner, M., Indebetouw, R., et al. 2016, ApJ 831, 32

Nikolić, S., Garay, G., Rubio, M., & Johansson, L. E. B. 2007, A&A 471, 561

Osterbrock, D. E. & Ferland, G. J. 2006, Astrophysics of gaseous nebulae and active galactic nuclei (University Science Books)

Parker, J. W. 1993, AJ, 106, 560

Paron, S., Ortega, M. E., Cunningham, M., et al. 2014, A&A, 572, A56

Paron, S., Ortega, M. E., Fariña, C., et al. 2016, MNRAS, 455, 518

Pietrzyński, G., Graczyk, D., Gieren, W., et al. 2013, Nature, 495, 76

Pineda, J. L., Ott, J., Klein, U., et al. 2009, ApJ, 703, 736

Planck Collaboration, Ade, P. A. R., Aghanim, N., et al. 2011, A&A, 536, A17

Rolleston, W. R. J., Trundle, C., & Dufton, P. L. 2002, A&A, 396, 53

Rolleston, W. R. J., Venn, K., Tolstoy, E., & Dufton, P. L. 2003, A&A 400, 21

Roman-Duval, J., Gordon, K. D., Meixner, M., et al. 2014, ApJ 797, 86

Roman-Duval, J., Jackson, J. M., Heyer, M., Rathborne, J., & Simon, R. 2010, ApJ 723, 492

Rosolowsky, E. & Leroy, A. 2006, PASP 118, 590

Rubio, M., Barbá, R. H., Walborn, N. R., et al. 1998, AJ, 116, 1708

Rubio, M., Boulanger, F., Rantakyro, F., & Contursi, A. 2004, A&A 425, L1

Rubio, M., Elmegreen, B. G., Hunter, D. A., et al. 2015, Nature 525, 218

Rubio, M., Lequeux, J., & Boulanger, F. 1993, A&A 271, 9

Rubio, M., Lequeux, J., Boulanger, F., et al. 1996a, A&AS 118, 263

Rubio, M., Lequeux, J., Boulanger, F., et al. 1996b, A&AS 118, 263

Rubio, M., Paron, S., & Dubner, G. 2009, A&A, 505, 177

Rybicki, G. B. & Lightman, A. P. 1986, Radiative Processes in Astrophysics (Wiley-VCH)

Saldaño, H. P., Rubio, M., Jameson, K., & Bolatto, A. D. 2018, Boletin de la Asociacion Argentina de Astronomia La Plata Argentina, 60, 192

Savaglio, S., Glazebrook, K., Le Borgne, D., et al. 2005, ApJ 635, 260

Schlafly, E. F. & Finkbeiner, D. P. 2011, ApJ 737, 103

Schruba, A., Leroy, A. K., Kruijssen, J. M. D., et al. 2017, ApJ 835, 278

Seale, J. P., Looney, L. W., Wong, T., et al. 2012, ApJ, 751, 42

Shetty, R., Kauffmann, J., Schnee, S., & Goodman, A. A. 2009, ApJ 696, 676

Shu, F. H., Adams, F. C., & Lizano, S. 1987, ARA&A 25, 23

Siringo, G., Kreysa, E., Kovács, A., et al. 2009, A&A 497, 945

Solomon, P. M., Rivolo, A. R., Barrett, J., & Yahil, A. 1987, ApJ 319, 730

Sorai, K., Hasegawa, T., Booth, R. S., et al. 2001, ApJ 551, 794

Staveley-Smith, L., Kim, S., Putman, M., & Stanimirovic, S. 1998, RvMA, 11, 117

Takakuwa, S., Ohashi, N., Bourke, T. L., et al. 2007, ApJ, 662, 431

Tielens, A. G. G. M. 2005, The Physics and Chemistry of the Interstellar Medium (Cambridge University Press)

Valdivia-Mena, M. T., Rubio, M., Bolatto, A. D., Saldaño, H. P., & Verdugo, C. 2020s, A&A in press

Vassilev, V., Meledin, D., Lapkin, I., Belitsky, V., & et al. 2008, A&A, 490, 1157

Verdugo, C. 2012, Master's thesis, Universidad de Chile

Virtanen, P., Gommers, R., Oliphant, T. E., et al. 2020, Nature Methods, 17, 261

Visser, R., van Dishoeck, E. F., & Black, J. H. 2009, A&A 503, 323

Walborn, N. R. 1991, in IAU Symposium, Vol. 148, The Magellanic Clouds, ed. R. Haynes & D. Milne, 145

Walborn, N. R., Sana, H., Simón-Díaz, S., et al. 2014, A&A, 564, A40

Williams, J. P., de Geus, E. J., & Blitz, L. 1994, ApJ 428, 693

Wilson, T. L., Rohlfs, K., & Hüttemeister, S. 2009, Tools of Radio Astronomy (Springer)

Wong, T., Hughes, A., Ott, J., et al. 2011, ApJS, 197, 16

Wong, T., Hughes, A., Tokuda, K., et al. 2017, ApJ 850, 139

Zahid, H. J., Geller, M. J., Kewley, L. J., et al. 2013, ApJL 771, L19

Appendix A

CPROPS detections in ^{13}CO(3-2), CS(7-6), HCO$^+$(4-3) and HCN(4-3)

Tables A.1 to A.4 contain the results from running CPROPS in the ^{13}CO(3-2), CS(7-6), HCO$^+$(4-3) and HCN(4-3) ALMA line cubes, with the same parameters as those stated in Section 4.1.1. We select those emissions that, according to CPROPS, have $S/N > 5$, and manually inspect the results to leave out false detections. We then match the emissions found in each molecule with its corresponding cloud detected in the ^{12}CO(3-2) line cube, according to their position (α, δ) and central velocities v. We report the properties obtained through CPROPS for each molecule: α, δ v, velocity FWHM Δv, peak temperatures T_{peak}, deconvolved radii $R_{\rm dc}$ and not deconvolved radii R, and luminosities of each molecular species.

The radii are calculated from the second moments of emission along the major and minor axes of the clumps, delivered by CPROPS. When the clump is unresolved (which means that one or both of the second moments of emission of the cloud are smaller than σ_{beam}, see Section 4.1.2), we use Equation 4.2 to calculate the upper limit to the deconvolved.

In the case of cloud no. 11, we add a detection in ^{13}CO(3-2) which is not detected by CPROPS but is detected after a manual inspection of the ^{13}CO(3-2) line cube. We do not attempt to characterize its size in this work.

ID	α (J2000)	δ (J2000)	T_{peak} (K)	v (km s^{-1})	Δv (km s^{-1})	$R_{\rm dc}$ (pc)	R (pc)	$L_{^{13}CO(3-2)}$ (K km s^{-1} pc^2)
2	05:38:36.2	-69:05:24.0	8.13	250.1	3.5 ± 0.2	0.42 ± 0.06	1.01 ± 0.13	56.14 ± 5.08
8	05:38:37.6	-69:05:33.7	0.28	227.8	1.5 ± 0.3	$< 0.16 \pm 0.04$	0.74 ± 0.23	0.56 ± 0.05
10	05:38:38.2	-69:05:40.0	0.47	246.6	2.0 ± 0.4	$< 0.23 \pm 0.05$	0.78 ± 0.21	1.12 ± 0.11
11	05:38:38.6	-69:05:41.1	0.15	232.3	-	-	-	-
12	05:38:38.6	-69:05:38.7	0.31	235.5	7.9 ± 0.6	$< 0.50 \pm 0.09$	0.94 ± 0.17	1.78 ± 0.11
14	05:38:39.0	-69:05:45.6	0.42	241.5	1.5 ± 0.2	$< 0.09 \pm 0.02$	0.76 ± 0.22	0.86 ± 0.09
15	05:38:39.1	-69:05:51.8	0.70	247.8	2.4 ± 0.3	$< 0.85 \pm 0.15$	0.81 ± 0.18	2.52 ± 0.22
16	05:38:39.2	-69:05:32.0	5.20	244.3	2.2 ± 0.2	0.42 ± 0.07	0.99 ± 0.16	21.73 ± 2.31
17	05:38:39.6	-69:05:37.2	2.05	246.3	2.5 ± 0.2	0.54 ± 0.09	1.02 ± 0.17	7.87 ± 1.00
18	05:38:40.0	-69:05:37.4	1.15	240.9	2.0 ± 0.2	0.54 ± 0.09	1.03 ± 0.17	4.75 ± 0.53
21	05:38:41.5	-69:05:25.3	0.14	254.5	1.0 ± 0.4	$< 0.85 \pm 0.34$	0.62 ± 0.40	0.12 ± 0.09
22	05:38:41.9	-69:05:42.4	2.41	237.8	2.4 ± 0.2	$< 0.72 \pm 0.10$	1.11 ± 0.14	14.52 ± 1.40
23	05:38:43.5	-69:05:57.3	2.90	236.0	2.6 ± 0.2	0.55 ± 0.08	1.05 ± 0.14	17.37 ± 1.70

Table A.1: Molecular clouds detected in the ^{13}CO(3-2) line cube. α and δ are the right ascension and declination, respectively. T_{peak} is the peak temperature detected in the ^{13}CO(3-2) line cube in K. v and Δv are the central velocity and FWHM of the clouds, respectively, in km s^{-1}. $R_{\rm dc}$ and R are the deconvolved and not deconvolved radii of the ^{13}CO(3-2) cloud, as characterized in CPROPS. For those clouds which are not resolved, we use the equations shown in Section 4.1.2 and take the deconvolved radii as an upper limit. $L_{^{13}CO(3-2)}$ is the ^{13}CO(3-2) luminosity in K km s^{-1} pc^{-2}. *Manually added detection, as CPROPS does not detect a cloud in ^{13}CO(3-2) in that location but a visual inspection reveals it.

ID	α (J2000)	δ (J2000)	T_{peak} (K)	v (km s^{-1})	Δv (km s^{-1})	$R_{\rm dc}$ (pc)	R (pc)	$L_{CS(7-6)}$ (K km s^{-1} pc^2)
2	05:38:36.5	-69:05:24.3	0.64	249.0	2.0 ± 0.2	0.17 ± 0.03	0.86 ± 0.18	2.17 ± 0.22
10	05:38:38.3	-69:05:40.2	0.14	246.5	1.3 ± 0.3	$< 0.85 \pm 0.21$	0.76 ± 0.25	0.23 ± 0.03
16	05:38:39.2	-69:05:32.5	0.45	244.0	1.8 ± 0.2	$< 0.29 \pm 0.05$	0.82 ± 0.18	1.20 ± 0.13
17	05:38:39.7	-69:05:37.8	0.20	245.4	2.7 ± 0.3	$< 0.48 \pm 0.09$	0.92 ± 0.19	0.81 ± 0.05
18	05:38:40.0	-69:05:38.6	0.09	241.1	1.4 ± 0.3	$< 0.14 \pm 0.04$	0.83 ± 0.26	0.16 ± 0.03
22	05:38:42.0	-69:05:41.5	0.10	236.8	1.4 ± 0.5	$< 0.82 \pm 0.24$	1.05 ± 0.30	0.16 ± 0.04
23	05:38:43.5	-69:05:56.3	0.28	235.8	2.7 ± 0.5	$< 0.46 \pm 0.11$	0.85 ± 0.24	0.65 ± 0.07

Table A.2: Molecular clouds detected in the CS(7-6) line cube. α and δ are the right ascension and declination, respectively. T_{peak} is the peak temperature detected in the CS(7-6) line cube in K. v and Δv are the central velocity and FWHM of the clouds, respectively, in km s^{-1}. $R_{\rm dc}$ and R are the deconvolved and not deconvolved radii of the CS(7-6) cloud, as characterized in CPROPS. For those clouds which are not resolved, we use the equations shown in Section 4.1.2 and take the deconvolved radii as an upper limit. $L_{CS(7-6)}$ is the CS(7-6) luminosity in K km s^{-1} pc^{-2}.

ID	α (J2000)	δ (J2000)	T_{peak} (K)	v (km s^{-1})	Δv (km s^{-1})	$R_{\rm dc}$ (pc)	R (pc)	$L_{HCO^+(4-3)}$ (K km s^{-1} pc^2)
2	05:38:36.3	-69:05:24.2	3.68	249.9	3.5 ± 0.3	0.44 ± 0.06	0.98 ± 0.14	25.62 ± 2.99
8	05:38:37.7	-69:05:33.5	0.13	227.2	2.5 ± 0.5	$< 0.81 \pm 0.21$	0.69 ± 0.25	0.29 ± 0.04
10	05:38:38.3	-69:05:39.6	0.41	247.0	3.1 ± 0.6	$< 0.34 \pm 0.07$	0.85 ± 0.21	1.35 ± 0.17
11	05:38:38.2	-69:05:41.6	0.09	231.3	4.1 ± 0.6	$< 0.53 \pm 0.13$	0.85 ± 0.25	0.46 ± 0.08
12	05:38:38.8	-69:05:37.3	0.15	237.1	3.5 ± 0.4	$< 0.61 \pm 0.12$	0.98 ± 0.20	0.95 ± 0.08
14	05:38:38.9	-69:05:46.1	0.12	241.4	3.1 ± 0.8	$< 0.40 \pm 0.13$	0.82 ± 0.32	0.29 ± 0.10
15	05:38:38.8	-69:05:51.1	0.53	247.4	4.5 ± 0.5	$< 0.99 \pm 0.20$	1.23 ± 0.20	3.31 ± 0.28
16	05:38:39.2	-69:05:32.3	2.83	243.9	3.0 ± 0.3	0.54 ± 0.09	0.99 ± 0.16	12.98 ± 1.91
17	05:38:39.8	-69:05:37.6	1.11	244.2	5.8 ± 0.4	0.71 ± 0.14	1.14 ± 0.20	8.12 ± 0.90
21	05:38:41.6	-69:05:25.3	0.11	254.2	2.0 ± 1.2	$< 0.81 \pm 0.30$	0.56 ± 0.37	0.11 ± 0.08
22	05:38:41.9	-69:05:42.2	0.53	237.5	2.5 ± 0.3	$< 0.82 \pm 0.14$	1.14 ± 0.17	2.86 ± 0.28
23	05:38:43.5	-69:05:57.4	0.74	235.8	2.8 ± 0.3	0.52 ± 0.09	0.99 ± 0.17	4.23 ± 0.43

Table A.3: Molecular clouds detected in the HCO$^+$(4-3) line cube. α and δ are the right ascension and declination, respectively. T_{peak} is the peak temperature detected in the HCO$^+$(4-3) line cube in K. v and Δv are the central velocity and FWHM of the clouds, respectively, in km s^{-1}. $R_{\rm dc}$ and R are the deconvolved and not deconvolved radii of the HCO$^+$(4-3) cloud, as characterized in CPROPS. For those clouds which are not resolved, we use the equations shown in Section 4.1.2 and take the deconvolved radii as an upper limit. $L_{HCO^+(4-3)}$ is the HCO$^+$ luminosity in K km s^{-1} pc^{-2}.

ID	α (J2000)	δ (J2000)	T_{peak} (K)	v (km s^{-1})	Δv (km s^{-1})	$R_{\rm dc}$ (pc)	R (pc)	$L_{HCN(4-3)}$ (K km s^{-1} pc^2)
2	05:38:36.3	-69:05:24.2	0.87	249.7	3.5 ± 0.3	$< 0.47 \pm 0.07$	0.93 ± 0.16	5.45 ± 0.58
10	05:38:38.3	-69:05:40.0	0.13	246.7	3.0 ± 0.8	$< 0.81 \pm 0.20$	0.62 ± 0.25	0.29 ± 0.04
16	05:38:39.2	-69:05:32.5	0.55	244.0	2.5 ± 0.3	$< 0.36 \pm 0.06$	0.86 ± 0.18	1.98 ± 0.28
17	05:38:39.7	-69:05:38.1	0.25	244.2	5.0 ± 0.5	$< 0.24 \pm 0.04$	0.77 ± 0.17	1.57 ± 0.14
22	05:38:42.2	-69:05:42.1	0.06	237.8	2.5 ± 1.0	$< 0.65 \pm 0.20$	0.82 ± 0.31	0.13 ± 0.05
23	05:38:43.4	-69:05:57.1	0.15	235.5	3.1 ± 0.9	$< 0.38 \pm 0.09$	0.83 ± 0.22	0.54 ± 0.07

Table A.4: Molecular clouds detected in the HCN(4-3) line cube. α and δ are the right ascension and declination, respectively. T_{peak} is the peak temperature detected in the HCN(4-3) line cube in K. v and Δv are the central velocity and FWHM of the clouds, respectively, in km s^{-1}. $R_{\rm dc}$ and R are the deconvolved and not deconvolved radii of the HCN(4-3) cloud, as characterized in CPROPS. For those clouds which are not resolved, we use the equations shown in Section 4.1.2 and take the deconvolved radii as an upper limit. $L_{HCN(4-3)}$ is the HCN(4-3) luminosity in K km s^{-1} pc^{-2}.

Appendix B

Molecular line spectra for each CO cloud

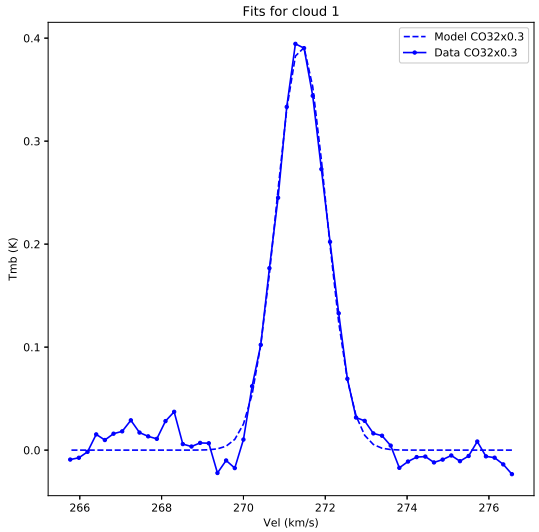

Figure B.1: Peak position spectra for cloud no. 1, with best fit Gaussian profile.

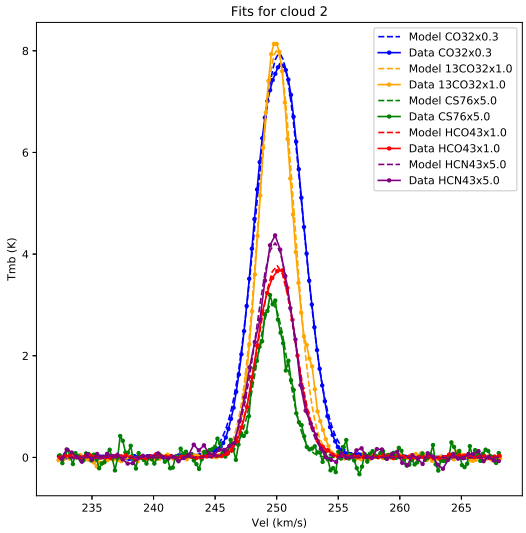

Figure B.2: Peak position spectra for cloud no. 2, with best fit Gaussian profiles.

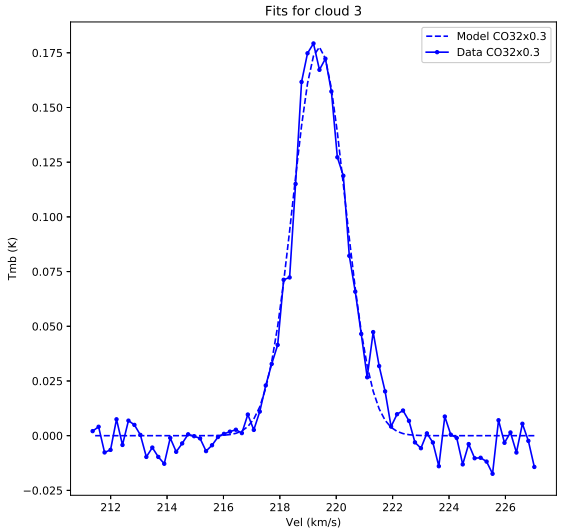

Figure B.3: Peak position spectra for cloud no. 3, with best fit Gaussian profile.

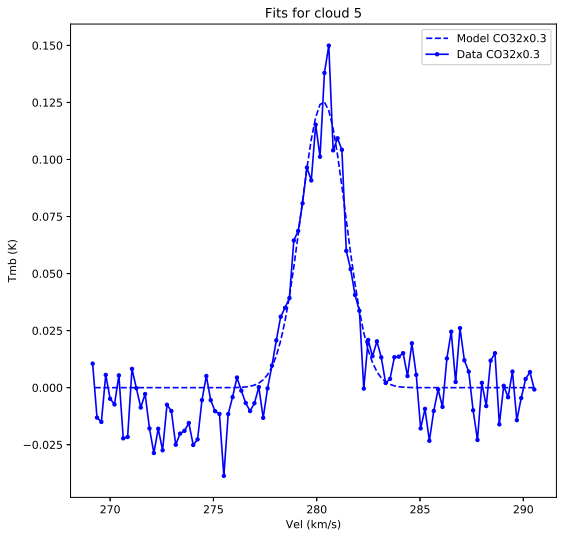

Figure B.4: Peak position spectra for cloud no. 5, with best fit Gaussian profiles.

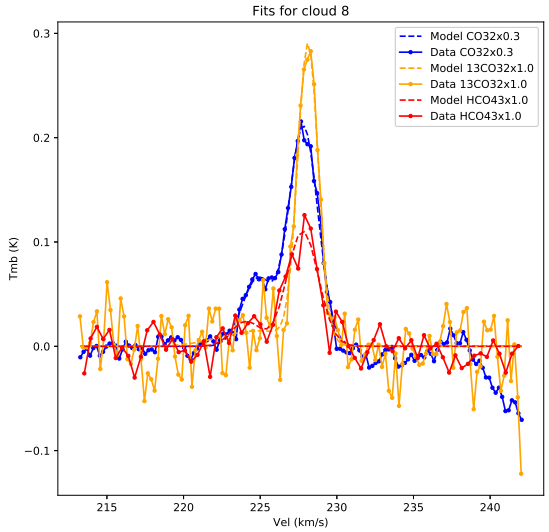

Figure B.5: Peak position spectra for cloud no. 8, with best fit Gaussian profiles.

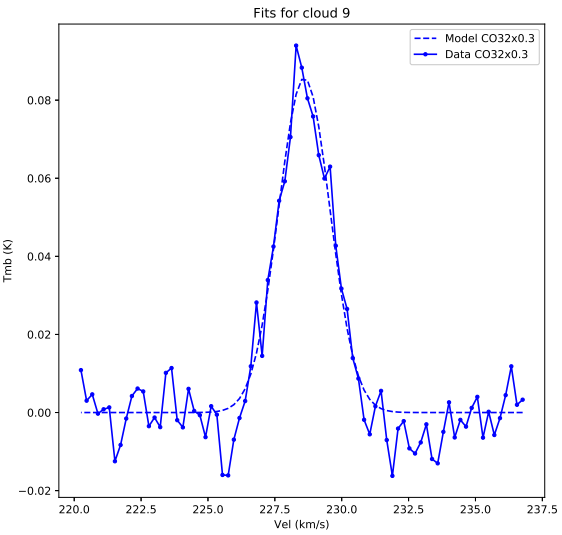

Figure B.6: Peak position spectra for cloud no. 9, with best fit Gaussian profile.

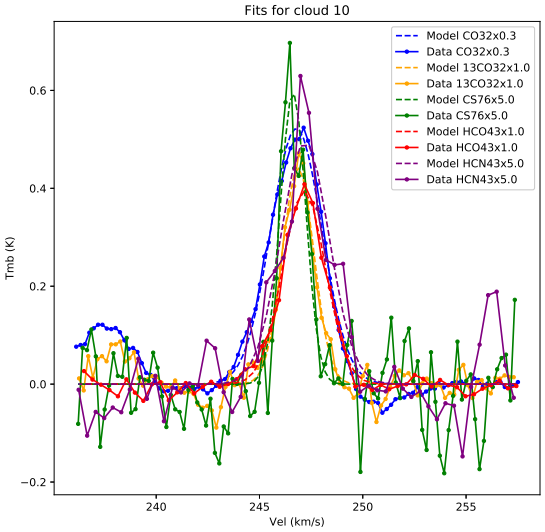

Figure B.7: Peak position spectra for cloud no. 10, with best fit Gaussian profiles. The individual spectra for each molecule is in Figure B.21.

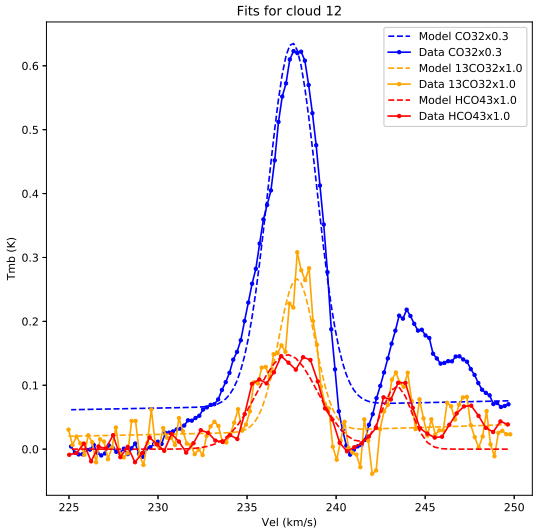

Figure B.9: Peak position spectra for cloud no. 12, with best fit Gaussian profiles.

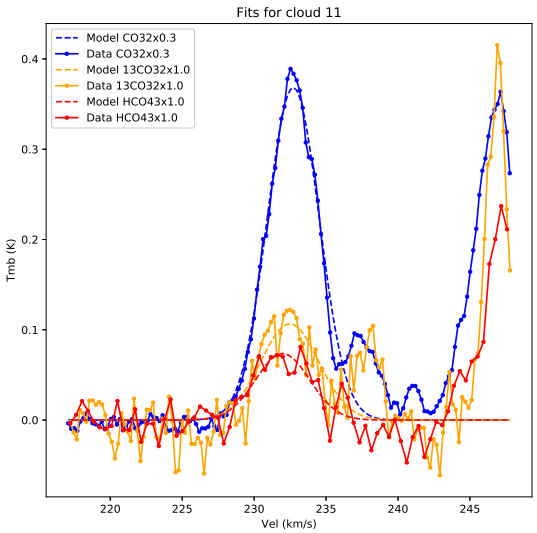

Figure B.8: Peak position spectra for cloud no. 11, with best fit Gaussian profiles. The strong emission at ~ 246 km s^{-1} corresponds to cloud no. 10.

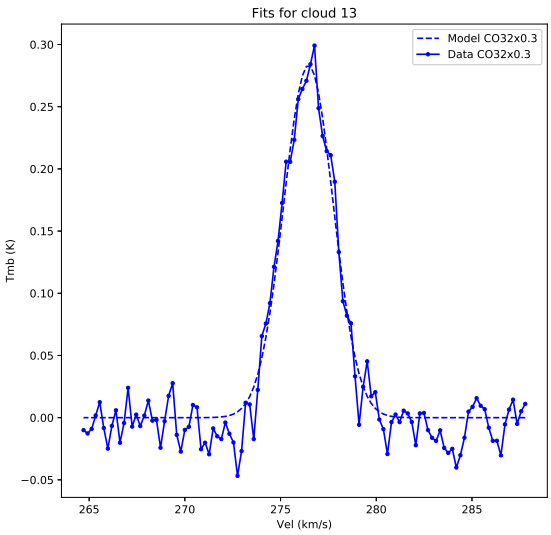

Figure B.10: Peak position spectra for cloud no. 13, with best fit Gaussian profile.

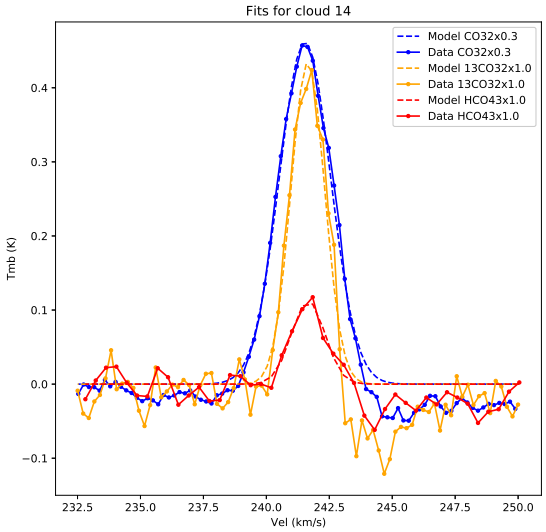

Figure B.11: Peak position spectra for cloud no. 14, with best fit Gaussian profiles.

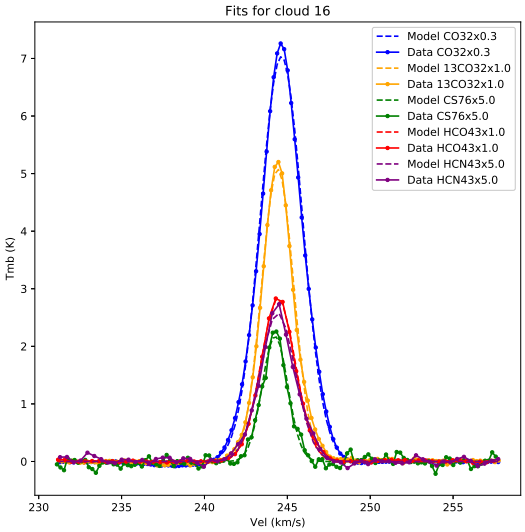

Figure B.13: Peak position spectra for cloud no. 16, with best fit Gaussian profiles.

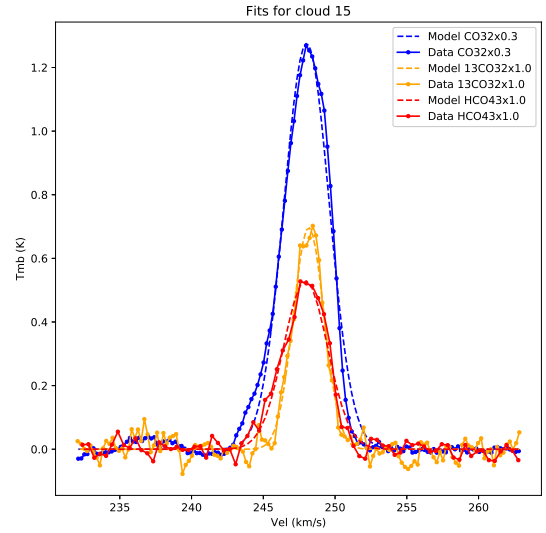

Figure B.12: Peak position spectra for cloud no. 15, with best fit Gaussian profiles.

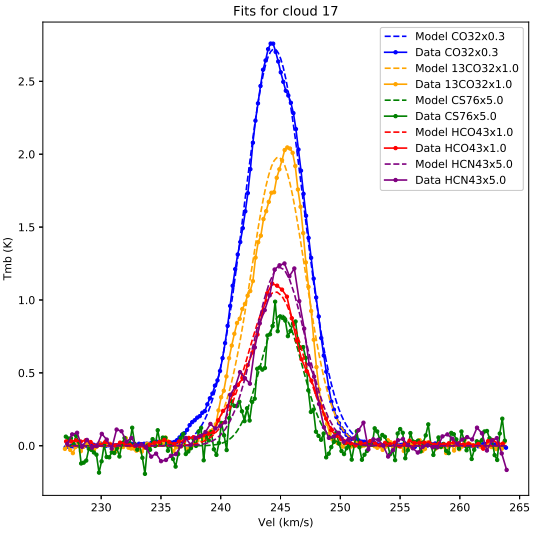

Figure B.14: Peak position spectra for cloud no. 17, with best fit Gaussian profiles.

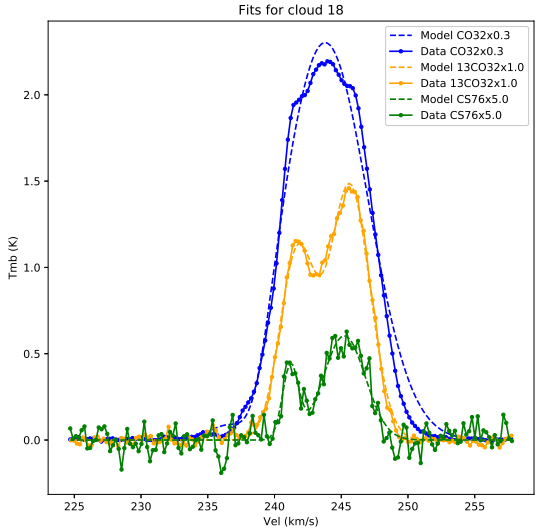

Figure B.15: Peak position spectra for cloud no. 18, with best fit Gaussian profiles. The peak at 245 km s^{-1} corresponds to cloud no. 17, whereas the peak at 241 km s^{-1} is from cloud no. 18.

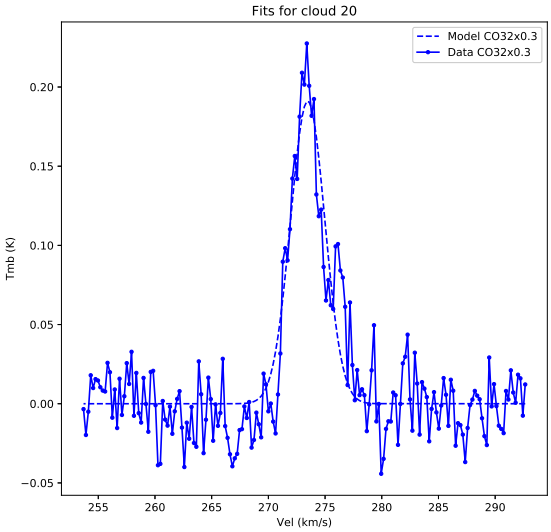

Figure B.17: Peak position spectra for cloud no. 20, with best fit Gaussian profile.

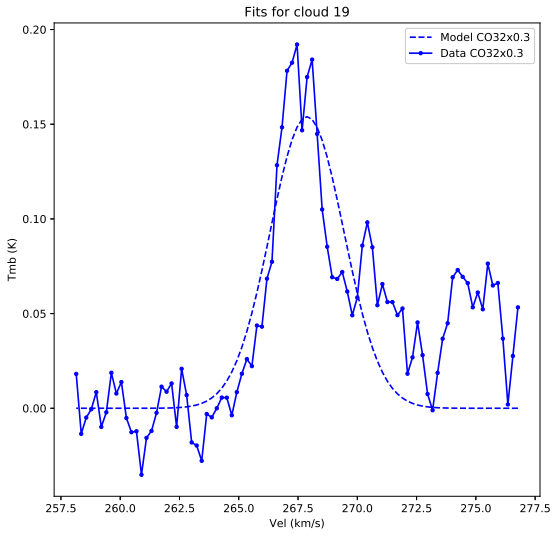

Figure B.16: Peak position spectra for cloud no. 19, with best fit Gaussian profile.

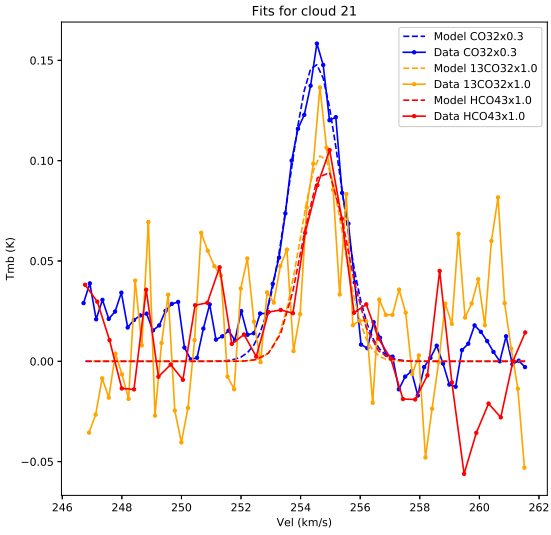

Figure B.18: Peak position spectra for cloud no. 21, with best fit Gaussian profiles.

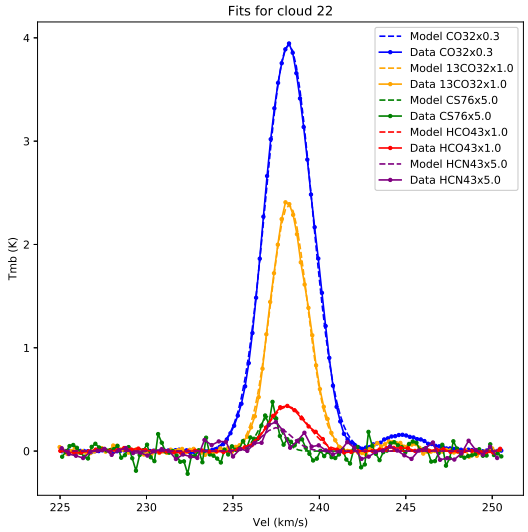

Figure B.19: Peak position spectra for cloud no. 22, with best fit Gaussian profiles.

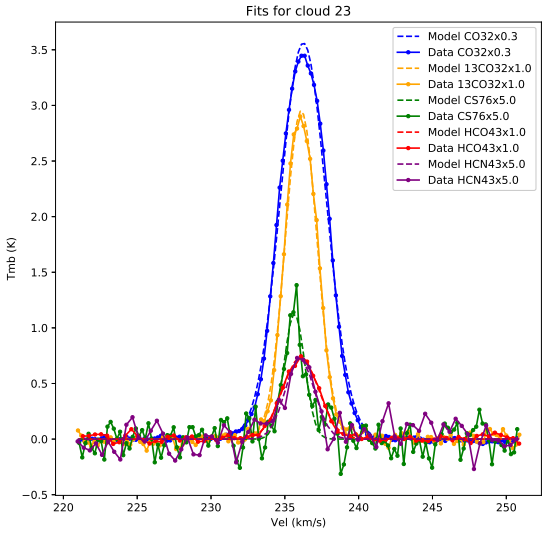

Figure B.20: Peak position spectra for cloud no. 23, with best fit Gaussian profiles.

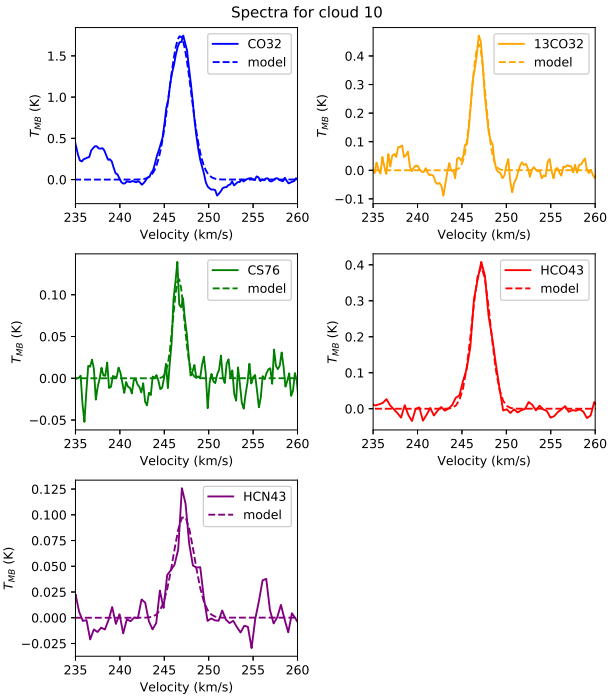

Figure B.21: Peak position spectras for cloud no. 10, separated by molecular species, with best fit Gaussian profiles.